Technische Universität München
Physik Department

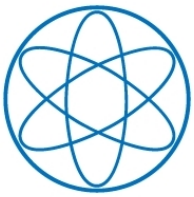

Characterisation of PNCCDs and Analysis of Pixel Defects

Dissertation
von
Gabriele Schmaler

angefertigt am Halbleiterlabor
des Max-Planck-Instituts für
extraterrestrische Physik

August 2012

TECHNISCHE UNIVERSITÄT MÜNCHEN

Max-Planck-Institut für extraterrestrische Physik

Characterisation of PNCCDs and Analysis of Pixel Defects

Gabriele Schmaler

Vollständiger Abdruck der von der Fakultät für Physik der Technischen Universität München zur Erlangung des akademischen Grades eines

Doktors der Naturwissenschaften (Dr. rer. nat.)

genehmigten Dissertation.

Vorsitzender: Univ.-Prof. Dr. Harald Friedrich

Prüfer der Dissertation:

1. Hon.-Prof. Dr. Günther Hasinger
2. Univ.-Prof. Dr. Stephan Paul

Die Dissertation wurde am 30.08.2012 bei der Technischen Universität München eingereicht und durch die Fakultät für Physik am 17.09.2012 angenommen.

Für Jens

Abstract

The next X-ray astronomy instrument performing an all-sky-survey will be eROSITA (**e**xtended **RO**entgen **S**urvey with an **I**maging **T**elescope **A**rray). It is one instrument on board the satellite **S**pectrum-**R**oentgen-**G**amma (SRG) to be launched in 2014. For X-ray detection, eROSITA uses a new version of the PNCCD, a detector concept which was already successfully employed in a satellite mission before, namely on XMM-Newton.

One aim of this thesis is to characterise the eROSITA PNCCDs as comprehensively as possible in order to select the best ones for the satellite instrument. Therefor important parameters describing the performance, e.g. the energy resolution, were measured prior to mounting and bonding the chips. Also pixel defects influencing the performance could be determined by these measurements. Based on the results, the eROSITA CCDs were evaluated in order to identify the best ones.

In addition to these measurements, this work investigates pixel defects in more detail. In particular, the observed temperature-dependent behaviour of so-called charge generating pixels is compared with model predictions. Also the influence of the back contact voltage on the charge generation centres is analysed. Finally, possible sources of non-transferring pixels are investigated by potential simulations, showing that simple model assumptions are able to reproduce the observed behaviour of those defects.

Contents

1 Introduction

1.1 X-Ray Astronomy with PNCCDs

Cosmic X-rays are not observable at the earth's surface as they are shielded by the atmosphere. Thus they can only be observed by balloon experiments or satellites. This implies that X-ray astronomy is a quite young astronomical field. The first galactic X-ray source - apart from the sun - was discovered in 1962, which marked the beginning of the rapidly evolving field of X-ray astronomy [1]. With the satellite Uhuru launched in 1970, the first all-sky survey was accomplished. Thereby over 300 sources could be identified [2]. About twenty years later in an all-sky survey performed by ROSAT, over 100,000 X-ray sources were found [3].

Observing cosmic X-rays allows you to study high energetic processes in the Universe. They are generated either thermally by extremely hot (several million degree Celsius) plasma or by fast charged particles emitting synchrotron radiation or bremsstrahlung [4]. The variety of objects emitting X-rays is huge. Their length scale ranges from small objects, e.g. the sun, to the large ones, e.g. galaxies. Also supernovae, compact objects, the interstellar medium, and galaxy clusters can be studied in the X-ray energy band, to name a few examples [5]. The intensity of the X-ray radiation and the shape of the spectrum help to investigate their origin. Furthermore studies of X-ray fluorescence lines enable one to determine the chemical composition of the source.

In order to achieve even better results than ROSAT, both the X-ray optics and the X-ray detection had to be improved in terms of spatial, time, and energy resolution. For the satellite XMM-Newton launched in 1999, an optics system with 58 nested mirror shells was designed. This setup achieved a large collecting area of about 1500 cm^2 with an angular resolution of about 6 arcsec FWHM at 1.5 keV [6]. Instead of a proportional counter as on ROSAT [7], CCDs were employed to detect the X-rays. In the semiconductor material of the CCD the energy needed to generate an electron-hole pair is about 3.6 eV. This is about a tenth of the energy necessary to ionise a gas atom in the proportional counter. Thus a photon with a certain energy generates an order of

magnitude more charge carriers in the CCD, leading to a better energy resolution. In addition to two cameras with MOS CCDs, a new CCD detector concept - the PNCCD - was used for the third camera.

The PNCCDs were specially developed for the needs of X-ray astronomy with an enhanced radiation hardness and an increased quantum efficiency for higher X-ray energies [8]. A main difference - explaining their name - is that the MOS (Metal Oxide Semiconductor) structure for the shift register is replaced by a p-n structure. More details on PNCCDs are described in chapter 2. Even today, after more than ten years in orbit, XMM-Newton is still working fine and taking data also with the PNCCD camera. The performance of the PNCCDs was so convincing that an improved version of them will be used for a upcoming next satellite mission - the eROSITA mission.

The first aim of this thesis is to characterise the PNCCDs for eROSITA without mounting and bonding the device. This allows to measure all eROSITA CCDs under the same conditions to determine their performance. Their properties can be compared directly and the best ones can be selected for the mission. In the second part, this work investigates pixel defects detected during the measurements in more detail by additional measurements and simulations.

1.2 The eROSITA Mission

eROSITA (**e**xtended **RO**entgen **S**urvey with an **I**maging **T**elescope **A**rray) is one of the two instruments currently being built for the **S**pectrum-**R**oentgen-**G**amma (SRG) satellite mission [9]. SRG is organised as a Russian-German collaboration and the current schedule foresees the launch of the satellite from Baikonur/Kazakhstan in 2014. Fig. 1.1 shows a model of the SRG satellite including eROSITA and the second instrument ART-XC (**A**stronomical **R**oentgen **T**elescope - **X**-ray **C**oncentrator).

SRG will fly in an orbit around the Lagrange point 2 (L2) of the Earth-Sun-system. During the first four years of the mission an all sky survey is planned, followed by a phase of pointed observations.

The eROSITA instrument sets the context of this thesis. It is being developed at the Max-Planck-Institute for Extraterrestrial Physics and consists of seven Wolter-Type-I telescopes with a PNCCD in each focus. It will observe the Universe in the X-ray energy range from 0.5 keV to 10 keV [9] with the main aim of studying galaxy clusters [11]. In the following sections the scientific goals and the instrumental design of the mission will be described in more detail.

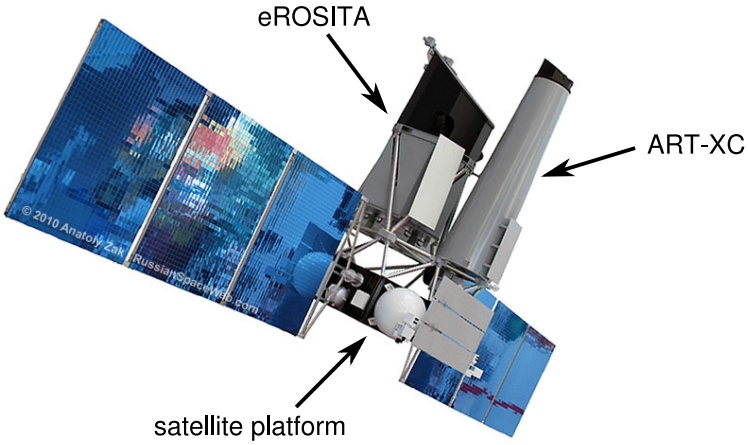

Figure 1.1: A model of the Spectrum-Roentgen-Gamma satellite with the two scientific instruments eROSITA and ART-XC. Picture adapted from [10].

1.2.1 Scientific Goals of the Mission

In 1998 the accelerated expansion of the Universe was discovered by observations of supernovae [12], [13]. The currently favoured explanation postulates an energy form called 'Dark Energy' [14]. In order to further investigate the evolution of our Universe and to constrain the parameters of the Dark Energy more measurement data is required.

As the Dark Energy acts on very large scales it will be helpful to study clusters of galaxies in this context. They can be perfectly observed in the X-ray spectral range since the intra cluster medium mainly consists of hot plasma with a temperature of about 10^8 K, thus emitting high-energy electromagnetic radiation [15]. However, to study Dark Energy a large number of clusters of galaxies has to be observed. Therefore the primary goal of the eROSITA mission is to detect at least 100,000 clusters of galaxies, a reachable aim according to simulations [16].

Studies of galaxy clusters can yield several types of information [17]. An important parameter in this context is the cluster mass function, i.e. the abundance of clusters with a certain mass. The cluster mass function depends mainly on the matter density and the primordial power spectrum which describes the amplitude of density fluctuations in the early Universe. Furthermore the evolution of the cluster mass function depends on how fast the structures are growing with time [18]. Thus constraints on Dark Matter and Dark Energy can be derived.

Another possible parameter for cosmological studies is the cluster power spectrum which describes the spatial distribution of the clusters. Information on Dark Matter and Dark Energy can be derived from the amplitude, shape, and evolution of the cluster power spectrum [17].

The detection of baryon acoustic oscillations in the cluster power spectrum is another aim which requires a large number of observed clusters [19]. In the early times of the Universe, before photons and baryons decoupled, small density fluctuations occurred and started to oscillate. These oscillations - travelling with speed of sound - were driven by the gravitation on the one hand and the radiation pressure on the other hand. When photons and baryons finally decoupled, the oscillations had a peak at a certain distance which can be seen nowadays in both, the cosmic microwave background and in the power spectrum of galaxy clusters [20]. The location of this acoustic peak in the power spectrum as a function of redshift traces the expansion history of the Universe and thus further constrains the equation of state of the Dark Energy.

Besides the studies of galaxy clusters, eROSITA also aims to detect millions of Active Galactic Nuclei (AGN), ranging from the local Universe to very large red shifts and including ones which are obscured by a dust torus [21]. It is expected that this will lead to a better understanding of this class of astrophysical objects.

1.2.2 Instrumentation

Fig. 1.2 shows a schematic drawing of the eROSITA setup which was designed to achieve the science goals described above. The mirrors and the detector modules are mounted on the telescope structure made of carbon fibre. The seven telescopes are thereby arranged in a hexagonal shape with co-aligned optical axes. Thus also pointed observations are possible. As the intensity of the observed radiation source is split between the telescopes, pile-up is reduced so that brighter sources can still be observed with a high quality. On top of the structure a sun shield is attached which protects the instrument from stray-light coming mainly from the sun [22].

Mirror Modules

Each telescope consists of a mirror module with an outer diameter of 360 mm and a length of 300 mm [21]. The focal length is 1.6 m. One such module is depicted in Fig. 1.3. It contains 54 Wolter-Type-I mirror shells with a gold coating. The Wolter-Type-I geometry is a combination of a paraboloid and a hyperboloid which focuses the X-rays onto the detector, in this case a CCD camera (see below). The resolution of the mirror module should be within 15 arcsec half energy width at 1 keV [22] on axis and 26 arcsec over the total field of view (FoV).

In front of the mirrors an X-ray baffle is mounted which prevents X-ray photons from sources outside the field of view to reach the camera by a single reflection [24].

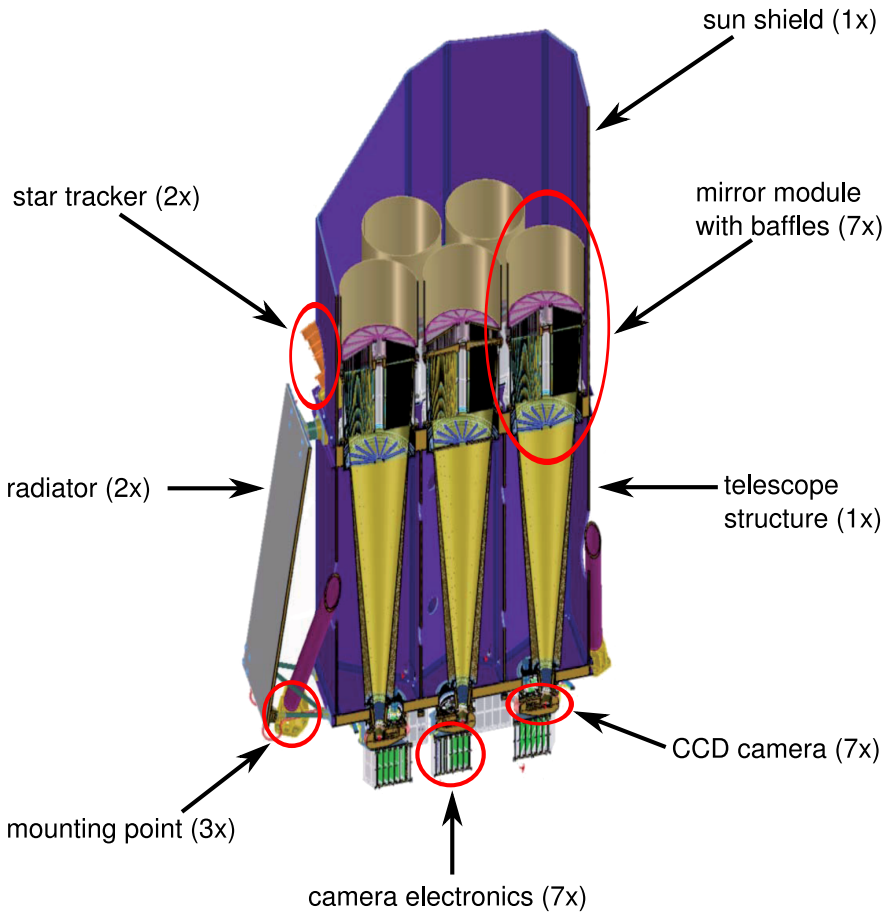

Figure 1.2: A lateral cut through the eROSITA instrument. The components are labelled in the picture and the numbers indicate how often they occur. The cover which protects the instrument from contamination during the launch is not shown in this picture. Picture adapted from [23].

This reduces the background level. In addition, a thermal baffle is mounted on top of the whole structure which reduces heat loss and helps to keep the mirrors at the desired temperature of +20 °C.

Camera

In the foci of the mirrors, the X-rays are detected by custom designed CCD cameras. The eROSITA CCDs are frame store PNCCDs which are developed and produced at the Max-Planck-Institut Halbleiterlabor (MPI-HLL). The image area is divided into 384×384 pixels, each of them with a size of $75\,\mu m \times 75\,\mu m$ [25]. In combination with the mirrors this effectively provides a field of view of about 1° in diameter.

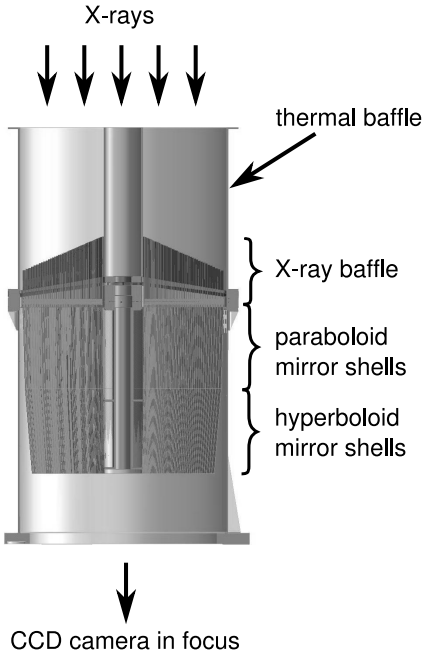

Figure 1.3: A lateral cut through a single eROSITA mirror module. The 54 nested mirror shells have a Wolter-Type-I geometry, a combination of a paraboloid and a hyperboloid structure. On top the thermal baffle can be seen which reduces heat loss in order to keep the mirrors at a temperature of +20 °C. The X-ray baffle prevents photons from outside the field of view to reach the focal plane of the telescope by a single reflection. Picture adapted from [24].

The 384 columns of a CCDs are read out in parallel with a custom designed ASIC - the so-called CAMEX (**C**MOS **A**nalog **M**ultipl**ex**er), described in more detail together with the PNCCDs in chapter 2.

Each CCD is mounted with its CAMEX chips on a common printed circuit board. To protect them from proton and fluorescence radiation the CCD-CAMEX board is embedded in a graded Z shield which consists of copper, aluminium, boron-carbide and beryllium (see Fig. 1.4). On these proton shields the corresponding readout electronic boxes are mounted. These contain among others the power converters, the sequencer providing the timing signals and the ADCs (Analog-to-Digital Converters) which digitise the analog CAMEX signals [26]. Each detector module hence is working independently.

For calibration purposes of the detector a radioactive source is integrated in the housing which can be moved into and out of the field of view. This source is composed of an ^{55}Fe source and an Al target, thus providing two spectral lines at 5.9 keV (Mn-K$_\alpha$) and 1.5 keV (Al-K$_\alpha$) [21].

Temperature Management

The eROSITA CCDs are operated at a temperature of -90 °C or lower. This way the required energy resolution can be maintained during the mission duration of seven years as leakage currents are suppressed and charge transfer losses are reduced. The

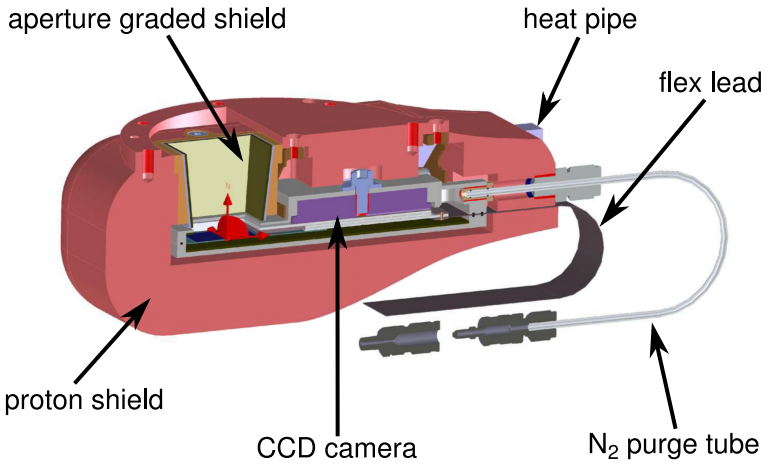

Figure 1.4: The camera module with its proton shield. The proton shield is a graded Z shield protecting the CCD and CAMEX against protons and fluorescence photons. To cool the CCD to -90 °C or lower the module is connected to a heat pipe. The whole housing can be flushed with nitrogen gas to keep the detector in a dry atmosphere. The flex lead connects the camera with the electronic box (not shown in this picture). The latter is mounted on the bottom of the proton shield. Picture adapted from [26].

CCD is cooled passively via heat pipes and radiators. Variable conductance heat pipes allow to stabilise the operating temperature with a precision of ±0.5 °C.

In contrast to the CCDs the mirror modules have to be kept at 20 °C ±2 °C in order to maintain the geometry to the required precision. Therefor heaters are attached to the mounting structure of the mirrors. The thermal baffle mentioned above helps to reduce the necessary heating power. More information on the thermal concept can be found in [27].

Grasp

An important parameter to characterise the instrument is the grasp. It is defined as the product of the 'effective area' and the 'field of view' and provides a measure for the efficiency of the instrument. The higher the grasp the shorter the time needed to measure a certain area of the sky to a given depth.

The grasp depends on the energy of the incident photon. Fig. 1.5 shows the grasp of eROSITA in comparison to that of ROSAT and XMM-Newton. Between about 0.3 keV and 2.5 keV the grasp of eROSITA is more than a factor of three higher than the grasp of XMM-Newton. eROSITA will thus be able to perform surveys in this energy range with an unprecedented sensitivity.

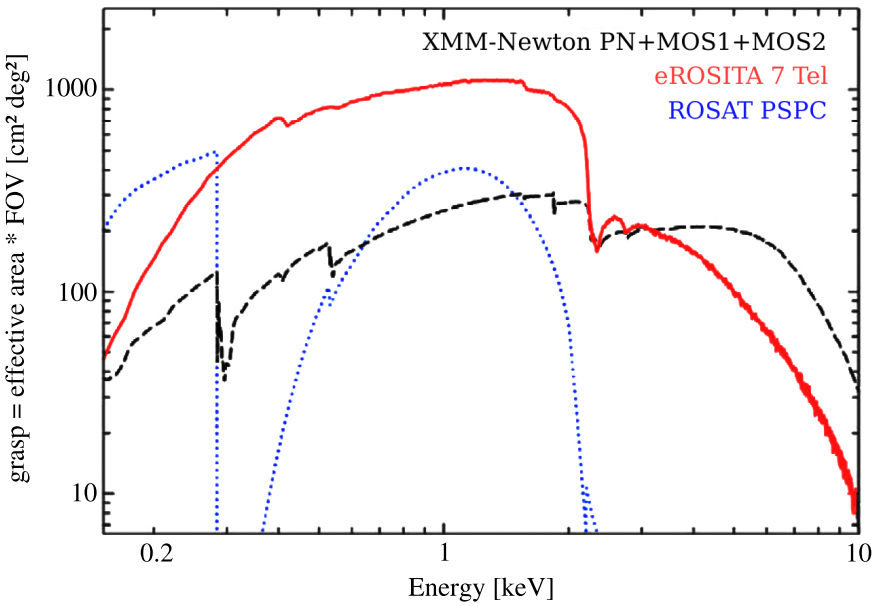

Figure 1.5: The grasp of the eROSITA instrument in comparison with the ones of XMM-Newton and ROSAT. It is a measure for the efficiency of the instrument. For energies between 0.3 keV to 2.5 keV the grasp of eROSITA is more than a factor of three higher than the one of XMM-Newton. [28]

2 Basics of PNCCDs

In 1969 W. Boyle and G.E. Smith invented the Charge-Coupled Device (CCD) [29]. For this they were rewarded with the Nobel Prize in Physics in the year 2009. Their original intention was to develop a memory device. But shortly afterwards, the imaging capability of CCDs was discovered which is used in most applications nowadays.

The basic concept of a CCD is to store charge in individual cells (pixels) which are local potential minima. These are defined by applying different voltages on metal contacts - the shift registers. By changing the voltages in a certain pattern, the charge can be moved from one pixel to the next. So the charge is moved step-by-step to a single readout node.

Based on the above concept, a novel type of CCD - the so-called PNCCD - was developed about twenty years ago [30]. The PNCCDs were specially designed for the needs of X-ray astronomy, namely for the European Photon Imaging Camera (EPIC) [31] on the satellite XMM-Newton. In the following section the PNCCD is described in more detail.

2.1 PNCCDs

The PNCCD was designed for a space instrument. An important requirement for this purpose was sufficient radiation hardness. Usually the shift registers of a CCD are made of MOS (metal-oxide-semiconductor) structures. These suffer rapidly from radiation damage as ionising radiation leads to an accumulation of positive charge in the oxide structure, changing the electric potential. As p-n structures do not suffer from this problem the MOS shift registers were replaced by p-n structures in PNCCDs. Another difference between PNCCDs and conventional MOS CCDs is the depletion depth. While in a normal MOS CCD only the first few microns beneath the surface are depleted, in a PNCCD the full detector thickness of several 100 µm is depleted which allows the detection of higher X-ray energies. The following section explains how the full depletion is reached.

2.1.1 Sideward Depletion

The penetration depth of a 10 keV photon in silicon is about 135 µm. This implies that a certain active detector volume is needed to detect X-rays with this energy efficiently. A wafer thickness of 450 µm - as used for the eROSITA CCDs considered in this work - would be sufficient for this task, if the whole volume of the detector can be made sensitive for X-ray detection. For this purpose, the volume has to be fully depleted. The full depletion of the detector volume is based on the mechanism of sidewards depletion which was discovered in 1983 by Gatti and Rehak [32]. The principle structure is depicted in Fig. 2.1(a) and works as follows:

A weakly n^- doped wafer is structured with heavily doped p^+ contacts on both sides and a n^+ contact on one side which is called front side. Thus one has a p-n-p-structure which can be regarded as two p-n junctions with a common n bulk. The n^- bulk is contacted through the additional n^+ contact. During operation, a reverse bias voltage is applied (i.e. a negative voltage on the p^+ contacts with respect to the n^- bulk). The device is therefore depleted from both sides (see Fig. 2.1(b)).

The voltage needed to achieve full depletion can be derived as follows. First consider a single p-n junction, where the dopant concentration n_p in the p^+ material is much higher than the one in the n^- material (n_n). In this case the depletion zone mainly extends into the n^- region. The voltage V required to reach the depletion width d is then given by [33]

$$V = \frac{e\, n_n}{2\, \varepsilon_0\, \varepsilon_{Si}} \cdot d^2, \tag{2.1}$$

where ε_0 is the permittivity of vacuum, ε_{Si} is the relative permittivity of silicon, and e the elementary charge. This result can be adapted to the given structure with two p^+ contacts on both sides of an n^- bulk: For full depletion, each p-n junction must only lead to a depletion width of half the bulk thickness, so that the voltage needed for full depletion is only a fourth of the one calculated above for a single p-n junction of the same thickness.

If the same voltage is applied on both p^+ contacts the potential minimum is in the middle of the wafer for a homogeneously doped bulk, as can be seen in the diagram in Fig. 2.1(c). Different voltages on both sides lead to the potential minimum being shifted away from the side with the more negative potential. In a PNCCD the voltages are chosen in such a way that the potential minimum is close to the front side. On this side the p^+ contact is not homogeneous but divided into stripes. This structure forms the shift registers which allow to store and move the charge as described in sections 2.1.2 and 2.1.3.

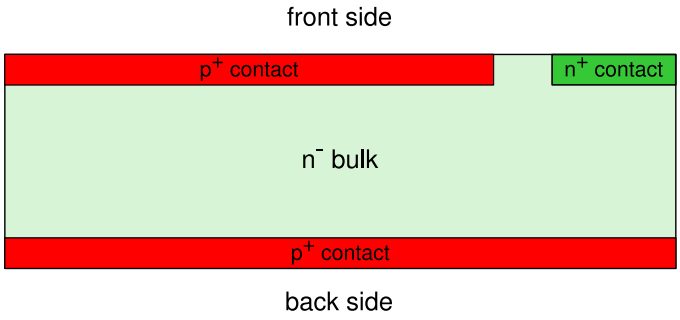

(a) Sketch of the geometry of the p-n-p structure. The side with the n^+ contact is called front side and the opposite side is called back side.

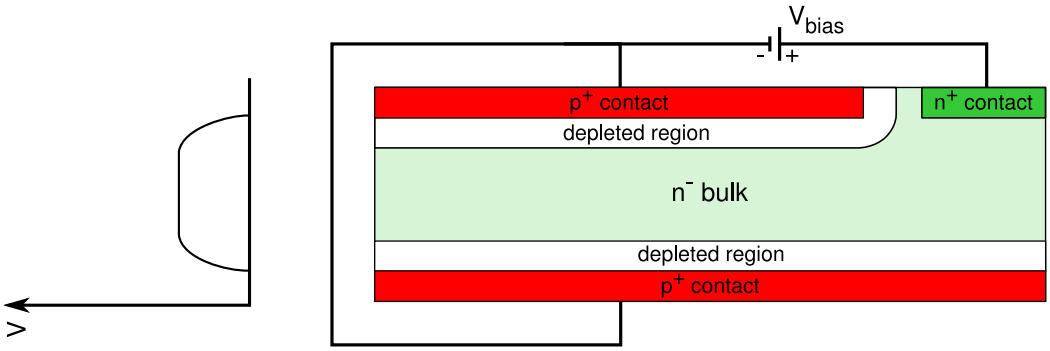

(b) If a small negative voltage is applied to the p^+ contacts, the structure is partly depleted. On the left a sketch of the electric potential in the structure is shown.

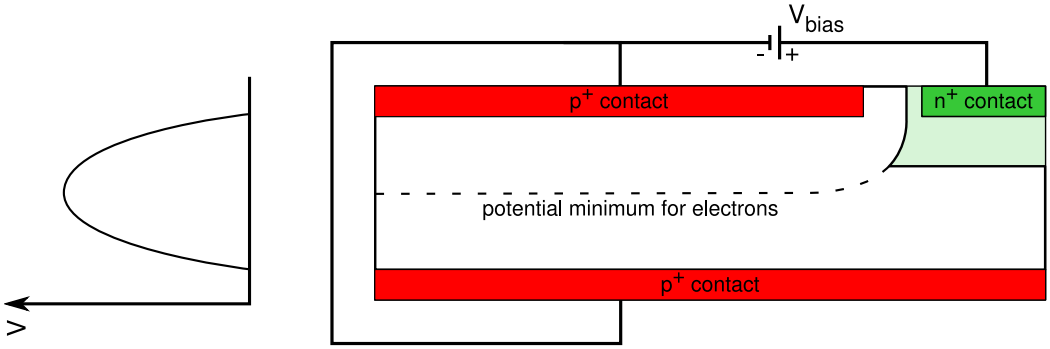

(c) With a more negative voltage the structure can be fully depleted. In this picture the p-n-p structure is nearly fully depleted. The potential minimum lies in the middle as both p^+ contacts are on the same potential.

Figure 2.1: Illustration of the concept of sidewards depletion.

The high quantum efficiency at higher X-ray energies is only one advantage of a fully depleted detector. Furthermore, the detector can be illuminated from the back side - the side opposite of the shift register structure - allowing for a homogeneous entrance window. In a front side illuminated CCD the photons instead have to pass the shift register structure where part of them is absorbed (especially low X-ray energies with short absorption lengths).

Another advantage of the back side illumination is that the entrance window can be optimised for different applications, e.g. with an anti-reflective coating for optical applications or with an aluminium layer to suppress optical photons in X-ray applications.

2.1.2 Charge Generation and Collection

Charge Generation

Before the PNCCD is described in more detail, the generation of electron-hole pairs by incident X-ray photons shall be explained. In the eROSITA energy range the photoelectric effect is the dominant interaction mechanism of X-rays with silicon. The incident X-ray photon with an energy E_{photon} is absorbed by an electron from the inner shells (K or L) of a silicon atom, leaving the silicon atom in a singly ionised excited state. The emitted photoelectron has a kinetic energy of $E_{kin} = E_{photon} - E_B$, where E_B is the binding energy of the electron. The excited silicon atom emits an Auger-electron or a fluorescence photon during the relaxation process. Usually the fluorescence photon is reabsorbed, causing a second photoelectron.

The photoelectrons and Auger-electrons lose their kinetic energy through coulomb collisions during their movement in the silicon bulk. In each coulomb collision part of the kinetic energy is used to create an electron-hole pair and another part is transferred to a phonon. Ultimately, the whole energy of the absorbed X-ray photon is thus used to create electron-hole pairs and phonons. In silicon, the effective mean energy needed to create one electron-hole pair is thereby $\varepsilon = 3.65\,\mathrm{eV}$ at a temperature of 300 K [34] which is significantly higher than the band gap of 1.12 eV [33]. The difference is due to the creation of phonons. As an example, for a Mn-K_α photon with an energy of 5.9 keV about 1600 electron-hole pairs are created.

Since the energy conversion into electron-hole pairs is a statistical process the number n of created electron-hole pairs is not exactly $n = \frac{E_{photon}}{\varepsilon}$, but distributed around this

mean value. The Fano theory gives the variance for this distribution as follows:

$$\langle \Delta n^2 \rangle = F \cdot \frac{E_{photon}}{\varepsilon} \tag{2.2}$$

where F is the Fano factor. For example, in silicon the Fano factor for X-ray energies above 1.5 keV is 0.12 [35]. Thus the standard deviation of the number of generated electron-hole pairs for 5.9 keV Mn-K$_\alpha$ photons is $\Delta n = 14$. This sets a lower limit to the energy resolution - i.e. the full width at half maximum (FWHM) of the Mn-K$_\alpha$ peak - of about 120 eV.

Charge Collection

It was explained in section 2.1.1 that in a PNCCD the bulk is fully depleted. To achieve this depletion, a negative voltage is applied at the p^+ implants on both sides with respect to the n^- doped bulk. The latter is contacted through an n^+ side contact. The voltages applied at the p^+ implants are chosen in such a way that the potential minimum of the electric field is located close to the front side. The electric field separates the cloud of electron-hole pairs before the electrons and holes can recombine. The holes drift to the back contact whereas the electrons drift to the potential minimum near the front side. This potential minimum is divided into a two-dimensional array of local potential minima - the pixels. The directions of the pixel array are called channels and rows (the collected charge will later on be transferred along a channel, whereas the rows are perpendicular to the transfer direction). The potential minima are created differently for channels and rows as described in the following.

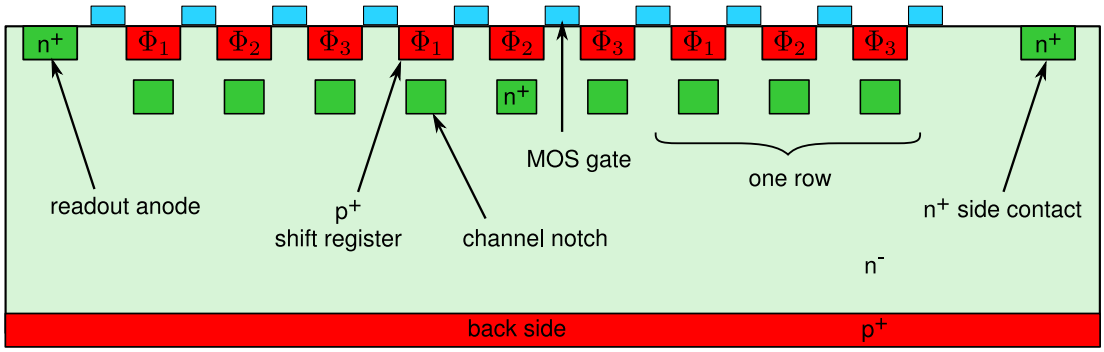

Figure 2.2: In this cut along a PNCCD channel the shift registers on the front side can be seen which are separated by MOS gates. Three shift registers define one row.

The separation of rows is illustrated in Fig. 2.2 showing a cut through the CCD along a channel. The p^+ implants on the front side are the shift registers. By applying

different voltages to the shift registers a structure of potential minima and maxima is created which defines the rows. For one row three shift registers are needed. If the voltages are now changed in a certain sequence, the charge can be transferred to the readout anode step-by-step. This process is described in more detail in section 2.1.3. The shift registers are separated by MOS contacts improving the isolation between them. Furthermore the MOS contacts attract electrons generated by surface defects. These electrons are thus prevented from drifting into the bulk where they would mix with the signal electrons.

The channels are separated from each other by a p^+ implant in a depth of about 1 µm from the front side, called channel stop (see Fig. 2.3). Between the channel stops, there is an n doped region - the channel guide - which has a higher dopant concentration in the middle - the channel notch. No voltage has to be applied to the channel stop, channel guide and notch as the potential structure is built by the space charge of the implantations. The potential minimum of a channel - where the charge is stored - is located in the channel notch due to the higher dopant concentration.

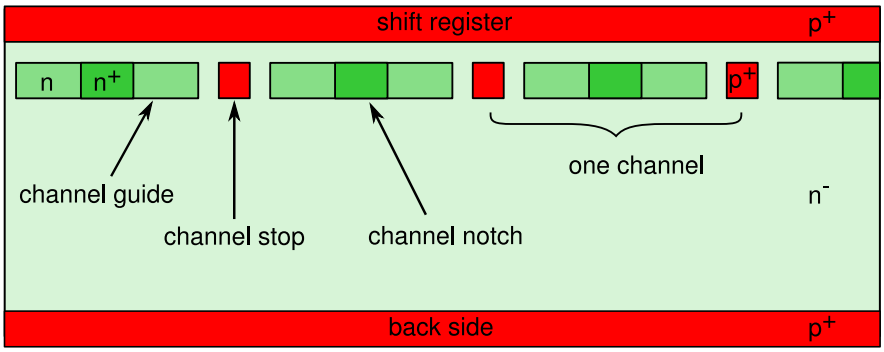

Figure 2.3: A cut along a PNCCD row. The p^+ and n implantation of the channel stop and guide, respectively, form the potential structure of the channels. The charge is collected in the potential minimum which is in the middle of the channel due to the higher dopant concentration of the channel notch.

Split Pattern

After the charge cloud is generated in the bulk it drifts to the potential minimum on the front side. Along the way it expands due to diffusion and electrostatic repulsion. When the charge cloud finally reaches the potential minimum at the front side, the radial symmetric charge distribution has a Gaussian shape with a sigma radius of roughly 10 µm at an energy of 5.9 keV [36]. Hence, with a pixel size of 75 µm × 75 µm, the charge can spread over four neighbouring pixel at most (in an area of 2x2 pixels).

Consequently, with the applied event threshold (see section 3.4), only four different types of valid split patterns can occur for a single interaction. They are depicted in Fig. 2.4.

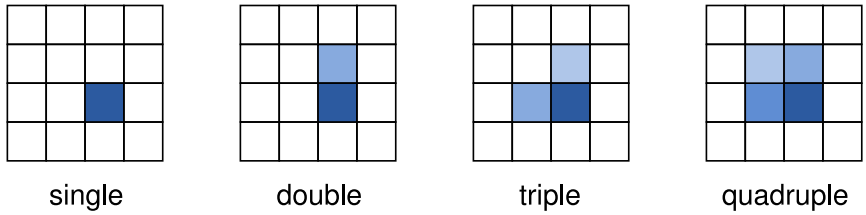

Figure 2.4: Valid split patterns. Also rotations of these patterns are valid.

First of all, the charge can be collected in a single pixel, a so-called single event. If the charge is generated near a pixel border, it distributes over two neighbouring pixels. This is named a double event. Two types of double events can be distinguished as the charge can spread either in a row or in a channel: If the charge is distributed over two pixels in the same row, it is called a left/right double (l/r double). In contrast, a double event in the same channel is a forward/backward double (f/b double). Due to the radially symmetric shape of the charge cloud it cannot split on two pixel along a diagonal. Such a pattern is called invalid.

Another possibility for a valid pattern is a triple or quadruple split event. These are generated by an X-ray photon which is absorbed near the pixel corner and thus splits over three respectively four close-by pixels. For a valid triple event, one requires the maximum charge to be in the corner. A quadruple event is only accepted as valid if the highest and the lowest signal are on the diagonal as otherwise at least two photons must have hit the detector. Some examples for invalid patterns are given in Fig. 2.5.

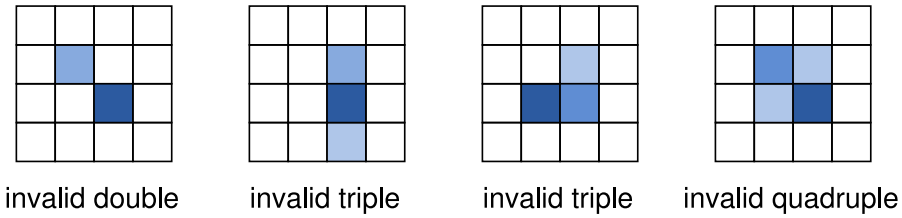

Figure 2.5: Some examples for invalid split patterns.

For a spectral analysis one has to know the total amount of charge generated by an incident X-ray photon. Thus the charge of the split patterns has to be recombined. However, only valid split patterns contain the energy information of a single photon.

On the other hand, invalid patterns can be caused either by pile-up events - i.e. two or more photons have hit the detector close by - or by the noise being above the event threshold. In these cases, the recombined charge would be the sum of two or more photons or the sum of at least one photon and the noise. Anyway, the recombined charge is not a valid measure of the energy of a single detected X-ray photon and the pattern must be discarded.

2.1.3 Charge Transfer

The shift registers on the front side of the CCD provide the potential structure of the rows for the charge collection and transfer. Each row is defined by three shift registers which are called Φ_1,Φ_2 and Φ_3. If voltage pulses with different phases are applied to these shift registers, the charge can be transferred from one row to the next. As described before, the channels are separated through the channel stops, so the charge is transferred solely within the channel from one pixel to the next.

In Fig. 2.6 the timing pattern of the voltage pulses in the shift registers is illustrated. During the integration time (i.e. before the first transfer step) both shift registers Φ_1 and Φ_2 have a more positive potential than Φ_3. Thus the charge is collected below Φ_1 and Φ_2. The storage usually happens below two shift registers, but also a storage below one register is possible.

In the first step of the charge transfer the potential of Φ_2 is changed to the more negative one. Thus the charge moves to the potential minimum below Φ_1. Then the potential of Φ_3 is changed to the more positive one which extends the potential minimum for the electrons, now being located below Φ_3 and Φ_1. By repeating these two steps with alternating shift registers as shown in Fig. 2.6 the charge moves on, and thus after six steps finally reaches the pixel of the next row.

When the first row - i.e. the row closest to the anode - is reached, the charge is shifted to the anode itself, which is an individual n^+ contact for each channel. The anodes are read out in parallel as described in section 2.2.

Charge Transfer Efficiency

During the transfer from one pixel to the next, charge might be lost, either by being trapped by a defect in the silicon crystal grid or due to imperfections of the potential structure. The mean value of the relative amount of charge shifted from one pixel to the next is called charge transfer efficiency (CTE). Instead of the CTE, it is often

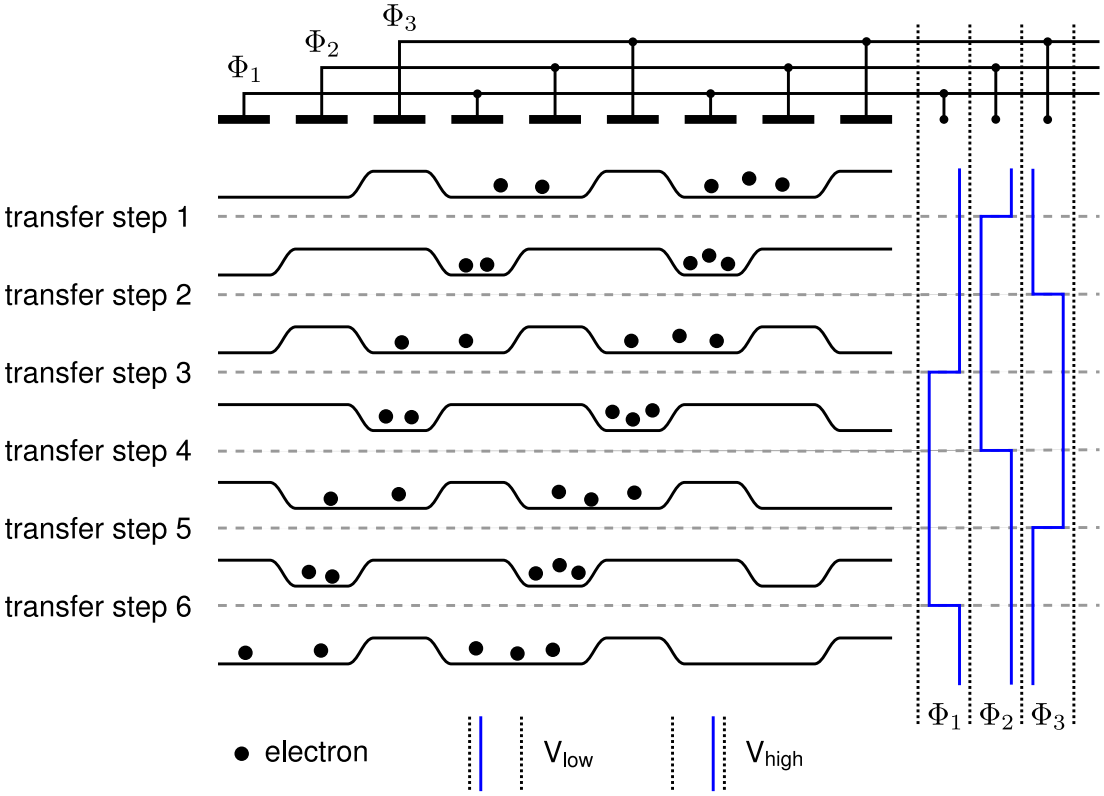

Figure 2.6: Six steps are needed to transfer the charge from one pixel to the next. The charge is transferred by changing the voltages on the shift registers between the voltage V_{high} and the more negative one V_{low}. The voltage pulses applied to the shift registers in each step are shown on the right. The transfer direction is from the right to the left. Picture adapted from [36].

more convenient to use the complementary value, the charge transfer inefficiency (CTI) CTI $= 1 -$ CTE, which describes the relative amount of charge lost by one transfer.

2.1.4 Frame Store CCD

As mentioned in the section 1.2.2 the PNCCDs for eROSITA are frame store CCDs. This means that the pixel array is divided into two parts - the image (IM) and the frame store (FS) area. The image area is illuminated with X-rays whereas the frame store area serves as storage and is shielded against X-ray radiation. After a certain integration time the charge accumulated in the image area is shifted quickly to the frame store area. Then the signal from the frame store area is transferred at a slower pace to the anode where it is read out, while the next image already accumulates in the image area. This operation mode is called frame store mode (FS mode) and is usually used to operate the eROSITA CCDs.

Alternatively, there is also the possibility to read out the whole CCD at a steady pace and get one large image from both parts. This mode - called full frame mode (FF mode) - is important for a full characterisation of the CCD, particularly for pixel defects.

As the charge has to be moved independently in both parts of the CCD, each part has its own three shift registers, i.e. there are six shift registers in total. The shift registers in the image area are named Φ_1, Φ_2 and Φ_3 while those in the frame store area are called Φ_4, Φ_5 and Φ_6.

The advantage of operating the CCD in FS mode is the reduction of out of time events as described in the following section.

Out of Time Events

Unlike in a normal photocamera there is no shutter which covers the CCD while the image is transferred to the anode and read out. Thus X-ray photons can hit the CCD during this time, i.e. out of the regular integration time. Such events are named out of time events (OOT).

An example is shown in Fig. 2.7. A source irradiates a spot around row 220. After a certain integration time frame 1 is read out. During the transfer two photons hit the CCD. These are, however, effectively detected not in row 220 (the nominal position of the source) but in row 350 of this frame and row 100 of the next frame, respectively. It is not possible to distinguish these events from 'normal' ones and thus the image is distorted.

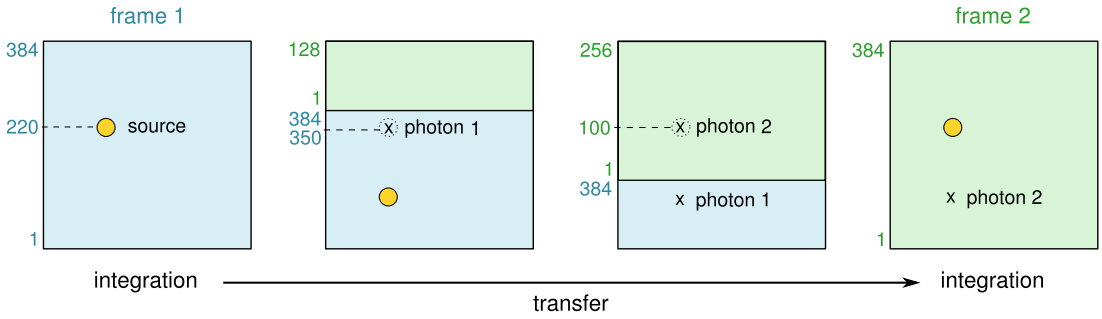

Figure 2.7: On the left picture the CCD is shown during the integration of the first frame. The numbers on the left side are the row numbers of this frame. The next two pictures illustrate the readout of the first frame, while the picture on the right shows the next frame during integration. The source irradiates a spot around row 220. If a photon hits the CCD during the transfer of the image, it is detected in a wrong row. These events are called out of time events.

OOT events have not only a wrong position information, but due to the CTI correction (see 3.4) also a wrong energy information which worsens the measured energy resolution [37]. Another consequence of the OOT events is an error in the CTI calculation. For example, the signal of photon 1 (in Fig. 2.7) which is detected in row 350 has lost less charge than a normal event, as it was only transferred over about 220 rows to the readout anode. Thus, for this event the CTE seems to be better than it really is.

As the time needed to transfer the image from the IM area to the FS area is much shorter than the time needed for the signal read out of the whole image, the number of OOT events is significantly smaller when the CCD is operated in FS mode. The number of OOT events n_{OOT} is proportional to the ratio of the transfer time of the image t_t to the integration time t_i: $n_{OOT} \propto \frac{t_t}{t_i}$. The transfer time including the read out takes about 9 ms for the image area, whereas the time needed for just shifting the image from the IM area to the FS area is only 115 µs. The number of OOT events is thus 80 times smaller when the CCD is operated in FS mode.

2.1.5 PNCCDs for eROSITA

After explaining the basics of a PNCCD, the properties of an eROSITA PNCCD in particular are described in this section. The image area of an eROSITA chip has a size of 28.8 mm × 28.8 mm (see Fig. 2.8). For handling and mounting of the chip it has an insensitive fringe of about 4 mm leading to a total size of 37 mm × 56 mm.

The eROSITA CCD is a frame store PNCCD with 384 × 384 pixel in both the image and frame store area. The pixels in the image area are square with an edge length of 75 µm. In the frame store area the pixel size is shortened to 75 µm × 51 µm in order to reduce the chip size and thereby the detector housing. The thickness of the detector is 450 µm.

The back side of the FS area is covered with a 1 µm thick aluminium layer. For the entrance window - i.e. the back side of the IM area - there are two options implemented. Either it is covered with 200 nm of aluminium or with no aluminium at all. In the first case the CCD can be used without an external filter as the optical light is sufficiently suppressed by the entrance window. In this case the quantum efficiency is more than 90 % in the energy range of 3 keV to 10 keV [39]. In the second case (without aluminium) such a high quantum efficiency can reached for a larger energy range from 0.3 keV to 10 keV [40], if the PNCCD is used without an external filter. However, for the suppression of optical light an external filter has to be used in this case which has to be included in the final quantum efficiency.

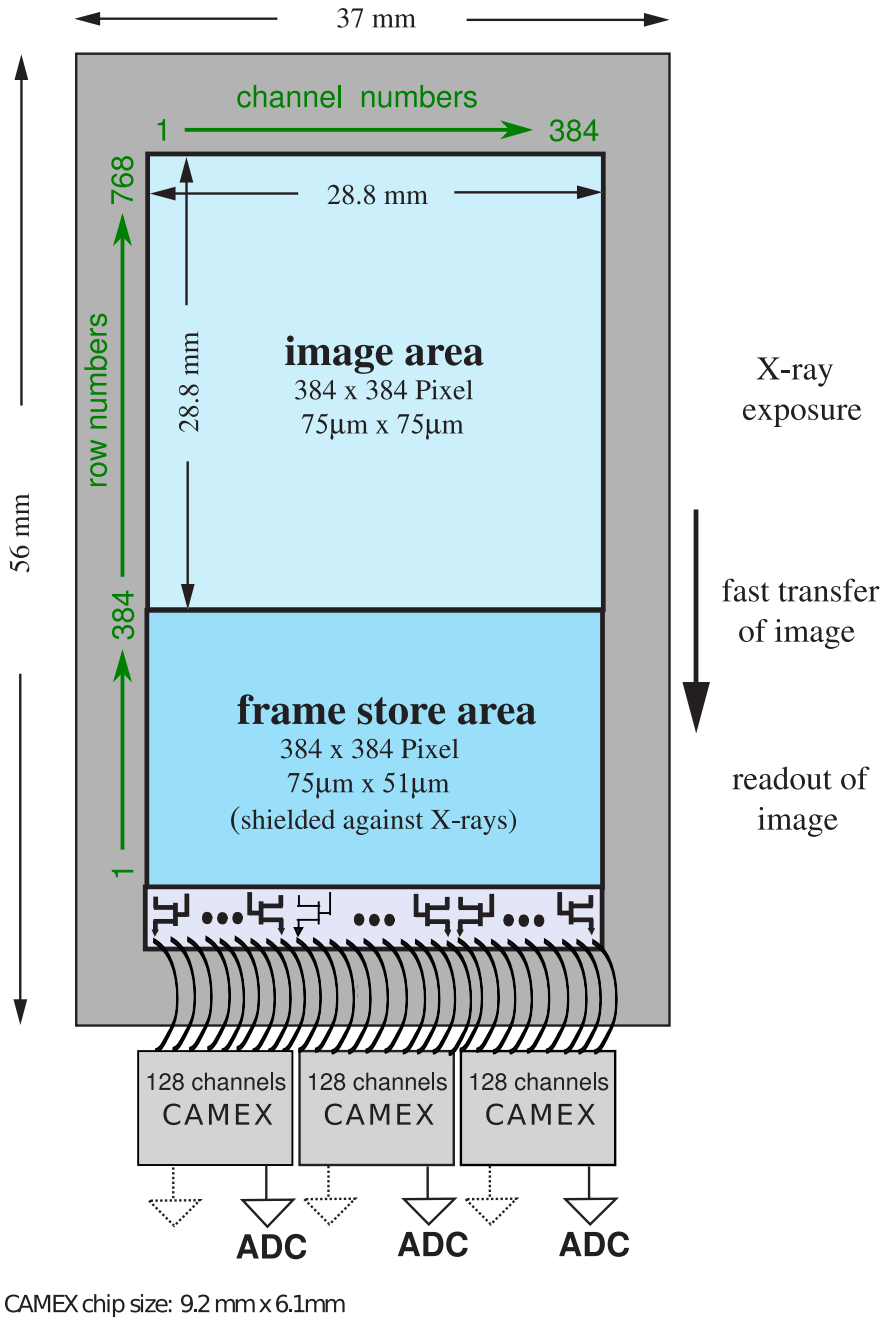

Figure 2.8: A sketch of an eROSITA chip showing the image and the frame store area with their different pixel sizes. Furthermore the transfer direction and the numbering of the rows and channels is presented. Picture adapted from [38].

An energy resolution of about 134 eV at 5.9 keV can be reached with an eROSITA PNCCD [40]. The fraction of OOT events is only 0.23 % for the planned operation in FS mode with a cycle time of 50 ms. In principle a shorter cycle time (down to 9 ms) is possible. This is not used for eROSITA for thermal reasons. With the long cycle time of 50 ms the CAMEX can be switched to standby between the readout cycles. Thus the heat dissipation by the CAMEX is reduced which allows for the operating temperature of -90 °C or lower on the satellite [40].

2.2 Signal Amplification and Readout

2.2.1 On-Chip Electronics

The first amplification step is directly integrated on the chip to reduce the noise or strictly speaking to improve the signal-to-noise ratio. As no wires are needed to connect the anode to the first amplifier the input capacitance is smaller and thus the voltage change induced by a certain amount of charge is higher.

All channels of a PNCCD are read out in parallel, because each anode is connected to the gate of its own 'First-FET'. This First-FET is an n-channel JFET operated in source-follower mode, thus changing the high input impedance due to the small detector capacitance to match the lower one of the following electronics [41]. The current sources - needed for the source-follower mode operation - are integrated on a special readout ASIC designed for the CCDs, the CAMEX (**C**MOS **A**nalog **M**ultipl**ex**er) (see section 2.2.2).

In order to remove the charge collected on the anode, the anode is connected to the source of a Reset-FET (see Fig. 2.9). The drain (RSTA) contact of this Reset-FET is supplied with a static voltage. For the gate (RGAT) contact there are two possibilities for the voltage supply. The first one is a pulsed voltage which either blocks or enables the reset current. Thus the charge on the anode can be removed quite fast at some point of the readout (e.g. after one row or one frame - as needed). The second possibility is to apply a static voltage at the RGAT contact. Depending on the applied voltage a small current through the Reset-FET can clear the anode continuously or block the reset. Independent of the charge reset by the Reset-FET, the charge is removed continuously from the anode at a slow rate by a gate-to-drain current in the integrated First-FET (for more details on this meachanism see [42]).

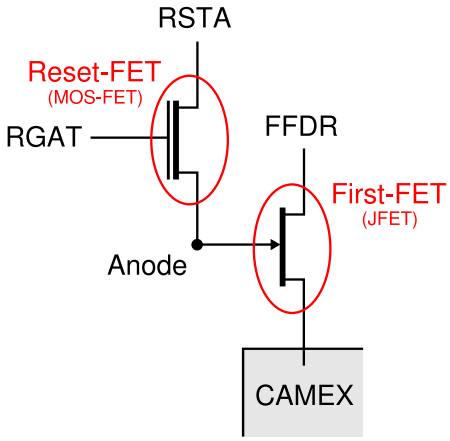

Figure 2.9: Schematic of the on-chip electronics integrated individually for each channel, consisting of the First-FET and the Reset-FET.

2.2.2 CAMEX

Simultaneously with the PNCCD a special ASIC - the CAMEX - was developed for the CCD readout at the MPI-HLL. The CAMEX chips are designed for a channel parallel amplification and shaping of the PNCCD signals [43]. Each CAMEX has 128 input channels, so three chips are needed for the readout of one eROSITA PNCCD. In Fig. 2.10 a block diagram of one CAMEX channel is shown. The first part is the current source for biasing the First-FET on the CCD. Then a JFET preamplifier follows where different values for input and feedback capacitance and thus different amplification factors can be chosen by statically programmable switches. The next step is a passive low pass filter which limits the bandwidth and thus reduces the noise but limits the readout speed. Again different values can be selected ranging from 150 kHz to 1750 kHz.

The low pass filter is followed by the signal sampling stage. For the signal sampling an 8-fold correlated double sampling filter is implemented which is described in detail in [44]. Basically it works as follows (see Fig. 2.11): At first the baseline is sampled eight times, then the CCD signal is shifted to the anode and again eight samples (of the baseline plus the signal) are taken. The difference between both sampling blocks is proportional to the charge shifted to the anode. By averaging over eight samples the signal to noise ratio is increased as the white noise contribution is reduced. In this correlated double sampling stage another amplifier is embedded where also different values for the amplification can be chosen.

In the Sample & Hold stage the signal is stored until it is multiplexed to the output node of the CAMEX. The signal sampling stage and the Sample & Hold stage can be separated by opening the switch between them. Thus it is possible to amplify and

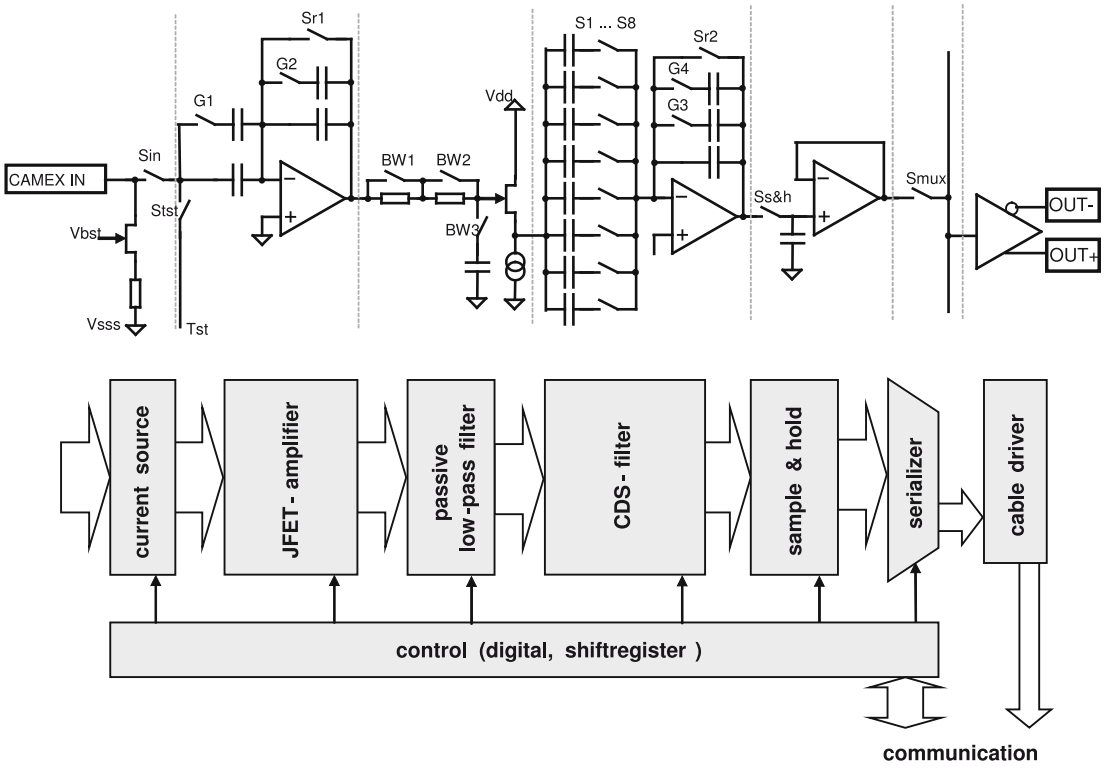

Figure 2.10: A block diagram of one CAMEX channel illustrating all steps of signal processing. Each CCD channel has its own CAMEX channel, so that their signals can be read out and amplified in parallel before they are serialised to the cable driver. Picture adapted from [43].

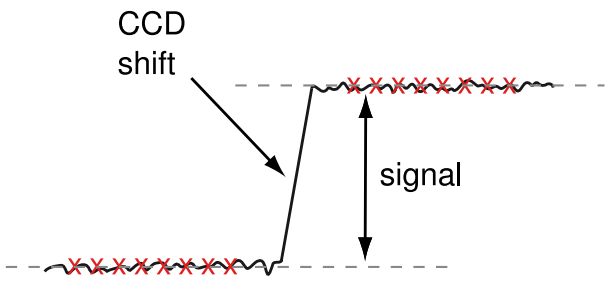

Figure 2.11: The 8-fold correlated double sampling, as described in the text. Both the baseline and the signal after shifting the charge to the anode are measured eight times. The signal level is averaged over the eight samples and thus the noise is reduced. The difference between both sample blocks is proportional to the signal charge on the anode. Picture adapted from [45].

sample the next line while the previous one is multiplexed to the output buffer. As the signal is transmitted differentially from the output buffer, it is amplified by an additional factor of two, leading to an overall gain in the range of 1 to 240.

Several switches on the chip need a timing signal which is provided by an internal shift register sequencer. Before a measurement, both the shift register and static switches are programmed by an external sequencer which also synchronises the timing signal of CAMEX and CCD.

3 Measurements for Defect Analysis and Characterisation of PNCCDs

For satellite instruments like EPIC on XMM-Newton or eROSITA on SRG, high quality standards are required for the integration of the CCDs on the detector module. This process is hence quite time-consuming. Furthermore, the flight qualified electronic components are expensive. Thus integrating a chip which is not working perfectly is a waste of resources. To prevent this, the only possibility is to test and qualify the CCDs as extensively as possible before the integration.

For this purpose, about fifteen years ago a special measurement setup was designed in order to test the PNCCDs developed for the XMM-Newton project in full operation beforehand, but without mounting and bonding the chip. Instead, the CCDs were contacted with needles. This setup - called Cold Chuck Probe Station (CCPS) - was modified to test the PNCCDs for eROSITA, allowing to characterise the CCDs and study existing defects. In the following the setup and the measurements are described in detail.

3.1 Experimental Setup - The Cold Chuck Probe Station

In Fig. 3.1 a picture of the Cold Chuck Probe Station can be seen. The setup is housed in a dark box. To fully operate the CCD, 400 needles are needed, one for each of the 384 CCD channels and 16 needles to supply all necessary operating voltages. All needles except one are mounted on a printed circuit board (PCB) called probe card. Fig. 3.2 shows the part of the probe card where the needles are mounted. They contact the PNCCDs via the bond pads on the front side of the chip. The remaining needle touches the chip on the back side on the thicker Al layer in the frame store area. This back contact needle is mounted on the chuck as shown in Fig. 3.3.

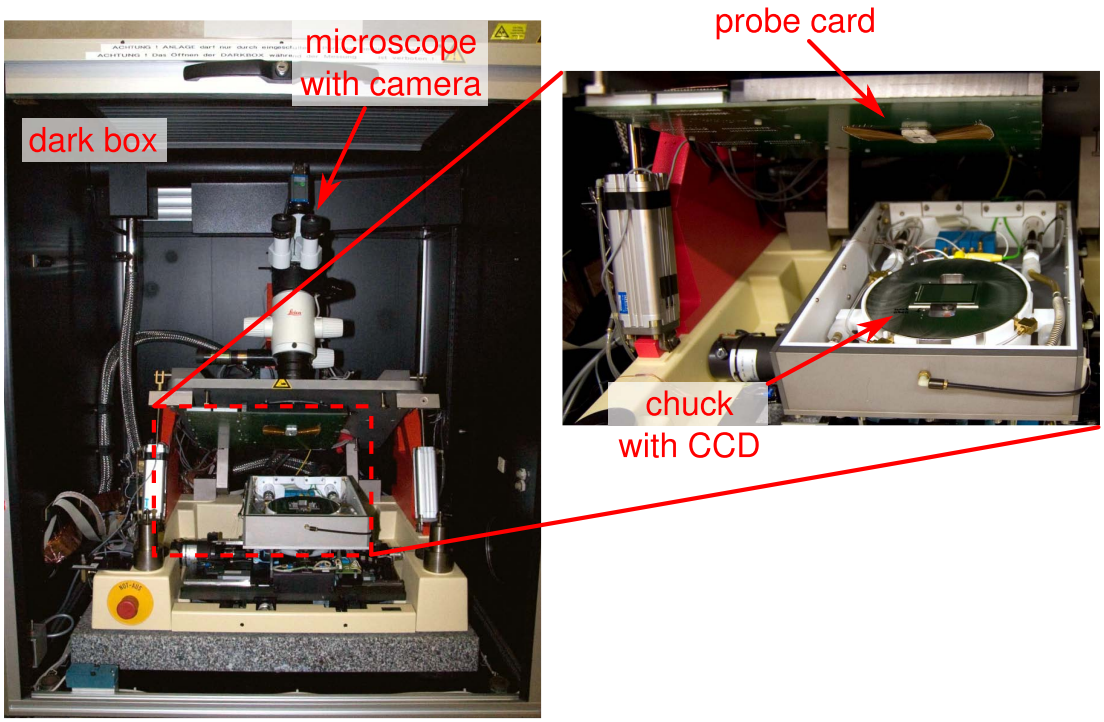

Figure 3.1: The dark box of the Cold Chuck Probe Station and a zoomed in picture showing the probe card and the chuck.

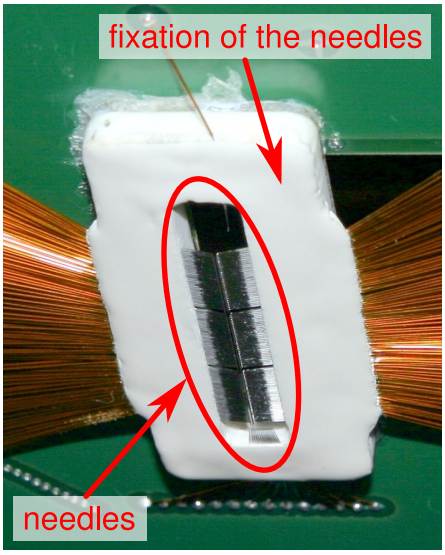

Figure 3.2: The needles mounted on the probe card. Through the needle contacts all operating voltages are supplied and the CCD signals are read out.

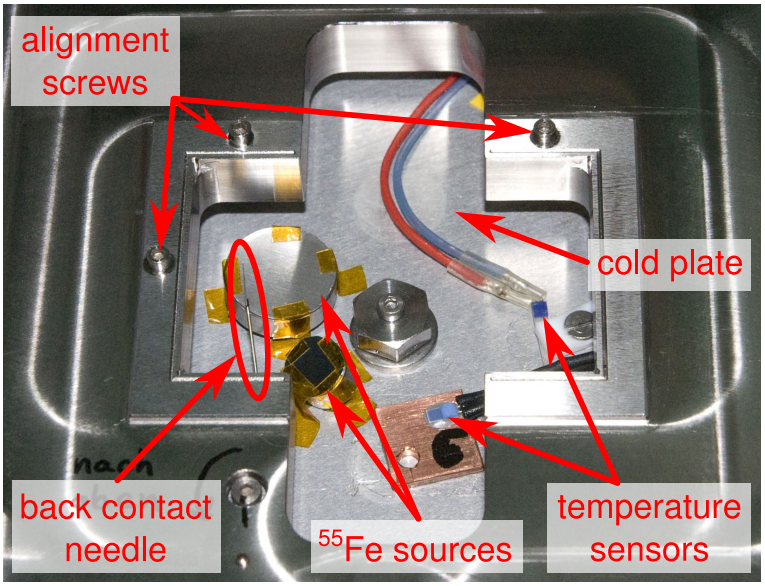

Figure 3.3: The chuck without a CCD. Through the hole the cold plate can be seen which is cooled with liquid nitrogen. On the cold plate the ^{55}Fe-sources for back side illumination and the temperature sensors are attached. The alignment screws are in the highest position which allow a safe placing of the CCD. Also the back contact needle which is mounted on the chuck can be seen.

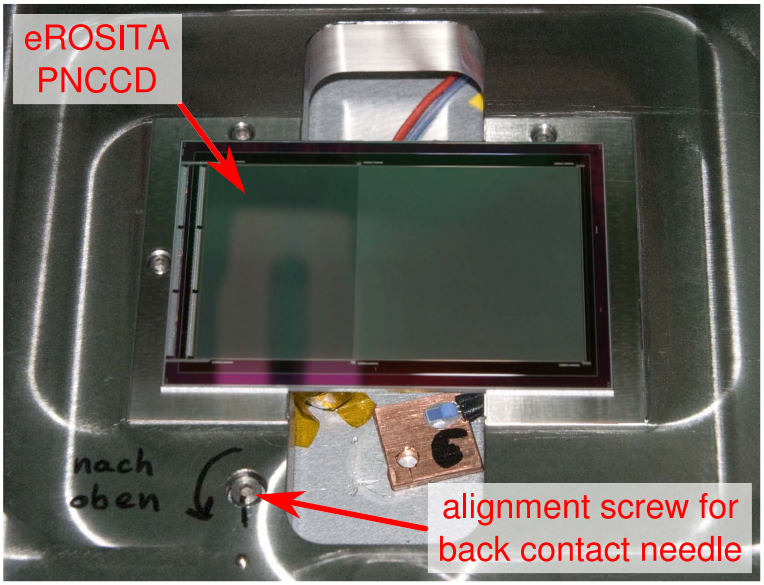

Figure 3.4: The chuck with a CCD placed on it. The alignment screw for the back contact needle which is used to adjust the height of the needle can be seen. Only the top of the alignment screws is visible as they are lowered down now in order to prevent a damage of the needles of the probe card.

As the PNCCDs are structured on both sides the chuck can hold the chip only on the insensitive edges. Alignment screws as shown in Fig. 3.3 allow a precise positioning of the chip on the chuck. Once the chip is placed on the chuck (see Fig. 3.4), a vacuum exhaust keeps it in position. After switching on the vacuum, the alignment screws are lowered down in order to avoid damaging the needles of the probe card during the measurement. With a dedicated screw it is possible to vary the height of the back contact needle. After placing the chip on the chuck, the back contact needle is lifted up until it touches the CCD. In order to contact the CCD with the needles of the probe card the chuck is moved upwards until the needles touch the bondpads. This is monitored by a microscope with a camera attached to it (see Fig. 3.1). For the alignment of chip and probe card the chuck can be moved in x-, y- and z-direction and also be rotated. The probe card itself can only be tilted with three screws in order to adjust the needles parallel to the chip.

3.1.1 Cooling

It is possible to cool the chuck with liquid nitrogen so that the CCDs can be measured at temperatures down to -70 °C which is close to the operating temperature in space. Lower temperatures are not possible as the risk of icing on the CCD is too high. To keep the CCD in a dry atmosphere, the dark box of the setup is flushed with nitrogen gas. The temperature sensor of the regulation is mounted on the cold plate of the chuck (see Fig. 3.3). To cross-check the temperature of the regulation two additional sensors are mounted on the cold plate during all measurements. As the temperature diode on the CCD is not contacted through needles, only the temperature of the cold plate is known during the measurements. Therefore, prior to the first measurements the temperature difference between the chip and the cold plate had to be calibrated. For the temperature calibration two temperature sensors were glued to a dummy CCD. The results of the temperature calibration can be seen in Fig. 3.5. At a cold plate temperature of about -80 °C a CCD temperature of about -70 °C is reached.

3.1.2 X-Ray Source

For the spectroscopic measurements the CCD is irradiated with 5.9 keV (Mn-K_α) and 6.5 keV (Mn-K_β) photons from four ^{55}Fe-sources. There are two possibilities to illuminate the CCD - from the front and from the back side - with different advantages and disadvantages. From the back side the CCD can only be illuminated inhomogeneously because of the close distance between the ^{55}Fe-sources and the chip. A further

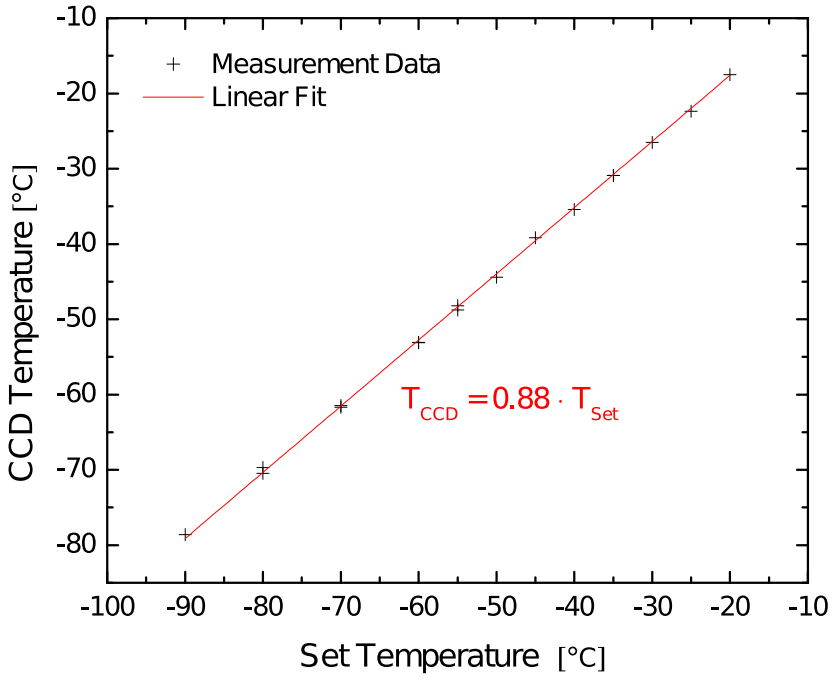

Figure 3.5: Temperature calibration curve. The CCD temperature was measured with a temperature sensor glued to a dummy CCD. The temperature of the cold plate is the set value of the regulation.

disadvantage is that the sources cannot be removed or covered during a measurement, so that no dark frames, i.e. frames without photons, can be recorded. Therefore the offset and noise map have to be calculated from photon frames. These disadvantages do not apply for the sources from the front side as they can be removed for calibration and the distance between source and chip is not so close. However, as the probe card is between CCD and source a shadow pattern is caused and about the first 200 rows cannot be irradiated at all.

To reach an illumination of all pixels and also as homogeneous as possible, two of the sources are placed underneath the chip and two are placed above the CCD and the probe card. In Fig. 3.6 a sketch of the position of the four ^{55}Fe-sources and the resulting intensity map is shown. The frame store (FS) area is mainly illuminated by the two sources from the back side whereas the image (IM) area is illuminated by the front side sources.

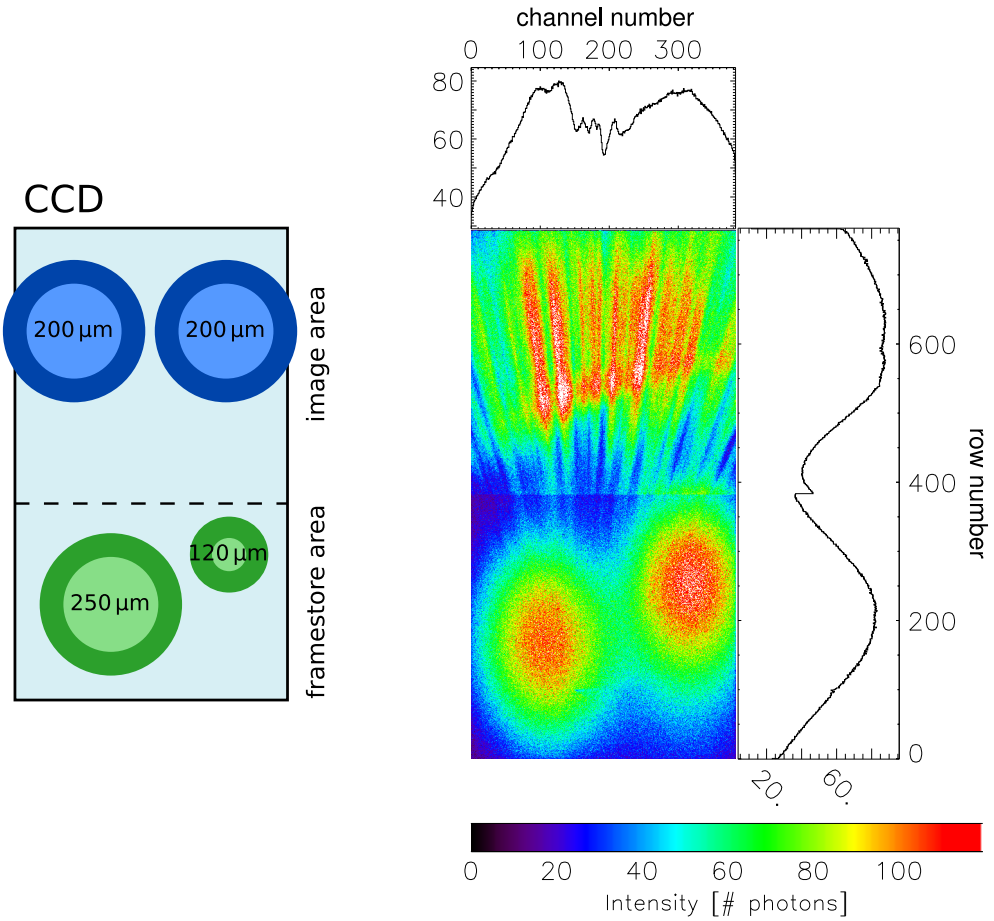

Figure 3.6: **On the left:** A sketch of the CCD showing the approximate positions of the ^{55}Fe-sources. The two sources which are marked green lay on the cold plate underneath the chuck, illuminating primarily the FS area from the back side. The blue sources are placed above the probe card and illuminate mainly the IM area. The dark colours mark the physical size of the source while the light colours mark the active area. The thickness of the Al foils reducing the intensity is written on each source.
On the right: Intensity map showing the resulting illumination which is not homogeneous. Nevertheless all pixels are irradiated. The shadow pattern in the IM area (upper half in the picture) is caused by the needles as the CCD is illuminated mainly from the front side. In the FS area (lower half) the two ^{55}Fe-sources illuminating the CCD from the back side can be seen. It should be noted that the pixels of the FS area are not plotted in the right aspect ratio as the rectangular pixels are plotted as square. Thus the shape of the back side sources looks like an oval. The smaller pixel size in the FS area also causes the little jump at the edge between FS and IM area which can be seen in the projection of the rows.

The three large sources have an activity of 740 MBq (Jan. 2009) and the small one has an activity of 12 MBq (May 2009). The photon intensity has to be adjusted to an appropriate level, i.e. as high as necessary to gain enough photons for the data analysis in a reasonable time and as low as possible to avoid pile-up. Therefor the photon flux of the ^{55}Fe-sources is reduced by 120 µm to 250 µm thick Al foils. As the absorption in the Al foil is higher for lower energies, the intensity of Mn-K$_\alpha$ is attenuated more than the one of Mn-K$_\beta$. Thus the heights of both peaks are nearly equal (see Fig. 3.7). On average about 2000 photons per frame are measured with this configuration in full frame mode operation with a cycle time of 200 ms. This rate allows for measurements with a sufficient number of events in a reasonable time with a pile-up rate of less than 1% of all events.

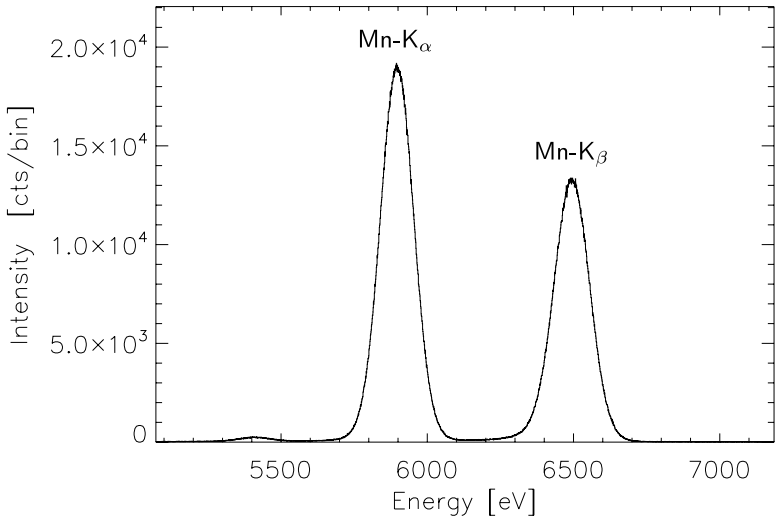

Figure 3.7: ^{55}Fe-spectrum measured with a CCD in the CCPS. The spectrum shows that the intensities of the Mn-K$_\alpha$ and Mn-K$_\beta$ peak are different by less than a factor of two due to the Al foils attenuating the source intensity.

3.2 Frontend Electronics and Data Acquisition

As explained in chapter 2.2 the CCD signal is read out by a CAMEX chip. Usually the CAMEX is mounted on a ceramic detector board close to the CCD [46] and is connected to the CCD directly via wire bonds. In this setup, however, such a close distance is not possible as the CCD is contacted by needles. Thus the CAMEX chips are mounted on custom boards specially designed for the CCPS, one board for each CAMEX chip (see Fig. 3.8). Three CAMEX boards are necessary which are connected

to the probe card (see Fig. 3.9). In this picture also a fourth PCB, the PHI board, plugged to the probe card can be seen. It houses the pulse drivers which generate the shift register pulses for transferring the charge in the CCD. Furthermore the PHI board routes the CCD voltages to the probe card.

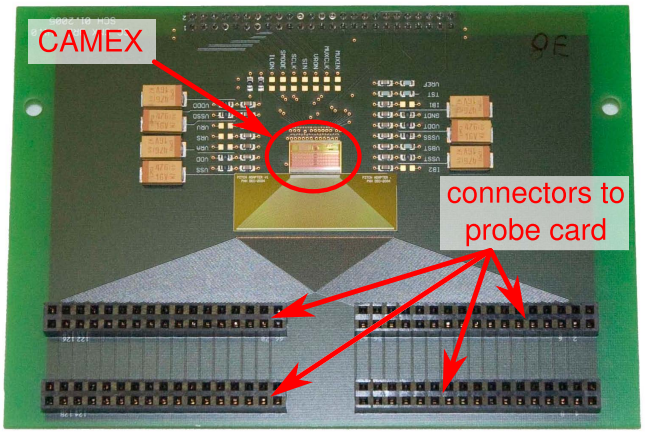

Figure 3.8: The bottom side of the CAMEX board where the CAMEX chip and the connectors to the probe card are mounted.

The analog output signals of the three CAMEX chips are digitised by a 14-bit ADC (**A**nalog to **D**igital **C**onverter). Thus the ADC covers a range of 0-16383 adu (**a**nalog to **d**igital **u**nits). The ADC cards were developed at the ZEL Jülich[1]. Each card has two ADC channels which means that two cards are needed to convert the output signals of all three CAMEX chips. Finally, the raw data, i.e. the adu value of each pixel of every frame, is sent to a PC and stored on hard disk. Thus no information is lost for the following data analysis.

The timing signals needed to synchronise the CCD, the CAMEX and the ADC are supplied by a sequencer which was also developed by the ZEL Jülich. It can generate up to 64 LVDS[2] signals and is freely programmable [47]. For the operation of the CCPS setup only 16 signals are needed. All voltages needed for the operation of CCD and CAMEX are provided by independent low noise power supplies.

[1] Zentralinstitut für Elektronik des Forschungszentrums Jülich
[2] Low Voltage Differential Signaling

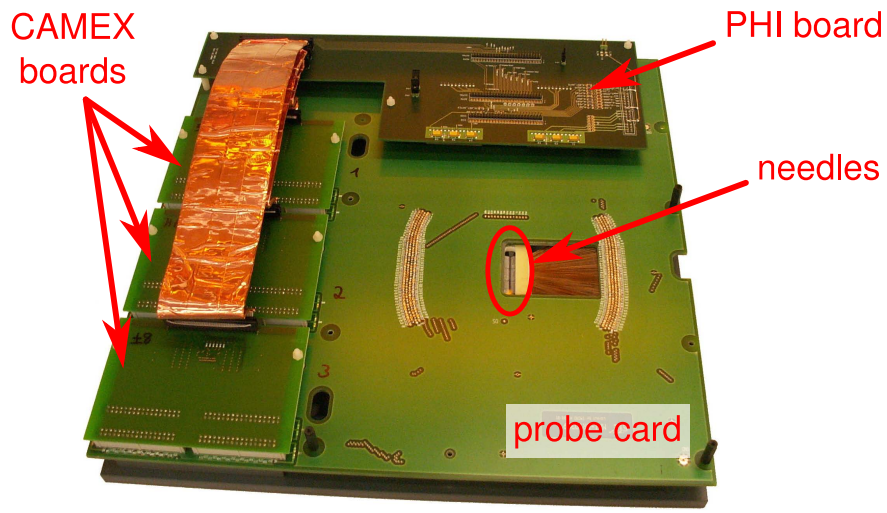

Figure 3.9: The Probe card with the three CAMEX boards and the PHI board plugged onto it. The CAMEX chips cannot be seen as they are mounted on the bottom side of the CAMEX boards. On the probe card also the back side of the needles can be seen and next to them the hole through which the CCD is irradiated from the front side.

3.3 Measurement Parameters

All eROSITA PNCCDs are measured with the same set of parameters at the CCPS. Additional measurements with varied parameters, e.g. the shift register amplitude voltage, are done if the chip shows a defect in order to investigate it further. If not noted otherwise the measurements are done under the conditions described in this section.

The CCD is measured at a temperature of -70 °C, both in frame store and full frame mode with a cycle time of about 200 ms. This is four times longer than the cycle time planned for the eROSITA mission and a compromise between the wish to differ as little as possible from the settings planned for eROSITA and the need to reduce the fraction of OOT events. At the CCPS not only the FF mode measurements suffer from a high OOT rate, but also the FS mode measurements. This is due to the ^{55}Fe sources underneath the FS area which cannot be covered and thus illuminate the FS area during the readout. The fraction of OOT events is about 10 % at a cycle time of about 200 ms.

The configuration of the ^{55}Fe sources - described in section 3.1.2 - leads to a photon rate of about 2000 photons per frame in FF mode and 1000 in FS mode. Although the illumination is inhomogeneous, this shows that it is distributed all over the chip, so that the IM and FS area are irradiated with the same rate. To obtain sufficient statistics for the following data analysis (see section 3.4) 3000 frames are written in each mode.

In a FS mode measurement the fast transfer of the signal charge from the image into the frame store area is slowed down by a factor of two compared to standard operation.

At the normal transfer speed the shift register pulses would not reach their full height fast enough as the long wires on the probe card increase the capacitance and thus lead to a slower rise time of the pulses. So the charge of one pixel would be smeared over several following pixels during the transfer which would make a reasonable data analysis impossible.

Due to the long wires on the probe card also the signal rise time is slower compared to a mounted CCD which is connected to the CAMEX with bond wires. Hence the time between the charge transfer to the anode and the signal sampling is adjusted to 6 µs, i.e. about three times longer than in standard operation, so that the full signal height is reached. Thus also crosstalk signals on neighbouring channels caused by capacitive coupling of the long wires on the probe card can be reduced as the crosstalk pulse decays shortly after the signal rising. For a better understanding, this is illustrated in Fig. 3.10.

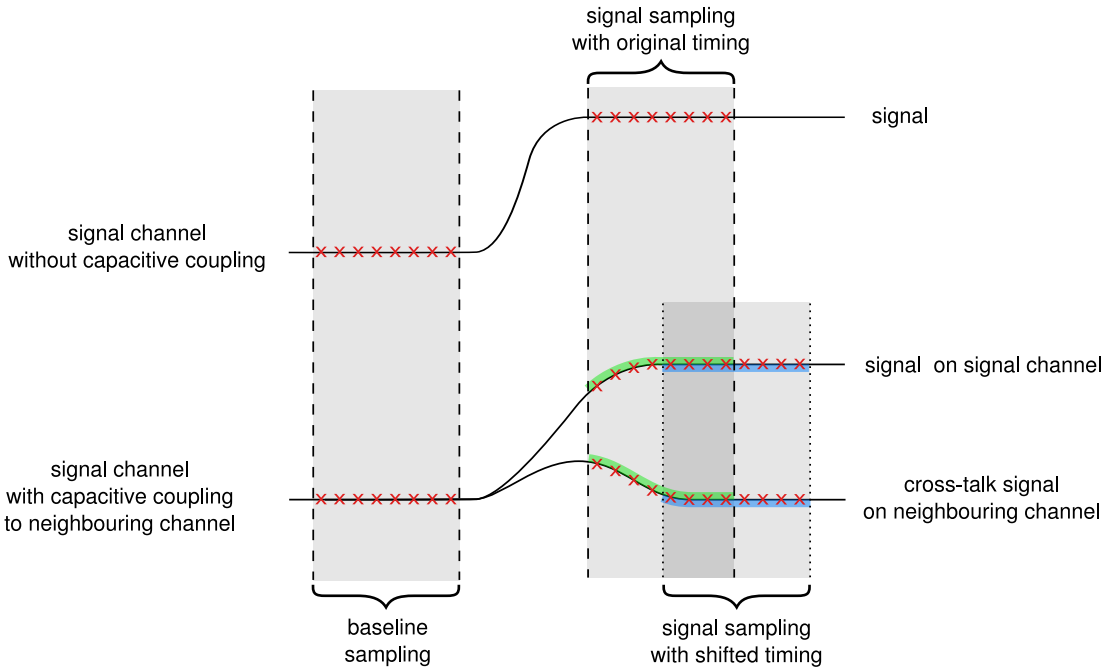

Figure 3.10: A signal pulse and the crosstalk on a capacitively coupled wire. If the signal sampling is done at a later time - i.e. the blue samples instead of the green ones - the signal has reached its full height and the crosstalk signal has decayed further.

The CAMEX chips are operated with the lowest bandwidth of 150 kHz to minimise the noise contribution. The second highest gain value is chosen which means an amplification factor of about 120. This is the highest possible gain at which the Mn-K_α and Mn-K_β peak are within the ADC range. For a good resolution it is essential to

choose the gain as high as possible.

The CCDs are operated with a voltage of -200 V at the back contact. For safety reasons this is less than the back contact voltage used later in eROSITA (which is planned to be -250 V). This difference may slightly affect the absolute performance of the CCDs, but as all of them are measured with the same set of parameters the results are comparable and allow to select the best ones. To generate the shift registers pulses two voltage levels are needed (see section 2.1.3) - V_{high} and the more negative one V_{low}. V_{high} corresponds to the supplied voltage called offset voltage, whereas V_{low} is realised by the sum of the offset voltage with another supplied voltage - the amplitude voltage. As the charge is transferred independently in the IM and the FS area two offset and two amplitude voltages have to be provided. For the offset voltage a value of -21 V and -19 V is chosen in the IM and FS area, respectively. The amplitude voltage is -6 V for both parts if not noted otherwise. More details on the CCD voltages can be found in appendix B.

3.4 Data Analysis

The measured raw data of PNCCDs is analysed by a software developed at the MPI-HLL. The different steps of the data analysis are described in the following. At first, the parameters offset, residual offset and noise are calculated. If possible, this is usually done from dark frames, i.e. frames without photon signals. As these parameters are individual for each pixel they are displayed in a map showing the whole CCD. In these maps the pixels in the FS area are not plotted in the right aspect ratio as the rectangular pixels are plotted as squares. Thus the FS area and the IM area appear at the same size in the maps. The rows and channels are numbered in the following way: the first row is the one closest to the anode. Thus the FS area covers the rows 0 to 383 and the IM area the rows 384 to 767. The channels are numbered from left to right looking at the front side.

The offset is the average value of a pixel over all dark frames. The residual offset map is calculated as follows: At first the median of each channel is subtracted from the offset map. Then, from this new map (offset - median of channel), the median of each row is calculated and also subtracted, resulting in the residual offset map. From the residual offset map, outstanding features such as bright pixels can be located easily.

To calculate the noise map, at first the offset is subtracted from each dark frame. Then a noise component common to all pixels of one row - the so-called common mode - is determined by calculating the median of each row. This common mode is

determined individually for each frame and is also subtracted from the dark frames. Now the noise σ for each pixel can be computed as the root mean square of the dark frames after subtraction of the offset and the common mode.

After calculating the offset, residual offset and noise map the event filtering can be started. Again the first step is to subtract the offset and the common mode from the raw frame data. Then one searches for all values which are above a threshold of four times the noise ($4\,\sigma$). The threshold should be high enough to suppress most of the noise events, but also as low as possible so that also small parts of a split event are detected. At a threshold of $4\,\sigma$, the fraction of noise events above the threshold is only 0.006 % assuming that the noise distribution has a Gaussian shape. Thus the probability of a noise event being part of an valid split pattern is very small and the distortion of the energy resolution by such events is negligible.

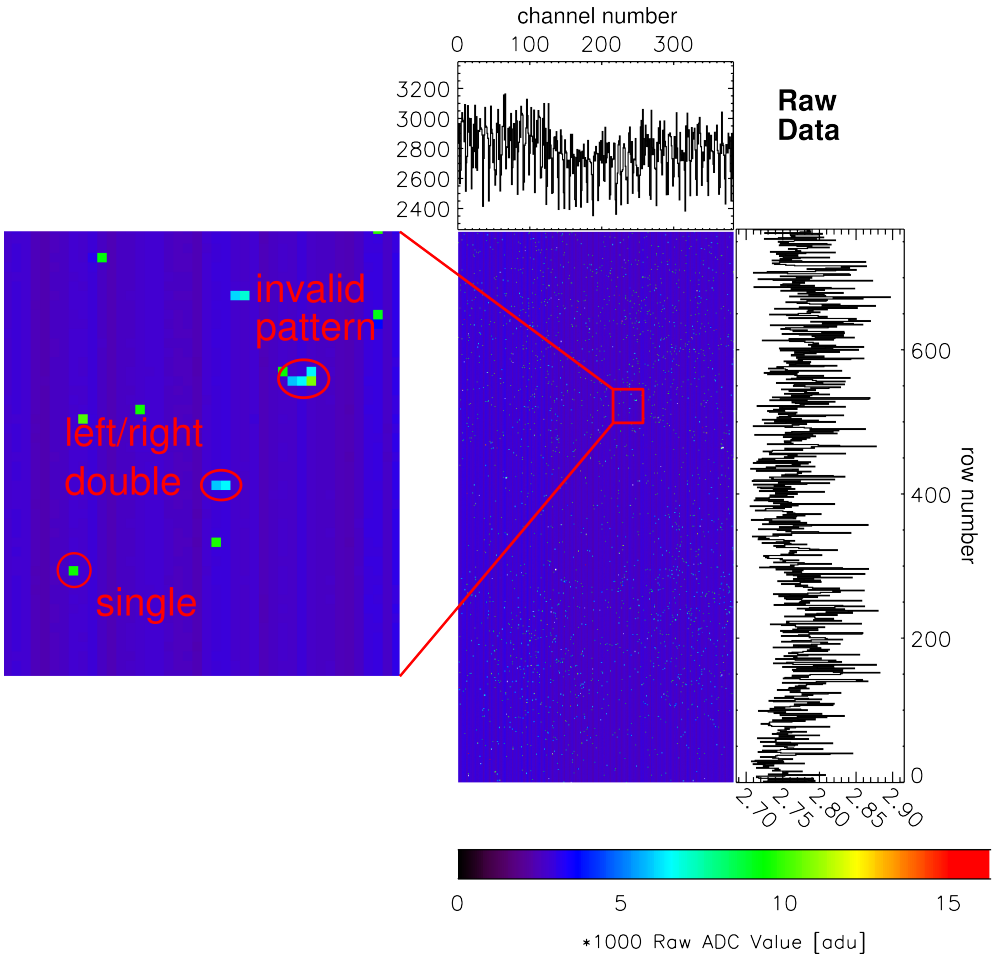

Figure 3.11: A raw data frame. In the zoomed area on the left different split patterns can be recognised.

As the setup does not allow to measure dark frames (see section 3.1), the parameters offset, residual offset and noise have to be calculated from frames with photon signals. An example of such a raw photon frame can be seen in Fig. 3.11. In the zoomed area in this figure different types of events are marked and labelled according to their split pattern.

The method used to calculate the offset and noise map out of photon frames works as follows. First of all, a first guess for the offset map is determined from the first 100 frames including the photon signals. Now from the next 100 frames the offset and common mode are subtracted and the first approximation of the noise map is calculated.

Then the next frame is taken and the events of this frame are filtered out. This means that all pixels with a signal greater than the threshold of 4 σ are left out, including their neighbour pixels. Skipping the neighbouring pixels as well prevents small signals from split events to distort the offset and noise map. If a pixel is left out, the offset and noise value are kept as before. For all other pixels a new offset and noise value is calculated as follows:

$$\text{new offset} = \frac{\text{old offset} \times 100 + \text{new frame}}{101}$$

$$\text{new noise} = \sqrt{\frac{(\text{old noise})^2 \times 100 + (\text{new frame})^2}{101}}$$

These two steps of event extraction and recalculation of the offset and noise map are repeated iteratively until the last frame of the input data. Thus one gets the final offset and noise map used for the event filtering. From the final offset map the residual offset is calculated. In Fig. 3.12 an example of the offset, the residual offset and the noise map of one PNCCD is shown. For illustration a measurement was selected inspecting a PNCCD with a defect. At a spot around row 390 and channel 260 a generation centre can be seen in all three maps. For more details on defects see chapters 5 and 6.

After calculating the offset, residual offset and noise map the valid events are filtered out. Then the extracted events are recombined, i.e. all events of one pattern are summed up, as the total energy of a photon is relevant for gain and CTE determination. For calculating gain and CTE only single events and forward-backward double split events are used as these events are only within one channel so no different gains are mixed up.

The procedure starts by estimating the gain of each channel through fitting a Gaussian to both the Mn-K$_\alpha$ and Mn-K$_\beta$ peak, assuming a CTE value of 1.0. In Fig. 3.13 a part of the spectrum (black line) of one channel with such a fit (green line) is shown. For the following gain and CTE calibration only the Mn-K$_\alpha$ peak is used which is

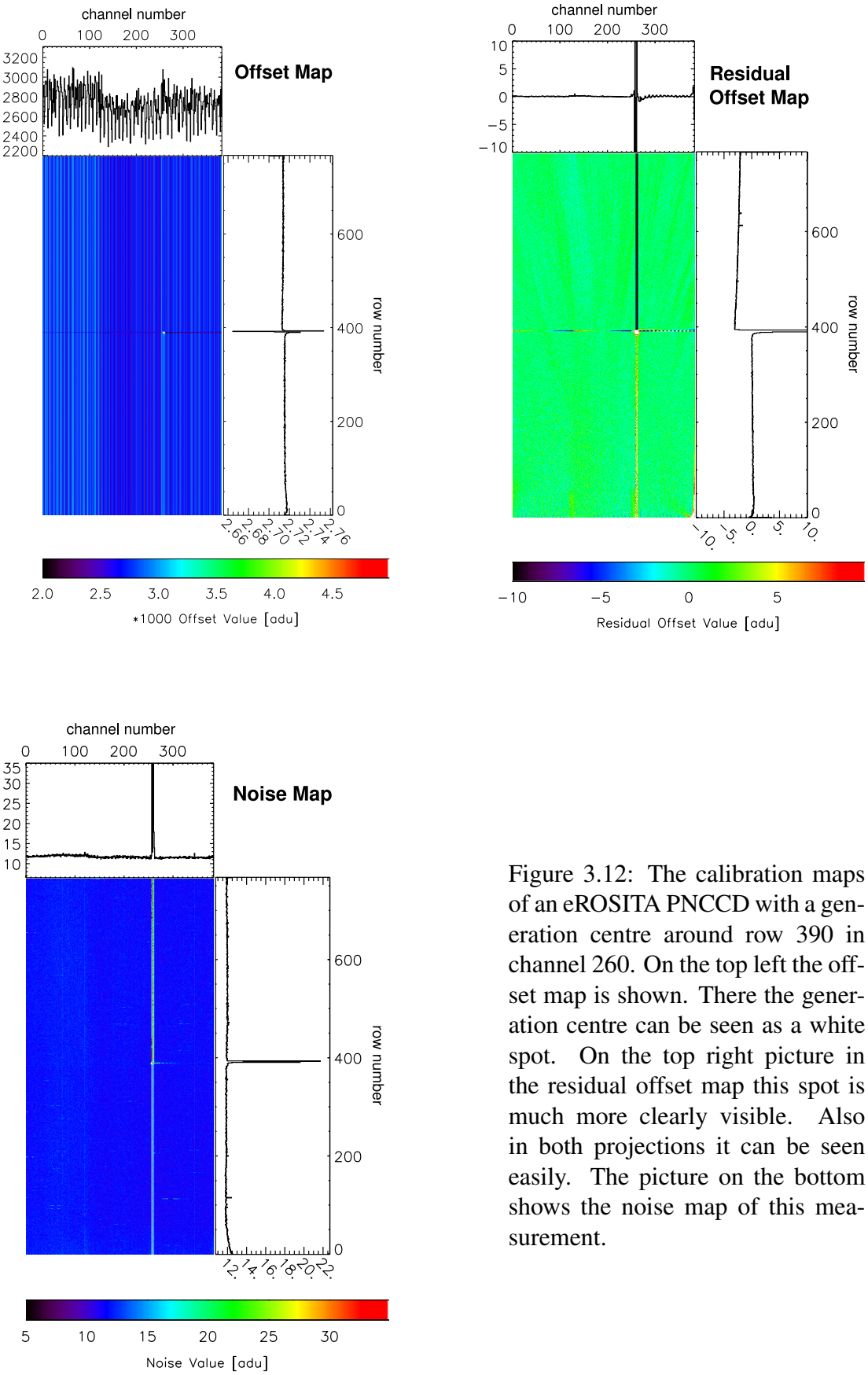

Figure 3.12: The calibration maps of an eROSITA PNCCD with a generation centre around row 390 in channel 260. On the top left the offset map is shown. There the generation centre can be seen as a white spot. On the top right picture in the residual offset map this spot is much more clearly visible. Also in both projections it can be seen easily. The picture on the bottom shows the noise map of this measurement.

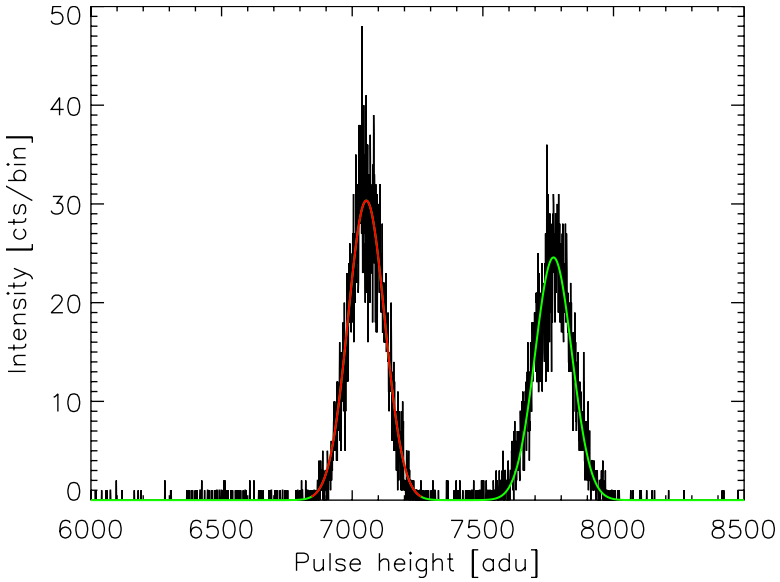

Figure 3.13: The spectrum of one channel with a Gaussian fit (green line) of Mn-K$_\alpha$ and Mn-K$_\beta$ peak in order to determine the start value of the gain. For the iterative gain and CTE fit only the Mn-K$_\alpha$ peak is used which is additionally coloured in red.

additionally coloured in red.

With the obtained starting value for the gain of each channel, the corresponding events are corrected. Then a global starting value (for all channels) for the CTE is calculated by fitting an exponential function through the amplitude values of all events (from all channels) as a function of the corresponding row number (as shown in Fig. 3.14).

Finally, from the starting value of the gain for each channel as well as the global starting value of the CTE, the gain and CTE are determined for each channel by fitting these values iteratively.

In Fig. 3.14 the gain-CTE fit for one channel of a FF mode measurement is shown. Through this fit one gets an individual gain and two CTE values for each channel as the CTE is determined for the FS and IM area independently. This distinction is reasonable as the pixel size is different in both areas which can lead to different CTEs. The only requirement is that the fit must have the same value at the border between FS and IM area. The exponents of the fits coloured in red and green yield the CTE of the FS and IM area, respectively. The axis intercept in Fig. 3.14 is proportional to the gain of this channel.

Only positive CTI values are physically reasonable, because charge can only be lost during the transfer and not picked up, i.e. the peak position at higher row numbers can

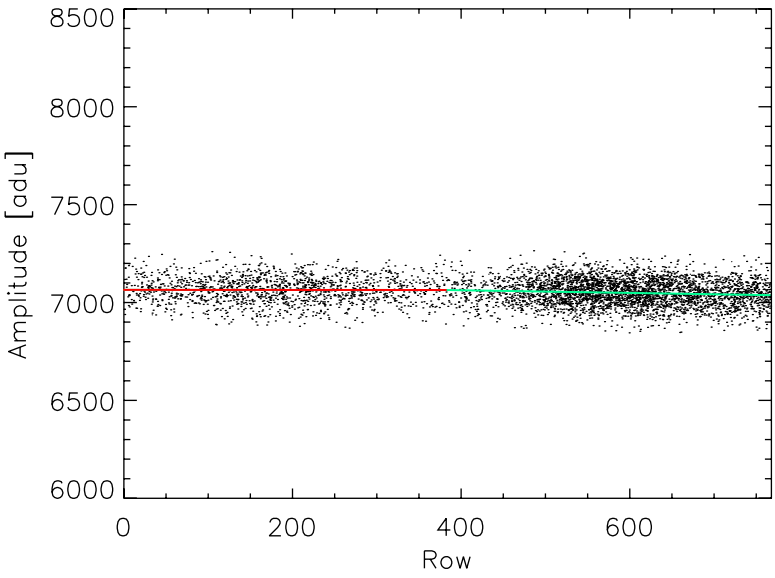

Figure 3.14: A scatter plot used for a CTE fit of one channel of an FF mode measurement. For each event a dot is drawn at the corresponding row and amplitude. The fit of the exponential function in the FS and IM area are shown in red respectively in green. The exponents of both parts correspond to the CTE of the respective area. The gain can be determined from the axis intercept.

only be lower. However, in the case of the CCPS it can happen that the peak position increases with higher row numbers. This effect is caused by the inhomogeneous illumination combined with the relatively high number of out of time events (OOT events). As explained in section 2.1.4 OOT events have either a higher or a lower signal amplitude than a normal event in the corresponding row. Thus the fit of the peak position in a certain region is distored as there is no possibility to distinguish between OOT events and normal events. In the first rows, OOT events move the signal amplitude to lower values whereas for the last rows, the amplitude is shifted to higher values. In addition, an inhomogeneous illumination leads to a varying ratio of OOT events to normal events. Both facts together can result in an increase of the peak position with higher row numbers, especially if the CTI and thus the changes in the peak position are small. In this case, the above fit can yield negative values for the CTI, if the fit parameter is not constrained to solely positive values. Such a constrained was not imposed in this analysis, i.e. negtive CTI values are possible. Adding this constraint would lead to a value of zero for the CTI in the respective cases. This, however, is not fully correct either and without the constraint, the affected cases can at least be identified. Anyway, the decision of whether or not to constrain the fit does hardly affect the other parameters. The differences between both methods for gain and energy resolution are smaller

than 1%.

The recombined events of all valid pattern are finally corrected with the obtained gain and CTE values before they are plotted in a spectrum. The energy resolution is then simply obtained from a Gaussian fit to the Mn-K_α peak.

Next to the parameters described above also bad pixels are determined during the data analysis. These are pixels which degrade the performance of the CCD by either generating charge or by transferring the charge incorrectly. The charge generating bad pixels can be divided into three groups according to their generation rate as described in the following. A pixel is called noisy if its noise is larger than twice the mean noise of all pixels. On the other hand, a bright pixel is defined to generate a charge of more than 0.3 e^-/ms. Finally, a very bright pixel has an offset of more than 10000 adu, i.e. a charge of more than 8 e^-/ms is generated. Thus with the electronics gain used in these measurements no signal detection of the Mn-K_α and Mn-K_β peak is possible because the ADC is in overflow. These charge generating pixel defects are described in more detail in chapter 5.

If only non-valid patterns or no events at all (except 10 % OOT events) are found after a pixel, it is called non-transferring (see chapter 6). Then a dark line can be seen in the intensity map of all valid patterns. Some pixels fulfil more than one of the above criteria and are counted for example as noisy and bright ones.

3.5 Verification of Concept and Construction

Some eROSITA CCDs which were used for different tests (e.g. radiation hardness tests) were measured both at the CCPS and another setup. There are two other setups which were used to test the CCDs, depending on their further planned use. In order to verify the reliability of the CCPS measurements, these results can be compared. Of course, the measurement conditions are not identical which should be kept in mind when comparing the results. In the next sections at first the other setups - RÖSTI and GEPARD - are described. Then a comparison of the setups and their results with the CCPS is given.

3.5.1 RÖSTI and GEPARD

RÖSTI

The RÖSTI test facility is a multi-target X-ray tube with a test chamber. As the name multi-target implies there are different targets, e.g. carbon and copper, which can be

used to generate fluorescence line spectra in the range from 277 eV to 8040 eV. With different filters the energy band can be limited to the required lines. The distance between X-ray tube and test chamber is about 4 m to ensure a flat field illumination of the CCD. In addition to the X-ray tube there is the possibility to irradiate the CCD with an ^{55}Fe source which is attached to a manipulator arm in the test chamber. Thus the source can be moved in and out of view as needed. A movable shutter allows to illuminate only the IM area (for FS mode measurements) or the whole CCD (for FF mode measurements).

The whole beam line is evacuated to a pressure below 10^{-6} mbar. Thus the X-rays are not absorbed by air and no ice will freeze on the cooled CCD. It is possible to cool the CCD with a cold head down to temperatures below -130 °C without any problems. The CCDs used for measurements at RÖSTI are mounted together with the CAMEX chips on a ceramic PCB which is then called detector test module. The ceramic boards of the test modules have pins on two sides for electrical and mechanical connection. The electronic setup used at RÖSTI is very similar to the one used at the CCPS.

GEPARD

In contrast to the RÖSTI test facility, the GEPARD test facility has no X-ray tube. There, the CCDs are solely irradiated with an ^{55}Fe source and, as the FS area is covered, only measurements in the FS mode are sensible. Again the CCD is in a vacuum chamber so that it can be cooled to low temperatures without the risk of icing on the module. While the RÖSTI test facility is designed for the measurements of test modules, GEPARD is used to test the flight detector modules and its development versions. These modules are mounted on a special ceramic which has no pins but is connected to a flex lead.

Differences between CCPS and RÖSTI/GEPARD

First of all, after the CCPS measurements a PNCCD is mounted on a PCB with its own CAMEX chips. The readout electronics is similar but not identical at the different test setups. The applied voltages are similar, but not identical either. Furthermore the timing varies. For example, the CCPS requires longer shift register pulses and a longer cycle time. The temperature at other setups is often lower than at the CCPS. Another major difference is the illumination. In the other setups, the illumination is not so inhomogeneous as at the CCPS. Secondly, the illumination modes are not mixed up in other setups in contrast to the CCPS where simultaneously the front and back side is illuminated. Thirdly the photon rate varies.

3.5.2 Comparison of the Obtained Results

To compare the different setups two eROSITA CCDs were chosen and measured both at the CCPS and at RÖSTI or GEPARD. The most important resulting parameters are compared in the tables below. Table 3.1 shows the results of an eROSITA CCD measured at the CCPS and RÖSTI. One can see that the difference for the CTI values is more than 10% for both the IM and the FS area. This is not surprising as the CTI correction at the CCPS suffers from the inhomogeneous irradiation as explained in section 3.4. The noise values, however, agree quite well with a difference of less than 3.5%. The single very bright pixel can be identified in both measurements. Bright and noisy pixels occurred only around the very bright one with slightly different numbers due to the difference of the noise - and thus the threshold - and the temperature. The CCD has no non-transferring pixel which was confirmed by the measurements of both setups.

parameter	CCPS	RÖSTI	difference
noise	$2.83\,e^-$	$2.74\,e^-$	3.2%
FWHM for single events	149,9 eV	137,6 eV	8.9%
CTI, IM area	$16 \cdot 10^{-6}$	$12 \cdot 10^{-6}$	25%
CTI, FS area	$19 \cdot 10^{-6}$	$21 \cdot 10^{-6}$	11%
gain	$1.16\,\frac{adu}{eV}$	$1.22\,\frac{adu}{eV}$	5.2%

Table 3.1: Results of a CCD measured at the CCPS and at RÖSTI.

In Fig. 3.15 the FWHM of single events of four different CCDs measured at the CCPS and RÖSTI are plotted. Only single events are used as the different illumination in the two setups leads to a different distribution of the split patterns (which may not all have the same energy resolution). The plot shows a reasonable correlation between the results from CCPS and RÖSTI, indicating that the CCPS results can indeed be used to compare the CCDs according to their energy resolutions.

The results of a CCD measured in FS mode at the CCPS and GEPARD are compared in table 3.2. The noise, gain and the FWHM of both measurements are quite similar, i.e. they vary by less than 5%. Solely the CTI values show a larger difference of 36%. Again this is explicable due to inhomogeneous irradiation at the CCPS. All four non-transferring pixels of this eROSITA CCD which were discovered by the CCPS measurements are confirmed by the GEPARD measurements.

To summarise, the measurements at the CCPS provide reliable results. The energy

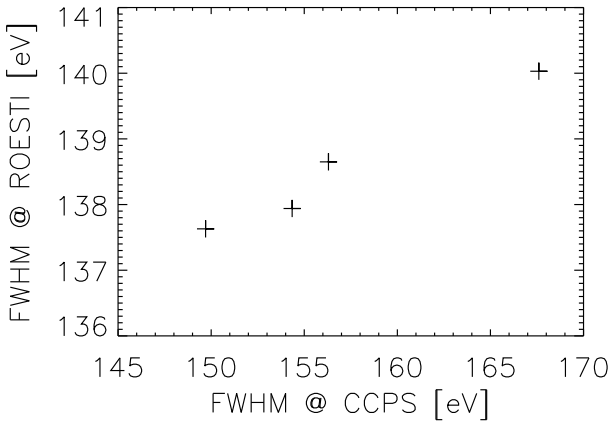

Figure 3.15: Energy resolution of four PNCCDs measured both at the CCPS and at RÖSTI. The energy resolution is the FWHM at 5.9 keV of single events in a FF mode measurement.

parameter	CCPS	GEPARD	difference [%]
noise	2.81 e^-	2.70 e^-	3.9%
FWHM for single events	130.9 eV	128.6 eV	1.8%
CTI	$6.2 \cdot 10^{-6}$	$4.0 \cdot 10^{-6}$	36%
gain	1.16 $\frac{adu}{eV}$	1.19 $\frac{adu}{eV}$	2.6%

Table 3.2: Results of a CCD measured at the CCPS and at GEPARD.

resolution at the CCPS is not as good as at RÖSTI and GEPARD, respectively. Nevertheless, the results can be used to compare different CCDs with respect to their energy resolution. All major pixel defects could be verified in the measurements with one of the other setups. Only minor pixel defects were partly not observed with RÖSTI or GEPARD as the temperature at these measurements was lower and so some noisy or bright pixels were below the threshold. Anyway, the CCPS can be used to determine the quality of each PNCCD and select the best ones for the eROSITA instrument.

4 Results and Statistical Evaluation

In the following chapter the results of the PNCCDs measured at the Cold Chuck Probe Station are summarised and compared with each other. Before the CCPS measurements all chips were tested for short circuits in a simple current-voltage measurement. Only the 63 eROSITA PNCCDs which passed this test were actually measured at the CCPS and are thus considered in this evaluation. In the first section, the determined properties of the CCDs such as noise, energy resolution, and charge transfer efficiency are presented. In the second section, the criteria for the selection of the best CCDs are defined and the CCDs are valuated.

4.1 Results

4.1.1 Noise

The noise is calculated individually for each pixel of a PNCCD. To compare the noise of different CCDs the mean value of all pixels is calculated. In Fig. 4.1, a histogram of all measured mean noise values at -70 °C is shown. The values range from 2.5 e^- to 5.2 e^-, with an accumulation of samples in the bin between 2.7 e^- and 2.8 e^-. The mean noise of all CCDs measured at the CCPS is 2.9 e^- with a standard deviation of 0.5 e^-. This is similar to results achieved with other setups (see section 3.5) although at the CCPS the CCD is contacted with needles instead of bond wires.

All CCDs with a noise higher than 3.1 e^- have a major pixel defect such as a charge generation centre or a non-transferring pixel. These defects can cause a lot of noisy pixels and thus shift the mean noise to a larger value. In case of a generation centre, all pixels of the channel pass the defect during the transfer and may get some of the randomly generated charge. This largely varying amount of charge in the pixels leads to a higher noise. In case of a non-transferring pixel on the other hand, the charge generated by a photon is sometimes transferred badly and smeared over several pixels in this channel. If the transferred amount of charge in a pixel is below the event cut, it is not recognized as part of an event and used for the calculation of the noise. Hence the noise is increased.

The majority of the CCDs (about 84 %) has a noise lower than $3.0\,e^-$. Also the variation between these CCDs is small and thus the noise is not a good criterion to identify the very best ones among them.

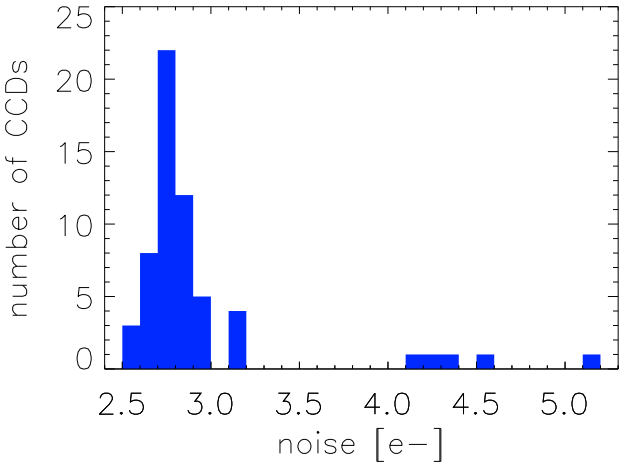

Figure 4.1: A histogram showing the distribution of the mean noise values of all PNCCDs which were measured at the CCPS.

4.1.2 CTI

The following statistical analysis of the charge transfer inefficiency, the energy resolution and the gain considers only those CCDs for which these parameters could be determined for the whole CCD. Whenever these parameters could only be calculated for some parts of the device, for example due to a large charge generation center, the mean value of these parameters is affected and these CCDs are thus not included in the following.

An important parameter to characterise the PNCCDs is the charge transfer inefficiency (CTI). Two CTI values are determined in a full frame (FF) mode measurement, one for the image (IM) and one for the frame store (FS) area (see section 3.4). Fig. 4.2 shows a histogram of all CTI values in the IM area. The total range stretches from $-5 \cdot 10^{-6}$ to $40 \cdot 10^{-6}$ with a peak at around $10 \cdot 10^{-6}$. The mean value is $15 \cdot 10^{-6}$ with a standard deviation over all samples of $11 \cdot 10^{-6}$. As already explained in section 3.4, the negative CTI values are due to the inhomogeneous illumination and the relatively high number of OOT events in the current setup. Note that the absolute values in all cases with negative CTI are only small ($\leq 5 \cdot 10^{-6}$).

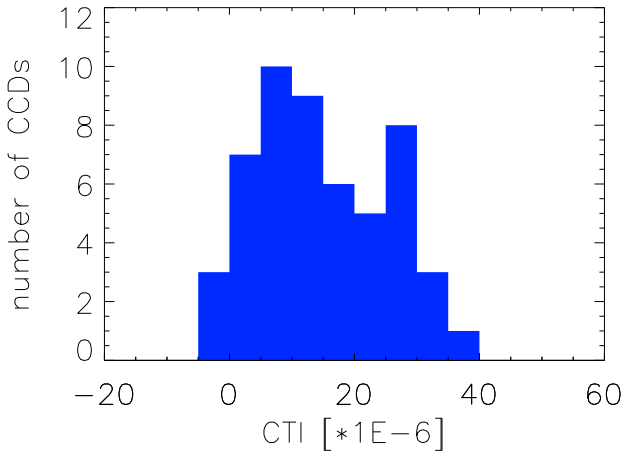

Figure 4.2: A histogram with all CTI values measured in the IM area in a FF mode measurement.

The distribution of the CTI in the FS area is quite similar as can be seen in Fig. 4.3. There, the values run from $-5 \cdot 10^{-6}$ to $45 \cdot 10^{-6}$ with an average value of $13 \cdot 10^{-6}$ and a standard deviation of $11 \cdot 10^{-6}$. The CTIs of the IM and FS area are not as different as one might expect. Due to the different pixel size in both parts the charge has to cover a shorter distance in the FS area than in the IM area. Assuming a homogeneous distribution of traps this should lead to a smaller CTI in the FS area - an effect which, however, seems to be small according to the measurement results.

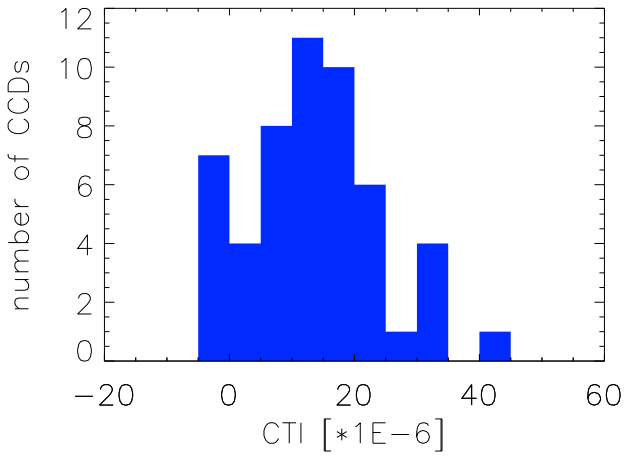

Figure 4.3: A histogram illustrating the distribution of all CTI values of the FS area in a FF mode measurement.

4.1.3 Energy Resolution

The energy resolution is defined here as the FWHM of the Mn-K$_\alpha$ line. For full frame mode measurements at -70 °C the energy resolution distributes from 135 eV to 195 eV as can be seen in Fig. 4.4. The mean energy resolution is 160 eV with a standard deviation of 15 eV. Compared to other setups such as RÖSTI the mean value is worse and the variation between the individual samples is larger. This was expected since the inhomogeneous illumination and the higher number of OOT events affects the CTI correction and thus worsens the energy resolution. Nevertheless, the best values reached with the CCPS show that for a good CTE also a good energy resolution is reached.

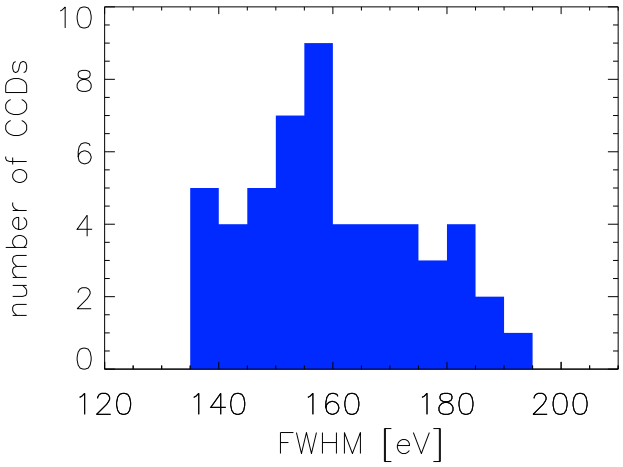

Figure 4.4: A histogram showing the distribution of the energy resolution measured at the CCPS of all PNCCDs where this parameter could be determind for the whole chip. Here, the energy resolution is the FWHM of the Mn-K$_\alpha$ line in a FF mode measurement at -70 °C.

The plot in Fig. 4.5 shows the FWHM as a function of the CTI. The two parameters show a clear correlation. In order to identify the best CCDs, it is thus sufficient to consider only one of the two - in this case the FWHM - as a criterion.

Finally, it is also interesting to study the distribution of the FWHM within one wafer and between the wafers. Fig. 4.6 illustrates the spread within the wafers. In about 60 % of the wafers, the range of all measured FWHM values is smaller than 10 eV, whereas the remaining 40 % exhibit larger spreads. Some of these wafers are split into one part with a good energy resolution and another part with a worse one, for example wafer 3.

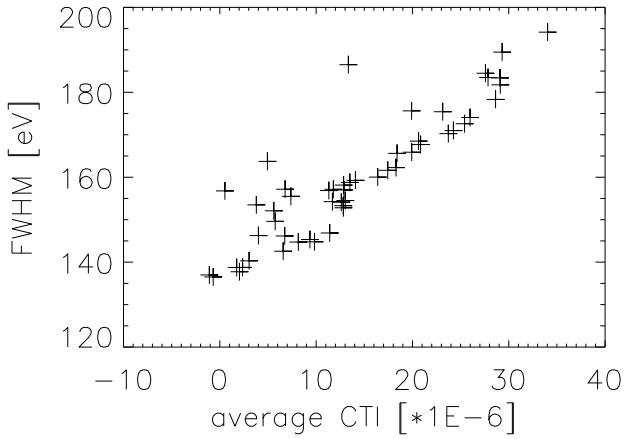

Figure 4.5: In this diagram the energy resolution of a FF mode measurement versus the average CTI is shown. The energy resolution is clearly correlated to the CTI.

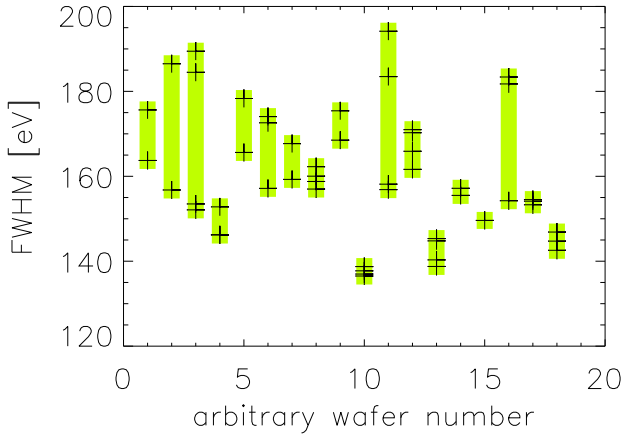

Figure 4.6: Distribution of the FWHM between the wafers. The wafer numbers are chosen arbitrarily. The FWHM was measured at -70 °C in FF mode. Crosses indicate the measured values of the individual CCDs while the green bars illustrate the spread within the respective wafer.

To investigate this further, the distribution of the FWHM with respect to the chip position on the wafer is analysed. Each wafer has four eROSITA CCDs which are named as illustrated in Fig. 4.7. In Fig. 4.8 the FWHM is plotted against the chip position on the wafer. The range at position 33 is smaller than for the others positions. The spread at position 32, for example, is about 80 % larger. Thus, in average the FWHM at position 32 is worse than at position 33.

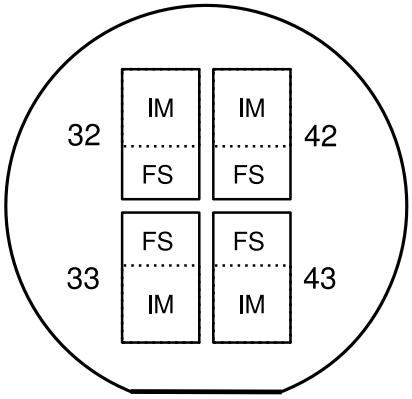

Figure 4.7: A sketch showing roughly the position of the eROSITA PNCCDs on the wafer.

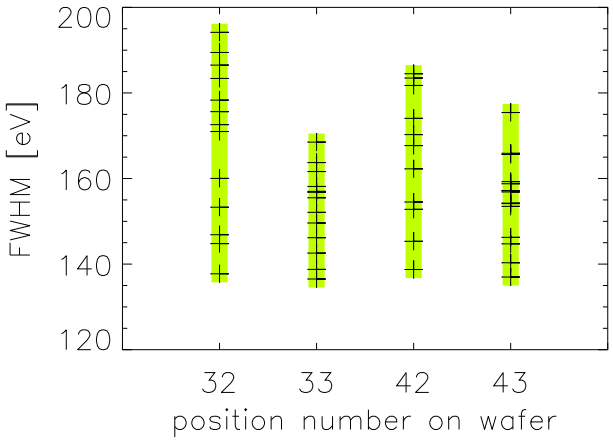

Figure 4.8: FWHM vs. the chip position on the wafer for all wafers. The energy resolution was measured at a temperature of -70 °C in FF mode. Each cross mark the FWHM of one PNCCD. The green bars indicate the spread within the respective position.

To investigate this inhomogeneity further the energy resolution of the six wafers from which all four PNCCDs were measured was analysed in more detail. Therefor,

each CCD was divided into six parts. The FS and the IM area were separated and each divided into three channel blocks, namely from channel 1-128, 129-256 and 257-384. For all six parts the energy resolution was then calculated individually, i.e. 24 values for the energy resolution on the whole wafer. The results for all investigated wafers are shown in Fig. 4.9. It should be noted that the color coding is adjusted between the minimum and the maximum value observed in each wafer individually.

There is a clear tendency (with the exception of the wafer shown in the lower right corner) to observe the worst FWHM in the IM area of the positions 32 and 42. The largest spread across the wafer is thereby seen for the two wafers shown on the top. Only the two wafers on the bottom reveal areas where the energy resolution of the IM area is better than in the corresponding FS area. This contradicts the expectation that the FWHM in the IM area is worse than in the FS area because the charge of the IM area suffers from more charge losses due to the higher number of transfers.

An explanation of the relatively large and partly systematic variation of the FWHM across the wafers could not be found yet. Likely some production steps are not as homogeneous as intended but further investigations are necessary to determine the cause of this inhomogeneity.

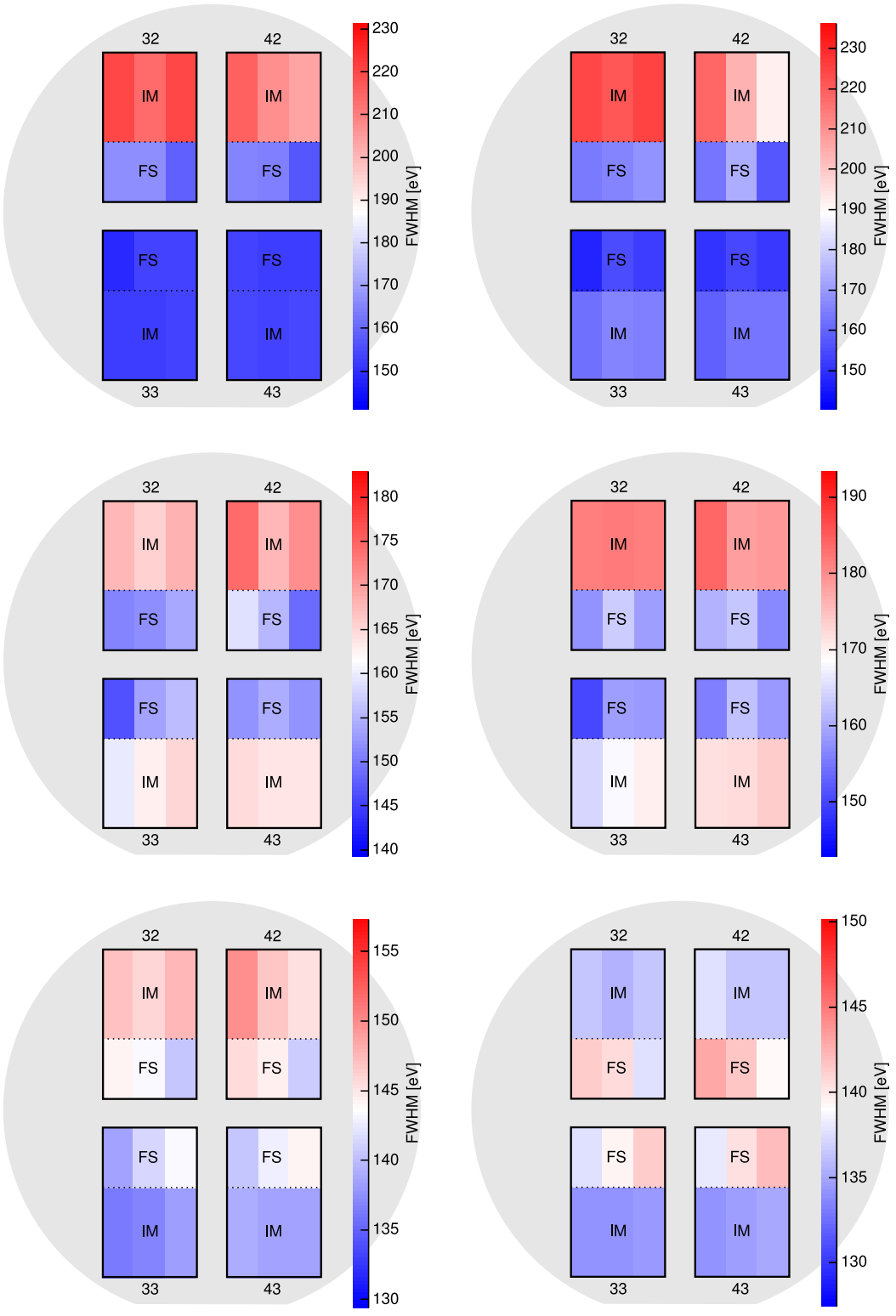

Figure 4.9: This diagram shows the distribution of the FWHM on six different wafers where all CCDs were measured. For each CCD the FWHM was calculated for six parts. Note that the color coding is adapted to the minimal and maximal value for each wafer individually.

4.1.4 Gain

The gain of each CCD detector module arises from the combination of the CAMEX and the on-chip electronics. Thus the gains of different modules usually cannot be compared independently. However, at the CCPS, all CCDs were measured with the same set of CAMEX chips operated with identical voltages. Thus the distribution of all gain values shown in Fig. 4.10 represents the distribution of the CCD gains. The mean value of the gain is 1.18 adu/eV with a standard deviation of only 0.02 adu/eV among the samples. There are thus no great variations between the CCD gains.

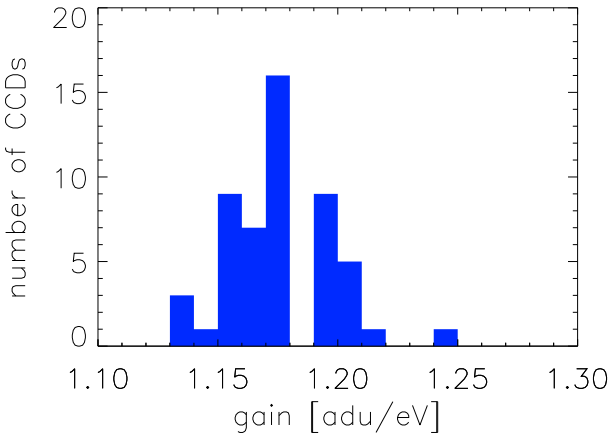

Figure 4.10: A histogram of all gain values determined with the CCPS measurements. It represents the distribution of the CCD gains as all were measured with identical CAMEX chips.

4.1.5 Pixel Defects

Next to the global parameters characterising the whole PNCCD there are pixel defects influencing the performance. In general one can distinguish two different categories - charge generating defects and non-transferring pixels.

The charge generating defects can be further divided into three different groups - noisy, bright and very bright - according to the amount of generated charge. The thresholds were already defined in section 3.4 as follows:

- noisy: noise greater than twice the mean noise
- bright: charge generation rate of more than 0.3 e^-/ms
- very bright: offset larger than 10000 adu (i.e. a generation rate of about 8 e^-/ms)

14% of all eROSITA PNCCDs have no noisy pixels and 60% have less than 10 noisy pixels. All CCDs with 10 or more noisy pixels have a very bright oder non-transferring pixel which cause most of the noisy pixels. At a very bright pixel a defect generates charge, also during the charge transfer. Hence, all pixels in the channel of the very bright one can get some charge of the generation centre. As the charge generation at the defect is a statistical process the amount of charge varies, thus increasing the noise. If the charge is transferred incompletely by a non-transferring pixel, small charge packages below the event cut cannot be filtered out by the data analysis software. Thus the amount of charge detected in the pixels behind the non-transferring one fluctuates, again resulting in an increased noise.

The next group of charge generating defects are bright pixels with a generation rate of more than $0.3\,\mathrm{e^-/ms}$. About 29% of the eROSITA CCDs have no bright pixel. 71% of the CCDs show not more than 10 bright pixels. Higher numbers of bright pixels are correlated to a charge generation centre causing several very bright pixels. The bright pixels - generating not as much charge as the very bright pixels - are clustered around the very bright ones.

48% of all CCDs have at least one very bright pixel, but only 17% have more than 30 very bright pixels. In Fig. 4.11 the distribution of the very bright pixels on the wafers is shown. Each colour stands for one wafer number. At the chip position 33 the fewest very bright pixel were detected. Three very bright pixels in the IM area on two different wafers occurred and no very bright pixels in the frame store area. At the other positions the very bright pixels are distributed all over the chips. A clustering of very bright pixels can be observed at the border between the IM and the FS area at the position 42 and 43. These were caused by a wafer holder of an implanter touching the chip during the production process. Thus the crystal structure was damaged leading to the charge generation centre.

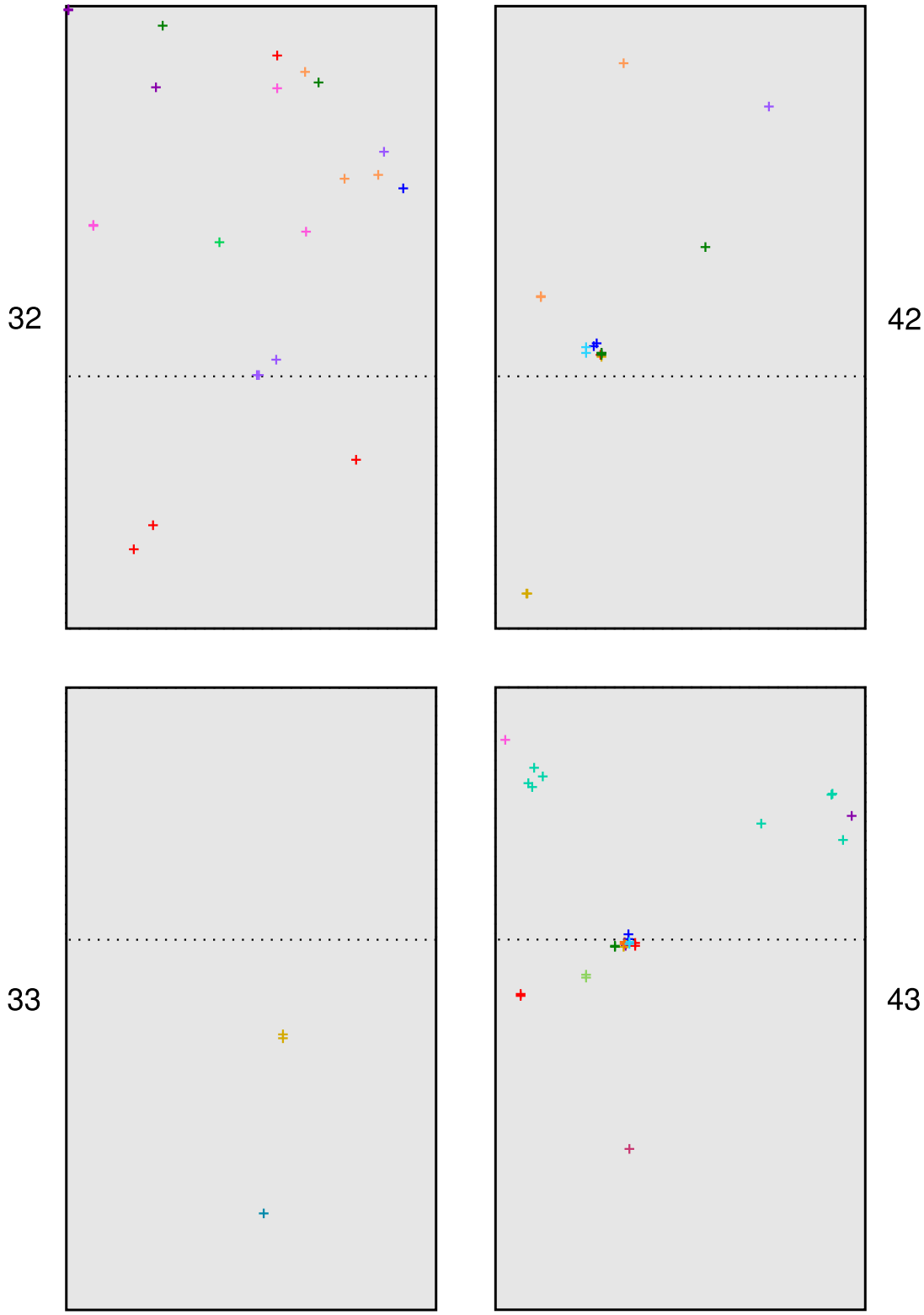

Figure 4.11: A sketch showing the distribution of the very bright pixels of all CCDs over the wafer. Each colour denotes a wafer. At position 42 and 43 a cluster of very bright pixels can be seen near the border between IM and FS area. There a wafer holder of an implanter touched the wafer damaging the crystal lattice.

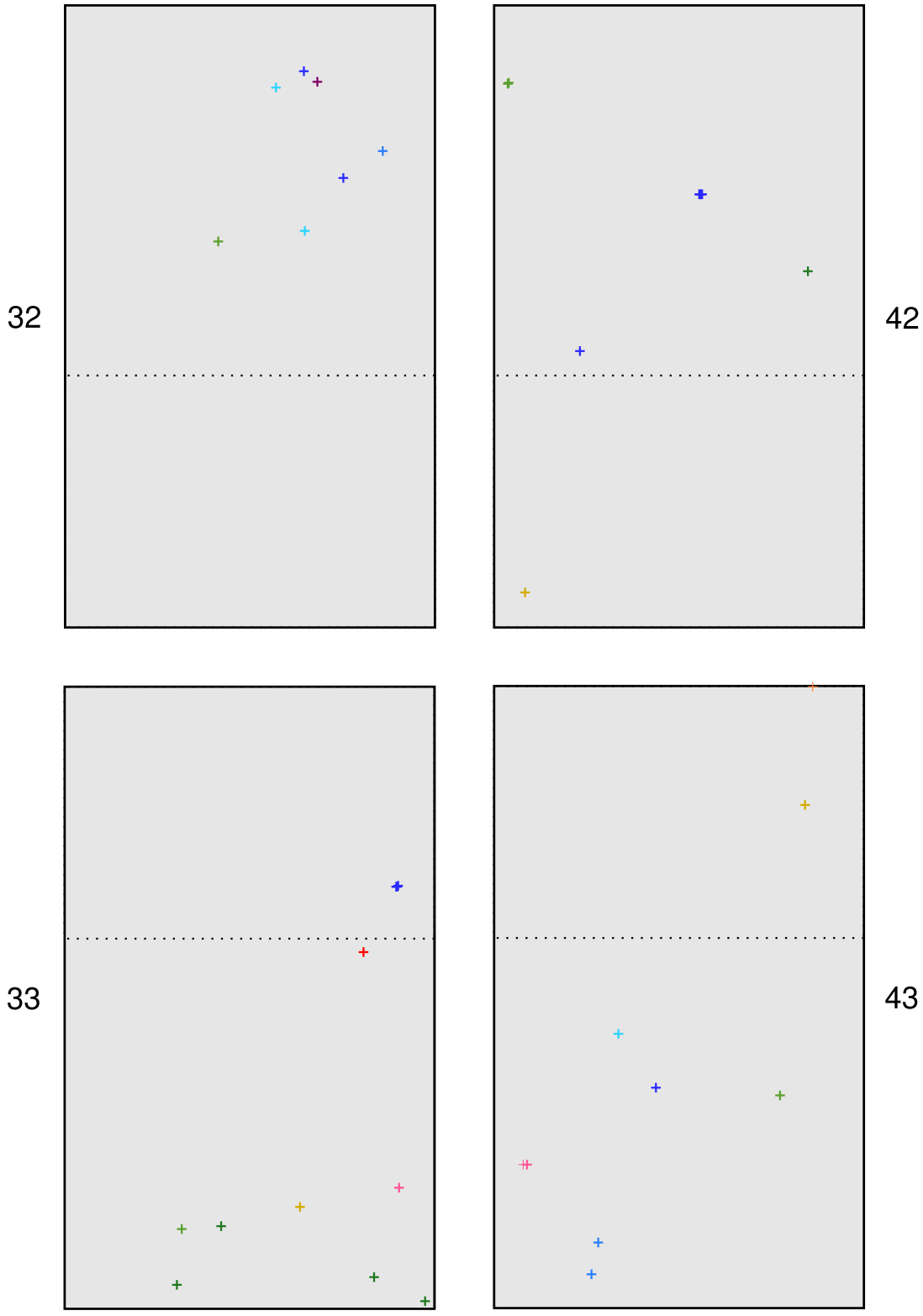

Figure 4.12: A map of the wafer with the position of all non-transferring pixels marked by a cross. The different colours stand for the different wafers.

At a non-transferring pixel the charge is transferred incompletely or not at all. So no valid events are detected in all pixels in the channel behind the non-transferring one. In total about 35% of all measured eROSITA PNCCDs have at least one non-transferring pixel. Only 10% have more than two non-transferring pixels. The map in Fig. 4.12 shows the spatial distribution over the wafer of all non-transferring pixels on all the wafers. Each colour depicts one wafer. One can see that most of the non-transferring pixels are located in the image area. The CCDs of position 42 have the fewest non-transferring pixels. At position 33 nearly all non-transferring pixels can be found in the last third (rows 640-767) of the IM area. Thus less than 130 pixels are lost for the image because of their position in the channel behind the non-transferring one.

More details on pixel defects can be found in chapter 5 and 6 for charge generating defects and non-transferring pixels, respectively.

4.2 Selection

4.2.1 Selection Criteria

With the results obtained from the CCPS measurements the PNCCDs are comprehensively characterised and it is thus possible to choose the best ones for the eROSITA detector modules. For this purpose, the CCDs are sorted into the following categories according to their energy resolution and their major pixel defects:

- The very good or '+ + +' CCDs have a very small CTI and thus an energy resolution of 145 eV or better is achieved at the CCPS. Also no major pixel defects (such as very bright or non-transferring pixels) are detected. Only a few bright or noisy pixels are allowed.

- In the next category ('+ +'), a few major defects are tolerated (30 very bright and 10 pixels after a non-transferring one). As the number of very bright pixels will decrease with a lower temperature and a shorter cycle time, more very bright than non-transferring pixels are allowed. The energy resolution has to be better than 160 eV.

- The CCDs of a medium quality are sorted into the category '+'. There, an energy resolution of 185 eV or better is required. PNCCDs of this category can have 300 very bright pixels at most and 100 pixels after non-transferring ones.

- Bad PNCCDs (category '-') have a FWHM of up to 200 eV or up to 384 pixels

after non-transferring ones in the IM area. Furthermore larger charge generation centres can occur which means more very bright pixels (≤ 3000).

- CCDs with a very bad CTI and therefore an energy resolution of more than 200 eV can be found in the category '- -'. Also more pixels after non-transferring ones are allowed as well as a higher number of very bright pixels.
- CCDs of the quality '- - -' are not working properly, e.g. because of short cuts or huge generation centres (i.e. a large number of pixels is in the ADC overflow). Hence, no reasonable spectroscopic measurements are possible.

An overview of all evaluation categories including their specifications is given in table 4.1. As the usual measurement mode for eROSITA is the frame store mode, the energy resolution used for the evaluation is the FWHM of a FS mode measurement. Also the number of pixels after non-transferring pixels is taken from a FS mode measurement. Hence, for a non-transferring pixel located in the FS area, the total relevant number of pixels behind this defect is 384 (all pixels of this channel in the IM area). For very bright pixels, on the other hand, the number observed in a FF mode measurement is considered. Even if located in the FS area, a very bright pixel will also generate charge after the transfer of the image to the FS area and thus distort the image. Therefore, these pixels cannot be neglected in the evaluation of the CCDs.

quality	FWHM (FS mode)	number of very bright pixels (FF mode)	number of pixels after non-transferring pixels (FS mode)
+ + +	≤ 145	0	0
+ +	≤ 160	≤ 30	≤ 10
+	≤ 185	≤ 300	≤ 100
-	≤ 200	≤ 3000	≤ 384
- -	> 200	$3000 < n \leq 30000$	> 384
- - -	no spectroscopic measurement possible		

Table 4.1: The selection criteria which were used to sort the measured CCDs into six different categories according to their performance.

4.2.2 Yield

All PNCCDs measured at the CCPS were evaluated as described in the previous section. Altogether 63 chips were evaluated and their distribution over the six quality

quality	number of CCDs (measured at CCPS)	yield (in %)
+ + +	9	14
+ +	11	18
+	12	19
-	20	32
- -	7	11
- - -	4	6

Table 4.2: Yield of the eROSITA PNCCDs measured with the CCPS.

categories is shown in table 4.2.

Four of the PNCCDs did not allow reasonable spectroscopic measurements, due to huge generation centres causing a large amount of very bright pixels. About 11% delivered quite poor results ('- -'). In the next category ('-') 32% of the 63 chips can be found. Most of the CCDs were sorted into this category because of the number of pixels after a non-transferring one. 19% and 18% of all CCDs, respectively, are of medium and good quality and 14% are of a very good quality.

For the eROSITA flight modules seven of the nine very good chips should be chosen. If needed, there are still eleven additional good PNCCDs which would also be appropriate for the flight instrument.

5 Charge Generating Defects

The following two chapters describe some defects which were observed during the CCPS measurements in more detail. In this chapter charge generating pixel defects, e.g. bright pixels, are analysed, whereas in chapter 6 non-transferring pixels are investigated.

The charge generating defects are distinguished in noisy, bright and very bright according to the amount of generated charge. The thresholds were already defined in chapter 3. Some figures on the occurrence of these pixel defects and their distribution were given in section 4.1.5 of the previous chapter. In this chapter a comparison to the Shockley-Read-Hall Model follows. Furthermore the influence of the back contact voltage on the amount of generated charge is investigated.

5.1 Temperature Dependence

5.1.1 Shockley-Read-Hall Model

The charge generation and recombination in a semiconductor is described by the Shockley-Read-Hall Model [48], [49]. It explains the charge generation and recombination through an energy level within the bandgap - called trap - by four basic processes. These are depicted in Fig. 5.1. The electron capture and electron emission describe the transition of an electron from the conduction band to the trap and vice versa. The transition of an electron from the trap to the valence band is called a hole capture, whereas the electron transition from the valence band to the trap is a hole emission. The net transition rate U is calculated as follows [33]:

$$U = \frac{\sigma_\mathrm{n}\,\sigma_\mathrm{p}\,v_\mathrm{th}\,N_\mathrm{t}\,(pn - n_\mathrm{i}^2)}{\sigma_\mathrm{n}\left[n + n_\mathrm{i}\exp(\frac{E_\mathrm{t}-E_\mathrm{i}}{kT})\right] + \sigma_\mathrm{p}\left[p + n_\mathrm{i}\exp(\frac{E_\mathrm{i}-E_\mathrm{t}}{kT})\right]} \tag{5.1}$$

with the following symbols

$\sigma_{\mathrm{n,p}}$	capture cross section for electrons and holes, respectively
v_th	thermal velocity

N_t	density of traps
n, p	concentration of free electrons and holes, respectively
n_i	intrinsic carrier concentration
E_t	trap energy level
E_i	intrinsic Fermi level
k	Boltzmann constant
T	absolute temperature

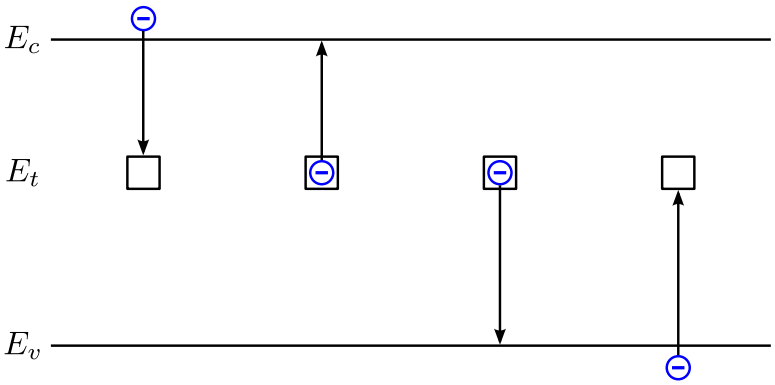

Figure 5.1: The four basic charge generation and recombination processes in a semiconductor according to the Shockley-Read-Hall Model. From left to right: electron capture, electron emission, hole capture, hole emission. In all processes a trap is involved with an energy level E_t in the band gap between the valence band E_v and the conduction band E_c.

As the PNCCD is fully depleted the concentration of free charge carriers is negligible ($n = p = 0$). Furthermore we assume that the capture cross sections for electrons and holes is equal ($\sigma_\mathrm{n} = \sigma_\mathrm{p} = \sigma$). Thus equation 5.1 can be reduced to

$$U = -\frac{\sigma\, v_\mathrm{th}\, N_\mathrm{t}\, n_\mathrm{i}}{\exp(\frac{E_\mathrm{t}-E_\mathrm{i}}{kT}) + \exp(\frac{E_\mathrm{i}-E_\mathrm{t}}{kT})} = -\frac{\sigma\, v_\mathrm{th}\, N_\mathrm{t}\, n_\mathrm{i}}{2\, \cosh(\frac{E_\mathrm{t}-E_\mathrm{i}}{kT})} \tag{5.2}$$

It is obvious that traps with an energy level close to the intrinsic Fermi level are more efficient. The negative sign in Eq. 5.2 implies a net generation rate.

The thermal velocity is proportional to the square root of the temperature T:

$$v_\mathrm{th}(T) \propto T^{\frac{1}{2}} \tag{5.3}$$

and the intrinsic carrier concentration as a function of the temperature is:

$$n_{\mathrm{i}}(T) \propto T^{\frac{3}{2}} \exp\left(-\frac{E_{\mathrm{g}}}{2kT}\right) \tag{5.4}$$

with the band gap E_{g}.

The capture cross section σ is furthermore assumed to be independent of the temperature. This leads to the following model prediction for the temperature dependence of the charge generation rate $U(T)$:

$$U(T) \propto \frac{T^2}{\exp(\frac{E_{\mathrm{g}}}{2kT})\ \cosh(\frac{const.}{T})} \tag{5.5}$$

5.1.2 Comparison of Model and Measurement Results

All eROSITA CCDs with noisy and bright pixels were measured not only at a temperature of -70 °C, but also at two higher temperatures, namely -48 °C and -31 °C. Thus the amount of charge generated by the noisy or bright pixel as a functions of the temperature can be compared to the above prediction of the Shockley-Read-Hall model. Therefor equation 5.5 is used as a fit function to the data points. As an alternative, a simple exponential fit is investigated:

$$U(T) \propto \exp(-\frac{const.}{T}) \tag{5.6}$$

Fig. 5.2 shows a sample of measured noisy pixels with both an SRH fit (red curve) and a simple exponential fit (green curve). Thereby the data of each sample was fitted individually. It is evident that the temperature behaviour of these pixels is described more accurately by the simple exponential fit.

A possible explanation for this observation is that the noisy or bright pixels are not caused by a single trap, but by a conglomeration of traps. Thus different trap energy levels are available and in total the sum of the charge created by all traps is observed.

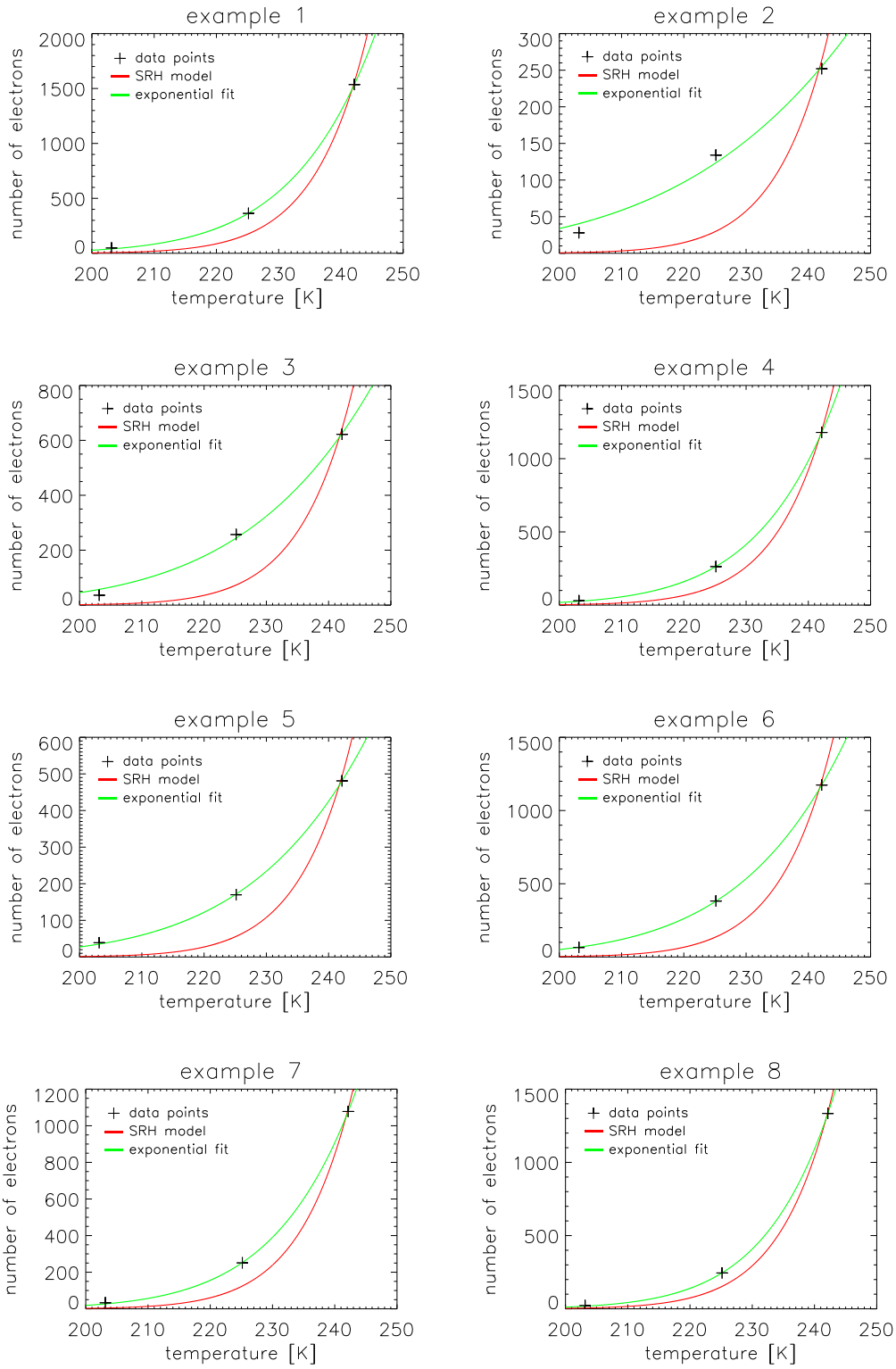

Figure 5.2: The amount of charge generated by a bright pixel plotted against the temperature. Several examples of bright pixels are compared to two different fit functions. The fit parameters were optimised for each example individually. The red curve displays the best fit according to the Shockley-Read-Hall Model. The green curve is a simple exponential fit.

5.2 Variation of the Back Contact Voltage

As mentioned earlier, during an implantation a wafer holder touched the wafer at three points on the back side. Thereby the crystal structure close to the surface was damaged causing charge generation centres. Two points where the wafer holder touched the surface are located at the chip positions 42 and 43 close to the border between the IM and FS area. The generation centres at these points were already shown in Fig. 4.11 of the previous chapter. Fortunately, the third point lies between the active areas of the chip position 32 and 33 causing no further defects.

As the defects are near the surface of the back side it can be expected that the back contact voltage has an influence on the amount of generated charge. A more negative voltage at the back contact increases the electric field close to the surface, thus separating the generated charge faster. This means that the time where the electron-hole pairs are still close enough together to recombine is shorter. Hence, more charge generated by the defect should reach the potential minimum of the pixel near the front side. In contrast, the amount of charge generated by bulk defects should be independent of the back contact voltage. There the electric field is so high that the generated electron-hole pairs are always separated immediately.

To investigate this assumption some eROSITA CCDs showing both the implanter defect and another charge generating defect were measured at different back contact voltages. Beside the usual back contact voltage of -200 V also measurements with -160 V and -240 V were performed. If necessary, the gain of these measurements was adjusted to avoid pixels reaching the ADC overflow so that it remained possible to determine the amount of charge generated by the defects from the measurement data.

In Fig. 5.3 the measured amount of generated charge is plotted against the back contact voltage. As the total amount of generated charge is quite different for each defect the relative amount is used - related to the amount generated at a back contact voltage of -200 V. The data is taken from four PNCCDs of three different wafers with an implanter damage. In all four cases the amount of generated charge increases almost linearly with the back contact voltage getting more negative. This confirms the assumption that a higher electric field separates the generated charge faster. The slope is different for the analysed defects. It varies from a change of about 0.75 % per volt to 1.35 % per volt.

Each of the four PNCCDs depicted in Fig. 5.3 has another generation centre - in the following called 'normal' - either a single pixel or a cluster of pixels being bright or very bright, which is not correlated to the implanter defect. Their behaviour with

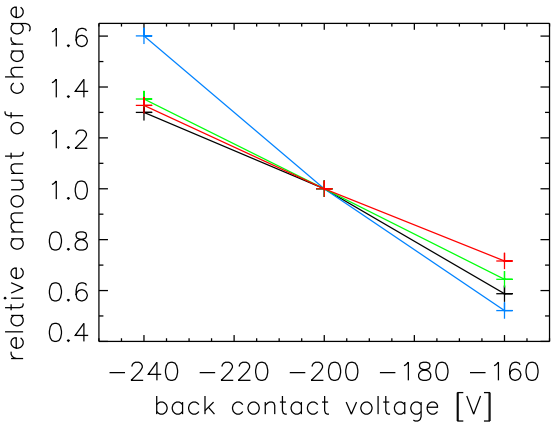

Figure 5.3: The amount of charge generated by an implanter defect versus the back contact voltage. The amount of charge is given relative to the one measured at -200 V. Each colour depicts a different PNCCD.

respect to the back contact voltage is plotted in Fig. 5.4. In contrast to the generation centres caused by the wafer holder the back contact voltage has no great impact on these defects. The variation over the whole voltage range is less than 10%. Also the slope is different. The charge generation rather slightly increases from -240 V to -160 V, opposite as with the defects caused by the implanter. This indicates that the 'normal' defects are not located close to the back side but more likely somewhere in the bulk. There the electric field is always high enough to separated the generated electron-hole pairs immediately.

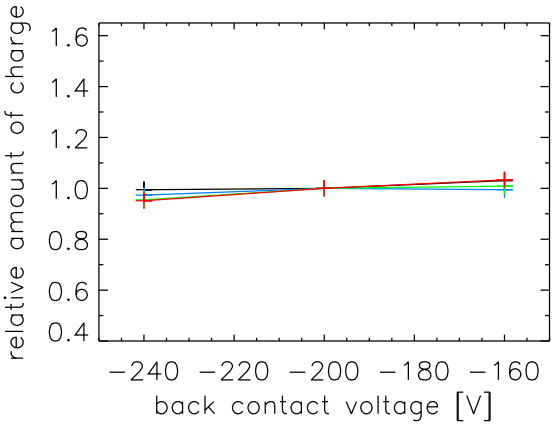

Figure 5.4: Relative amount of charge (with respect to the charge measured at -200 V) generated by a 'normal' defect as a function of the back contact voltage. In this case 'normal' defect means not caused by the wafer holder of the implanter. The colours represent the same PNCCDs as in the figure before.

Both cases of the defect location (either close to the back side surface or within the bulk) have a different dependence on the back contact voltage. They can be easily distinguished by measuring the charge generation rate as a function of the back contact voltage. This method could thus be used in the future to roughly determine the location of charge generating defects.

6 Non-Transferring Pixels

The measurement results described in chapter 4 show that about 35% of the PNCCDs have at least one pixel where the charge is not transferred correctly. These pixels are called non-transferring. As the charge is transferred by changing the potential in a certain pattern the faulty transfer is probably caused by a deformation of the potential. Thus potential simulations can help to identify defects which can lead to an incorrect charge transfer. The simulations done within this work are described in the following chapter along with experimental results.

6.1 Experimental Results

As explained in section 4.1.5 a non-transferring pixel is defined as follows: no valid split pattern can be observed in the channel behind this pixel except out of time (OOT) events. This means that in the intensity map of all valid split patterns a dark line can be seen. An example is shown in Fig. 6.1 with a non-transferring pixel in channel 326 in row 493. The few events still found after this pixel are OOT events.

There are two different types of non-transferring pixels, the dead pixels and the bad-transferring ones. The dead pixels do not transfer any charge at all. This means that also no thermally generated charge carriers - causing part of the noise - are transferred to the anode which leads to a lower noise of all pixels behind the dead ones. In a noise map at higher temperatures, e.g. at -30°C, this can be easily seen as shown in Fig. 6.2. At low temperatures it is not clearly visible as the noise contribution of the leakage current is negligible.

The second type of non-transferring pixels are the bad-transferring ones. These pixels transfer only part of the charge cloud so that the charge of one event is distributed over several pixels. Depending on the strength of the defect, the event is smeared over three up to more than 30 pixels. An example for such an event is given in Fig. 6.3.

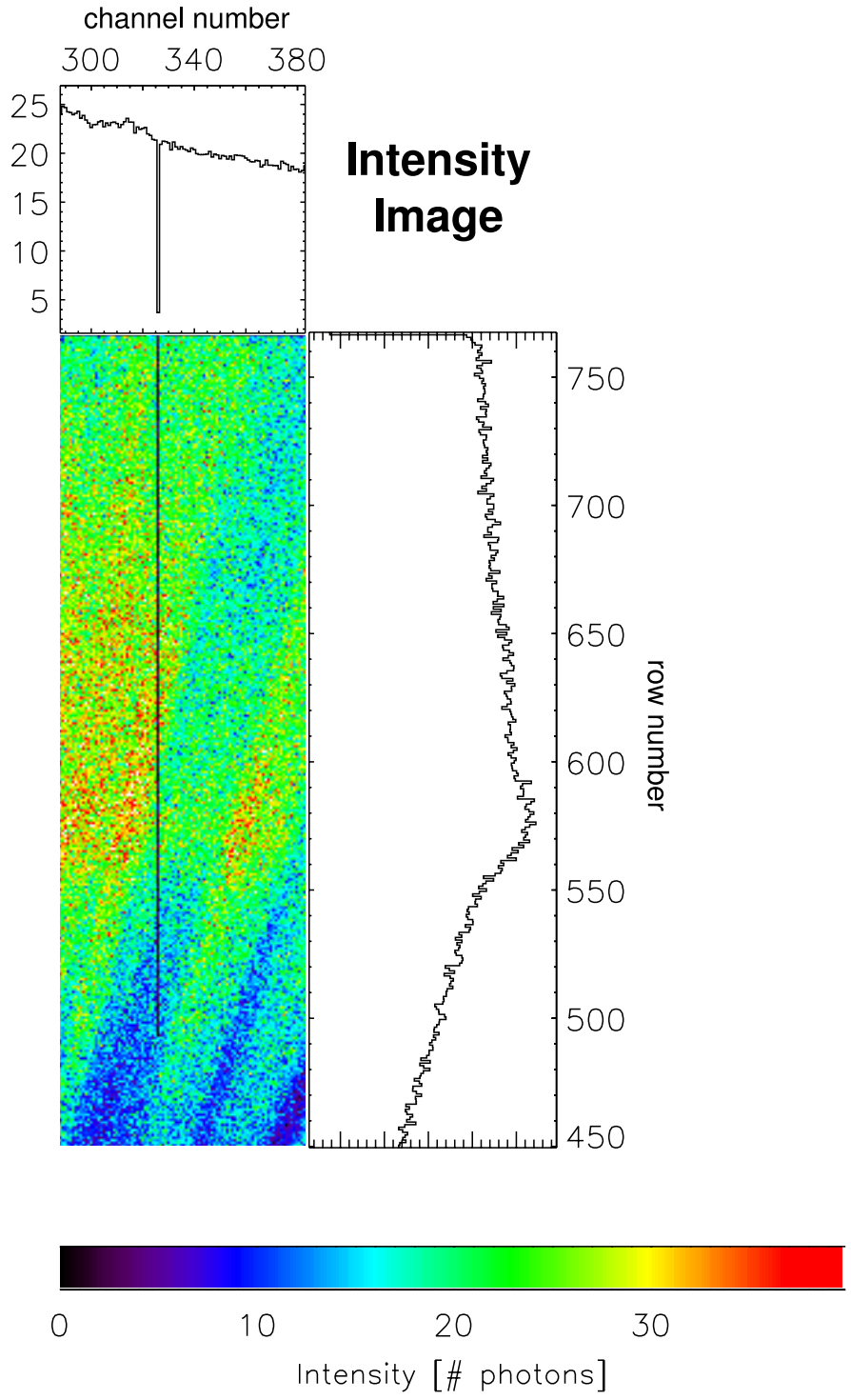

Figure 6.1: A detail of an intensity map with a non-transferring pixel in channel 326 in row 493. The part of the channel behind the non-transferring pixel is visible as a dark line as it has no events except OOT events.

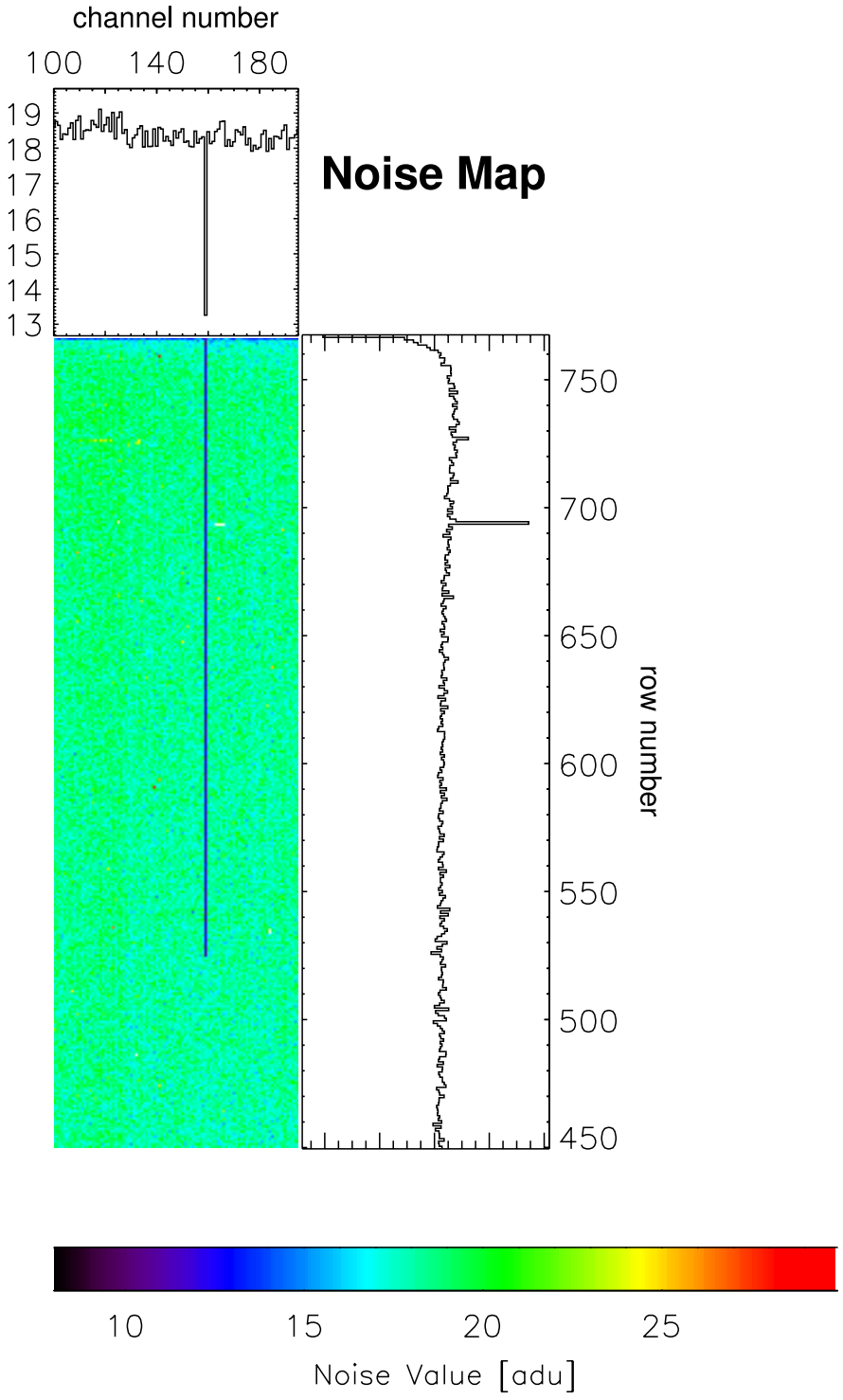

Figure 6.2: This part of a noise map measured at a temperature of -30 °C shows a dead pixel in channel 159 in row 524. No charge - not even thermally generated charge - is transferred and thus the noise is lower after the dead pixel.

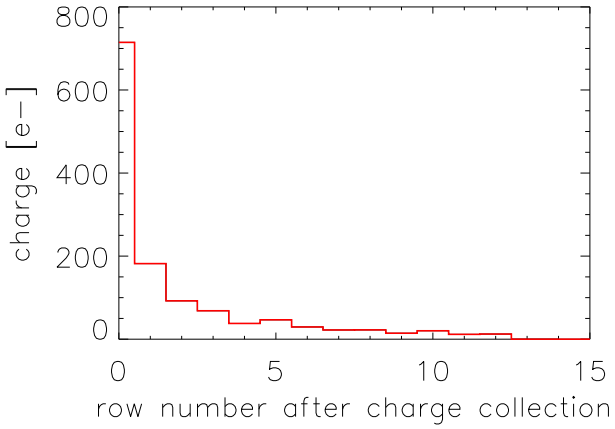

Figure 6.3: This plot shows an example event which hit the CCD after a badly transferring pixel. The charge is transferred only partially and thus it is smeared, in this case over 12 pixels.

6.2 Basics on Simulations with TeSCA

In this work, different possible causes for dead or bad-transferring pixels were investigated with 2D simulations of the charge transfer in the CCD. For this purpose, the program TeSCA (Two-Dimensional Semi-Conductor Analysis Package) was used which was developed at WIAS[1] for numerical simulations of semiconductor devices [50]. With its help the electric potential and the charge carrier densities in a semiconductor device at a certain time can be calculated. The basic concepts of such simulations are described in the next section. After this introduction, more details on the simulations done in this work are given. Finally, the simulation results are explained and compared with the measurement results.

6.2.1 Basics on TeSCA

To model a semiconductor device one has to solve the basic equations described by van Roosbroeck in 1950 [51]. These are the Poisson equation and the continuity equation for electrons and holes.

$$-\mathrm{div}(\mathrm{grad}\,\phi) = \frac{e}{\varepsilon}\,(N_\mathrm{D} - N_\mathrm{A} + N_\mathrm{p} - N_\mathrm{n})$$

[1] Weierstrass-Institut für Angewandte Analysis und Stochastik

$$e\,\frac{\partial N_\mathrm{n}}{\partial t} - \operatorname{div} J_\mathrm{n} = e\,(G_\mathrm{n} - R_\mathrm{n})$$
$$e\,\frac{\partial N_\mathrm{p}}{\partial t} + \operatorname{div} J_\mathrm{p} = e\,(G_\mathrm{p} - R_\mathrm{p})$$

with the following parameters:

ϕ	electrostatic potential
e	elementary charge
ε	absolute permittivity of silicon
N_D	donator concentration
N_A	acceptor concentration
$N_\mathrm{n,p}$	electron and hole density, respectively
$J_\mathrm{n,p}$	electron and hole current density, respectively
$G_\mathrm{n,p}$	electron and hole generation rate, respectively
$R_\mathrm{n,p}$	electron and hole recombination rate, respectively

Thereby the current density of electrons and holes, respectively, is calculated as follows [50]:

$$J_\mathrm{n} = -e\,N_\mathrm{n}\,\mu_\mathrm{n}\,\operatorname{grad}(\phi - \tfrac{kT}{e}\log\tfrac{N_\mathrm{n}}{N_\mathrm{ie}})$$
$$J_\mathrm{p} = -e\,N_\mathrm{p}\,\mu_\mathrm{p}\,\operatorname{grad}(\phi + \tfrac{kT}{e}\log\tfrac{N_\mathrm{p}}{N_\mathrm{ie}})$$

with the following parameters:

$\mu_\mathrm{n,p}$	electron and hole mobility, respectively
T	temperature
k	Boltzmann constant
N_ie	effective intrinsic carrier concentration

TeSCA solves these basic equations using the finite element method on a two dimensional grid. The potential, the electron and hole density are determined for each grid point at a certain time. The grid consists of triangles with varying grid point density. Regions with a higher potential gradient have a higher density of grid points to obtain a better resolution. To simulate a time-dependent process like the charge transfer in a CCD, the basic equations have to be solved for different time steps. Additionally the continuity equation for the total current is needed [50]:

$$\operatorname{div} J = 0$$

with $J = J_\mathrm{n} + J_\mathrm{p} - \varepsilon\,\operatorname{grad}(\frac{\partial\phi}{\partial t})$.

6.2.2 Simulated Region

The simulations described here are done for a cut along the transfer channel through the middle of the channel, i.e. through the channel notch. An area of three pixels is simulated which allows to investigate the charge transfer by two pixels. In Fig. 6.4, a sketch of the simulated region can be seen. Each of the pixels consists of three shift registers - called Φ_1, Φ_2, and Φ_3. To distinguish the three pixels they are named - from left to right - A, B, and C. The charge cloud of about 1600 e^- - which corresponds to the number of electrons generated by a Mn-K_α photon - is generated in pixel C. The transfer direction is from the right to the left side so that a charge cloud in pixel C can be shifted to pixel B and then to A. Each transfer by one pixel requires six different steps with the shift pulse pattern already explained in section 2.1.3.

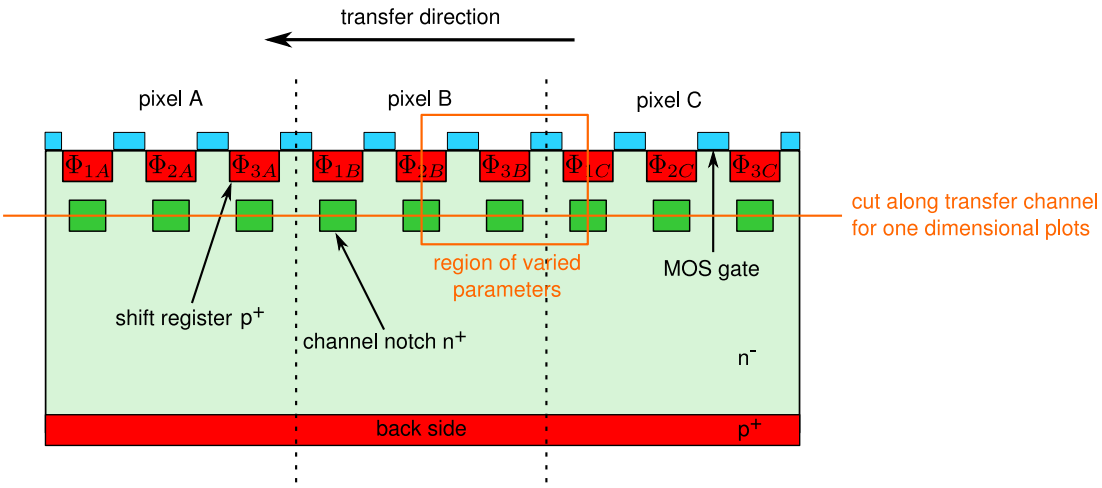

Figure 6.4: In total three pixels along one channel are simulated, i.e. nine shift registers. The pixels are denoted A, B, and C. In order to distinguish the shift registers of the different pixels, they are named accordingly, e.g. Φ_{1A}, Φ_{3B}. The region in which parameters are varied in the simulations is marked with an orange box. Most of the one-dimensional plots show the potential or electron density along a cut through the channel notches marked by the orange line.

All necessary geometrical information is taken from the eROSITA PNCCD layout. The only difference between the real layout and the simulation is the wafer thickness which is shortened to a length of 70 µm in the simulation (instead of 450 µm). Thus the bulk region (which is less interesting for the charge transfer) is reduced and the simulations are sped up. Of course, the back contact voltage in the simulation has to be adjusted to the reduced detector thickness. The back contact voltage of -200 V - as applied in the measurements - corresponds to a voltage of -24 V in the depth of 70 µm.

The dopant profiles used for the simulations are largely based on measured data. Where no measurement data was available, the dopant profile was calculated based on the technology parameters. The boundary conditions in the simulation at the contacts are chosen identical to the applied voltages during the CCPS measurements, i.e. 0 V at the MOS gates and -21 V or -27 V at the shift registers, respectively.

All one-dimensional plots in the following show a cut along the transfer channel in the depth of the potential minimum, which is located at 7.5 µm. In the two-dimensional plots the simulation is only shown to a depth of 30 µm, so that more details in the charge transfer region around the potential minimum are visible.

6.2.3 Varied Parameters

One can think of several defects which could cause an incomplete charge transfer or prevent a transfer at all. As the charge is transferred close to the front side, it is very likely that the defect is also located close to the front side.

In principle, there are two different structures forming the potential in a pixel: the transfer registers which are p^+ implants and the channel notches which are n^+ doped. Different possible failures during the manufacturing can change one of these structures. First of all, some contamination on the wafer during the implantation could lead to a wrong doping concentration either in the p^+ of the transfer register or in the n^+ of the channel notch. Secondly - similar to the first problem - an imperfection in the lithography before the implantation can lead to a smaller structure width.

In this work the following cases are investigated:

- change of the doping concentration of the n^+ implantation of the channel notch under transfer register Φ_{3B}
- change of the width of the n^+ implantation of the channel notch of Φ_{3B}
- change of the doping concentration of the p^+ implantation of Φ_{3B}
- change of the width of the p^+ implantation of Φ_{3B}

The simulation results for all these cases are described in the following section.

6.3 Simulation Results

6.3.1 Ideal Charge Transfer

Before the changes in the potential due to the imperfections are discussed, the simulation result of the ideal case of the charge transfer shall be described. In Fig. 6.5 the potential of all six voltage steps needed to transfer the charge by one pixel is shown. During the integration time, the transfer registers 1 and 2 have the more positive voltage of -21 V while the register 3 has the more negative one of -27 V. The potential minimum is thus located between the transfer register 1 and 2. Due to the MOS gate which has a voltage of 0 V between these two shift registers, the potential has a small dip and thus a quite narrow minimum underneath the MOS gate.

After the integration time the transfer of the charge is started. To shift the charge to the next pixel six steps are needed in total. In the first step the voltage of register 2 is changed to the more negative one so that the potential minimum moves below the register 1. In the second step the voltage of register 3 is changed to -21 V. Thus the minimum is again located between two registers like in the beginning, but now these are number 3 and 1. The minimum after this step is at the pixel border between pixel B and C which is at $x = 150\mu$m.

In the next step, the potential of register 1 is changed to -27 V which leads again to a charge storage under one register, namely register 3. By changing the register 2 to -21 V (step 4), the potential minimum moves on to a location between register 2 and 3. Step 5 shifts the minimum to be under register 2 by changing the voltage of register 3 to the more negative one. The last step of the transfer changes the voltage of register 1 to the more positive one so that the potential minimum is again located beneath register 1 and 2 as it was in the beginning.

Fig. 6.6 shows the simulated electron density of the charge cloud during all the transfer steps described above. The charge cloud follows the potential minimum as can be seen easily if one compares the position of the charge and the potential minimum in Fig. 6.6 and Fig. 6.5, respectively. In each step where the charge is stored below one register the charge distributes over a larger area as the potential minimum is broader. If stored below two registers the distribution is smaller as the minimum is more narrow due to the mentioned dip caused by the positive MOS gate between the two shift registers.

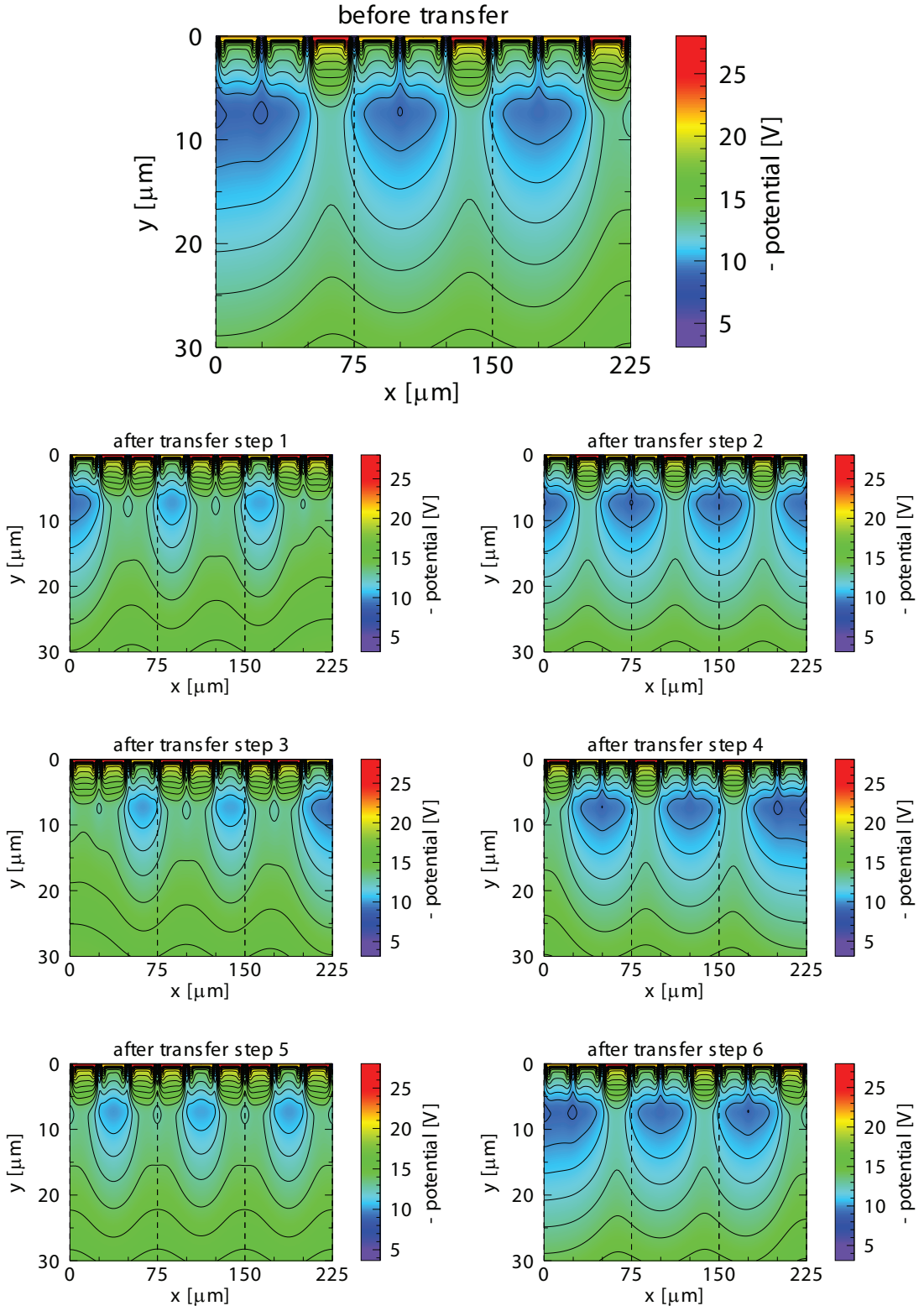

Figure 6.5: Simulation of the ideal potential of all steps needed to transfer the charge by one pixel. The simulated region is only plotted to a depth of 30 µm to show more details in the charge transfer region. The dark blue parts in a depth of about 7.5 µm are the potential minima where the charge is stored.

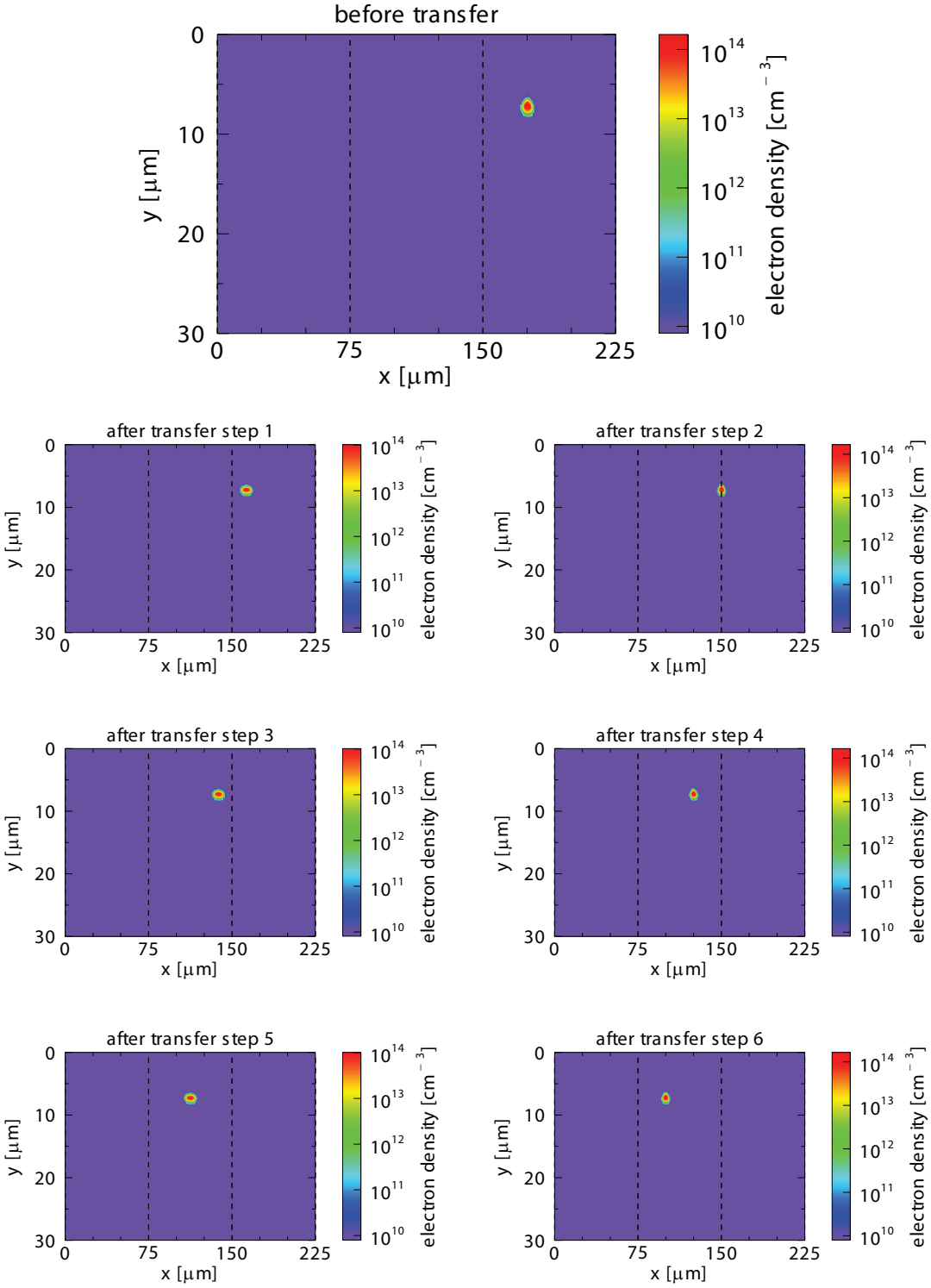

Figure 6.6: Simulation of the electron density during an ideal charge transfer. All steps needed to transfer the charge by one pixel are shown. The charge is collected in pixel C and transferred to pixel B (transfer direction from the right to the left).

6.3.2 Doping Concentration of the Channel Notch

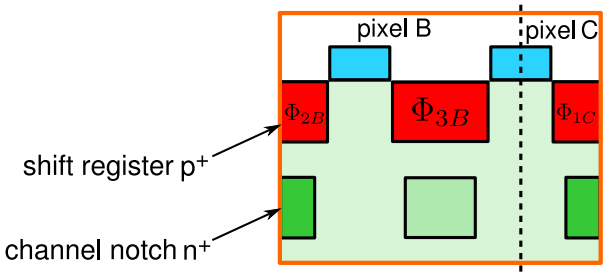

Figure 6.7: A detail of the simulated region. The lower doping concentration of the channel notch below Φ_{3B} is indicated by the paler colour than before (see Fig. 6.4).

The first possible imperfection which was simulated was the change of the doping concentration of the n^+ implantation of the channel notch. As illustrated in Fig. 6.7 the channel notch implantation below the shift register 3B was modified. Therefor the entire doping profile of the channel notch was scaled with respect to the default value. The scaling factors were chosen between 0.4 and 0.9. In Fig. 6.8 the resulting potential during the integration is shown with a doping concentration of 60 % of the default value. The potential barrier between the two potential minima for electrons is higher than usual by about 1.5 V (more clearly visible in the first picture of Fig. 6.9). This is evident as a lower doping concentration of the n^+ implantation implies a smaller amount of positive space charges left in this region when depleted. Thus the potential becomes more negative which means a higher barrier for electrons. If the doping concentration is reduced further, the barrier increases even further.

Fig. 6.9 shows the potential for different scaling factors of the channel notch doping concentration and how it changes during a whole transfer. One can see that in step 3 and 4, in case of a scaling factor of 0.6 or less, the potential minimum in pixel B is divided by a bump which increases with lower doping concentration. A look at the charge distribution illustrated in Fig. 6.10 shows the consequences of this potential bump. It prevents part of or the whole charge to be shifted to the next pixel. At a scaling factor of 0.4, no charge is transferred anymore. On the other hand, a doping concentration of 70 % of the default value still allows the charge to be transferred completely.

In Fig. 6.11 the number of electrons being transferred to the next pixel (i.e. from pixel C to pixel B) as a function of the scaling factor is shown. If the doping concen-

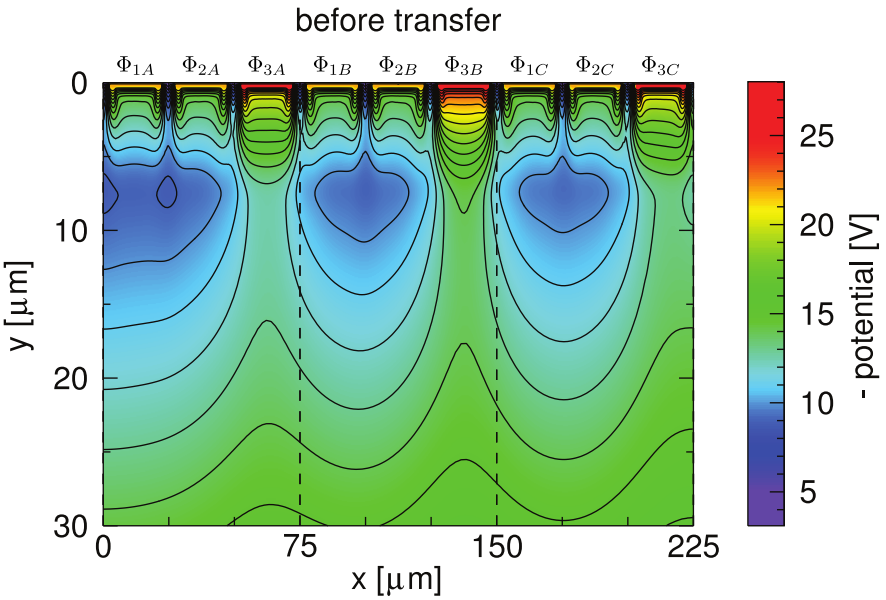

Figure 6.8: The potential of the simulated region with a doping concentration in the channel notch below Φ_{3B} of 60 % of the default value. The negative potential of the shift register Φ_{3B} is less compensated by the positive space charge of the channel notch implantation and thus the barrier between pixel B and C gets higher.

tration is lower than 45% of the default value, the charge is not transferred anymore and thus the pixel seems to be a dead one. In the range between 0.45 and 0.65 the charge is only transferred partly leading to a badly transferring pixel. For doping concentrations of 65% or more of the default the total amount of charge is transferred and no defect is seen at all.

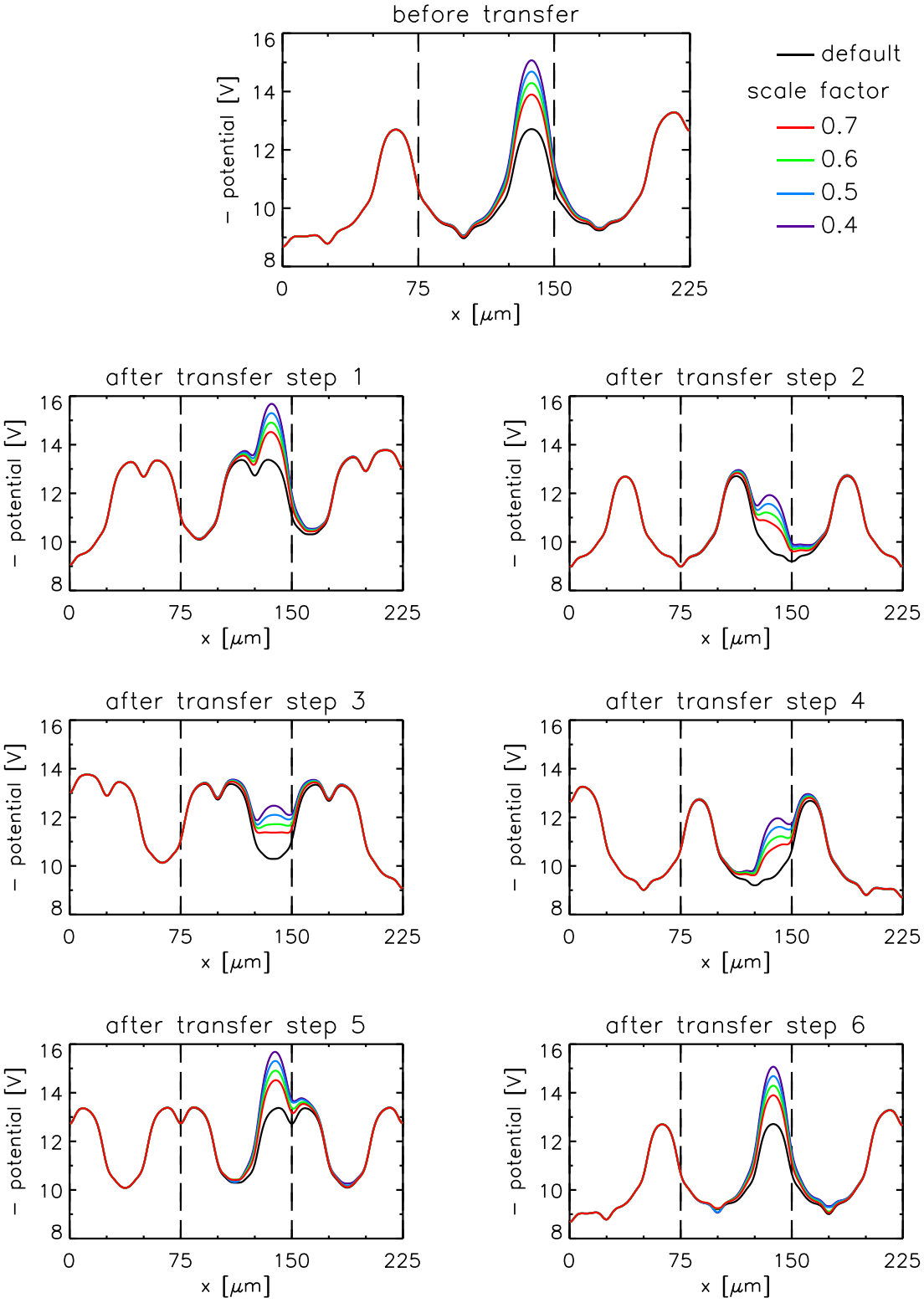

Figure 6.9: The potential on a cut along the transfer channel at a depth of 7.5 µm (i.e. through the potential minima) is shown in these plots for each transfer step. The doping concentration of the channel notch was reduced by the scale factor given in the legend next to the first plot. After transfer step 3, for a doping concentration of less than 60% of the default value the bump dividing the charge cloud can be seen.

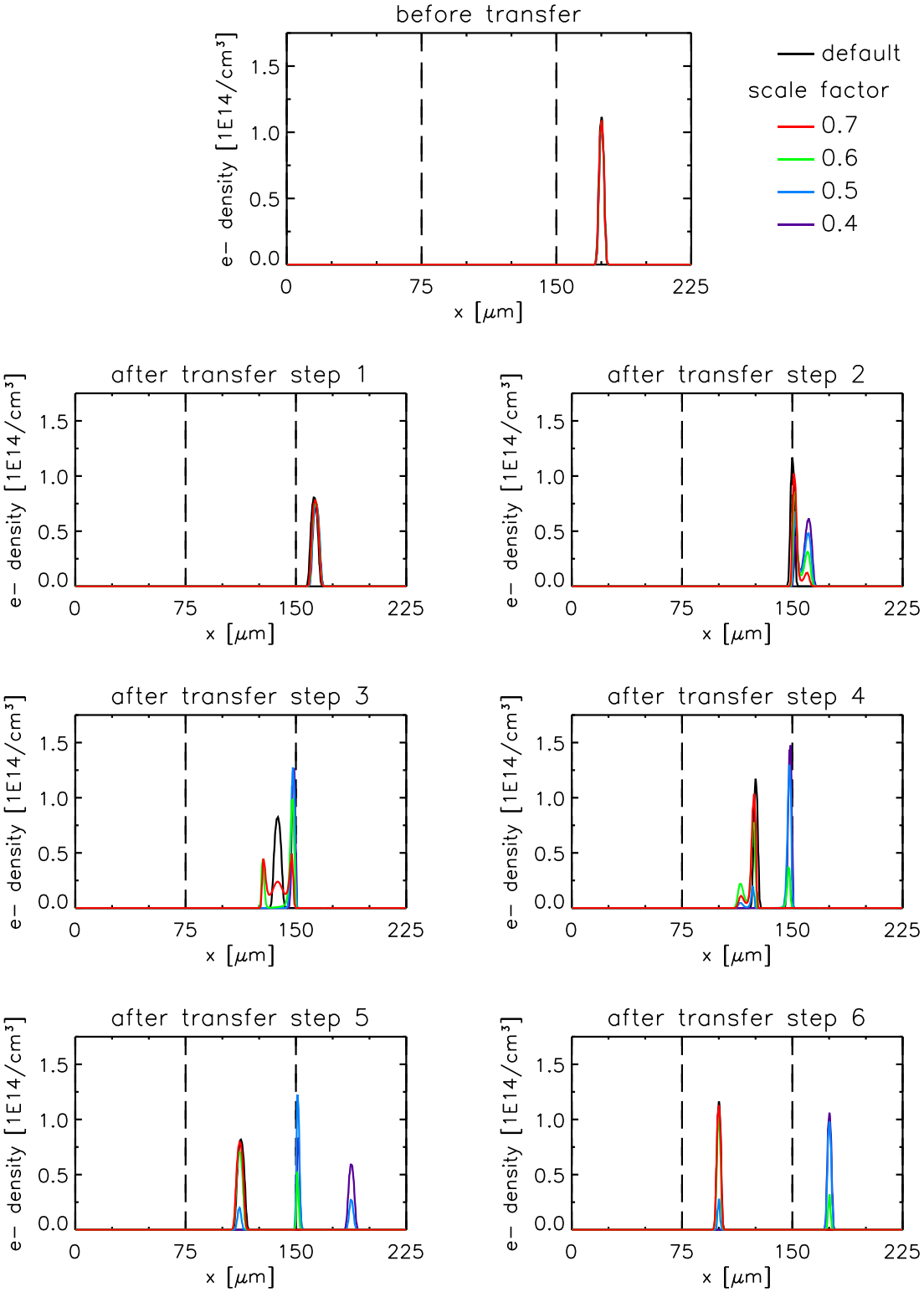

Figure 6.10: In these plots the electron density matched to the potential in Fig. 6.9 is shown. The charge is generated in pixel C, i.e. it is collected at $x = 175\,\mu m$ in the first figure. The doping concentration of the channel notch was reduced by the scale factor given in the legend next to the first plot. After transfer step 4 the charge is split into two parts.

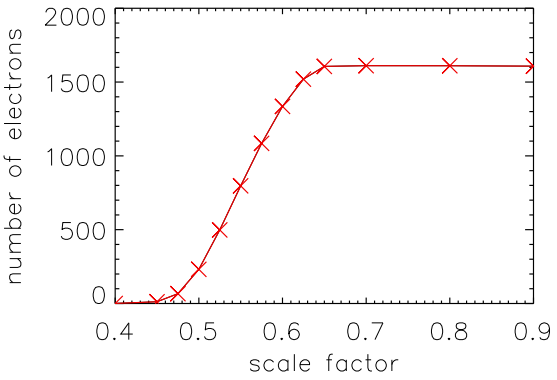

Figure 6.11: The number of transferred electrons (after one transfer) plotted against the scale factor of the channel notch doping concentration. For scale factors between 0.65 and 0.9 the total amount of charge is shifted to the next pixel, where as below a scale factor of 0.45 no charge is transferred anymore. Between 0.45 and 0.65 only a part of the charge is moved to pixel B.

6.3.3 Width of the Channel Notch

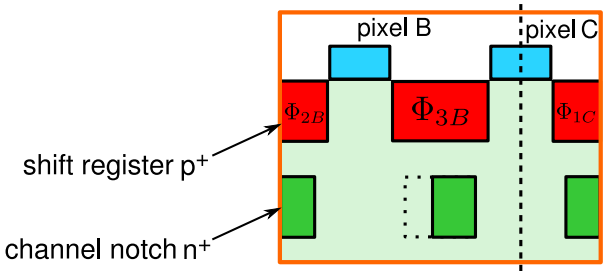

Figure 6.12: A sketch of the reduced width of the channel notch implantation. The original width is indicated by the dotted line.

Another possible fault could be the reduction of the width of the channel notch implantation. To investigate its influence on the charge transfer process the channel notch below Φ_{3B} was shortened from the side next to Φ_{2B} (see Fig. 6.12) by an amount between 1 and 4 µm. The potential in the 2D plot in Fig. 6.13 shows the case of a reduction by 3 µm. Again the potential barrier between the two potential minima is increased, but in contrast to the scaling of the doping concentration it also becomes asymmetric.

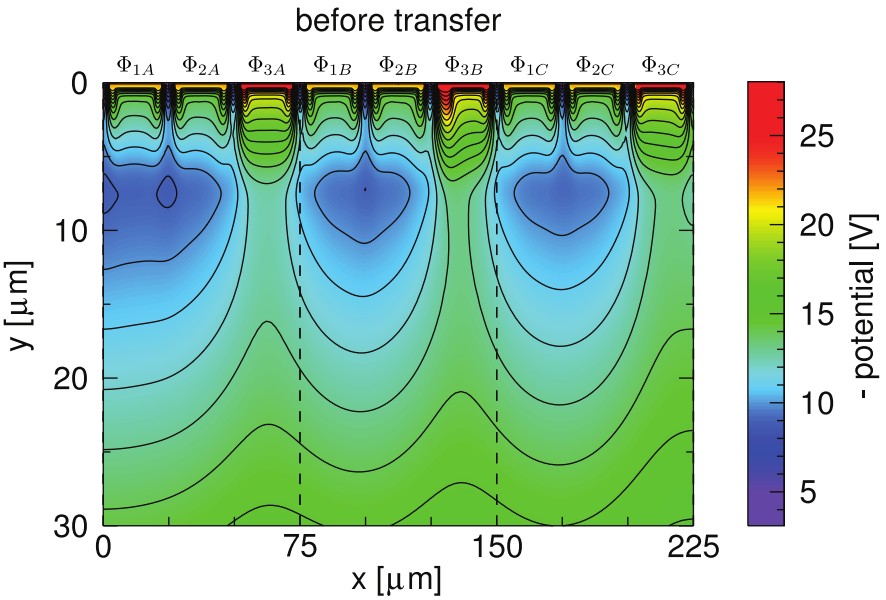

Figure 6.13: The simulated potential with a width of the channel notch reduced by 3 µm from the left side. Similar to the case before with the reduced doping concentration the potential barrier between the potential minima of pixel B and C is increased. But in contrast to the previous case the change in the potential is asymmetric.

In Fig. 6.14 and 6.15 the potential and the electron density during one transfer are shown for four different widths of the channel notch (the nominal width was reduced by 1, 2, 3, and 4 µm). In step 3 and 4 the potential minimum in pixel 3B is again divided by a bump of varying size. If the channel notch is reduced by 4 µm the bump after step 4 is about 0.2 V high and no charge is transferred any more. A reduction by 1 µm, on the other hand, has no consequences at all for the charge transfer.

The influence of the width of channel notch is illustrated in Fig. 6.16 where the number of electrons in pixel 3B after the first transfer is plotted against the reduction of the width. If the width is reduced by 3.25 µm or more no charge is transferred. For a reduction of 1.5 µm or less the charge is shifted completely. In between the amount of charge transferred to pixel B decreases with increasing reduction.

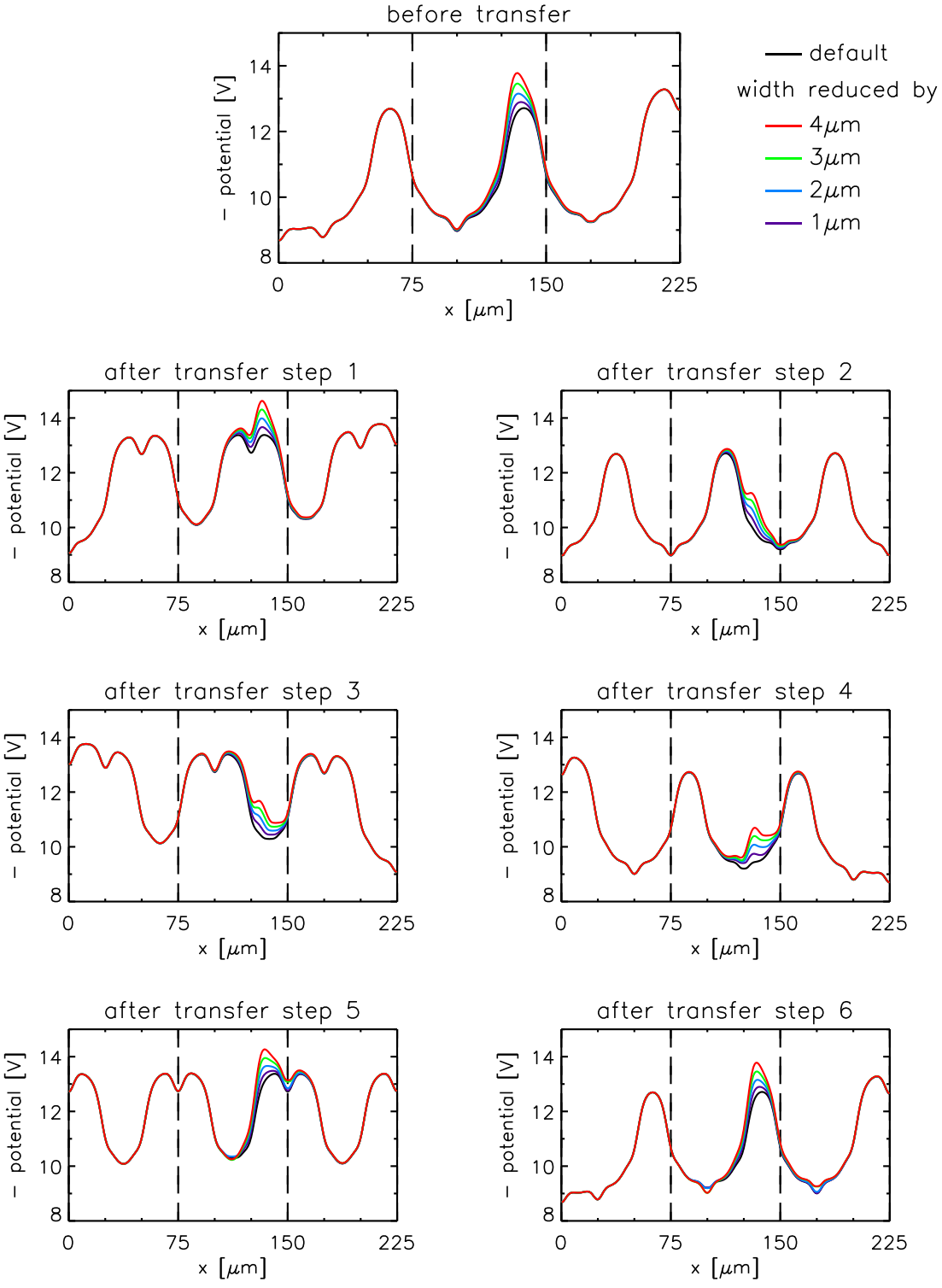

Figure 6.14: This set of plots shows the potential during a transfer for different variations of the channel notch width. The width is reduced by 1 µm to 4 µm. After step 4 the bump arising in the potential minimum in pixel B can be seen which is responsible for the incomplete charge transfer.

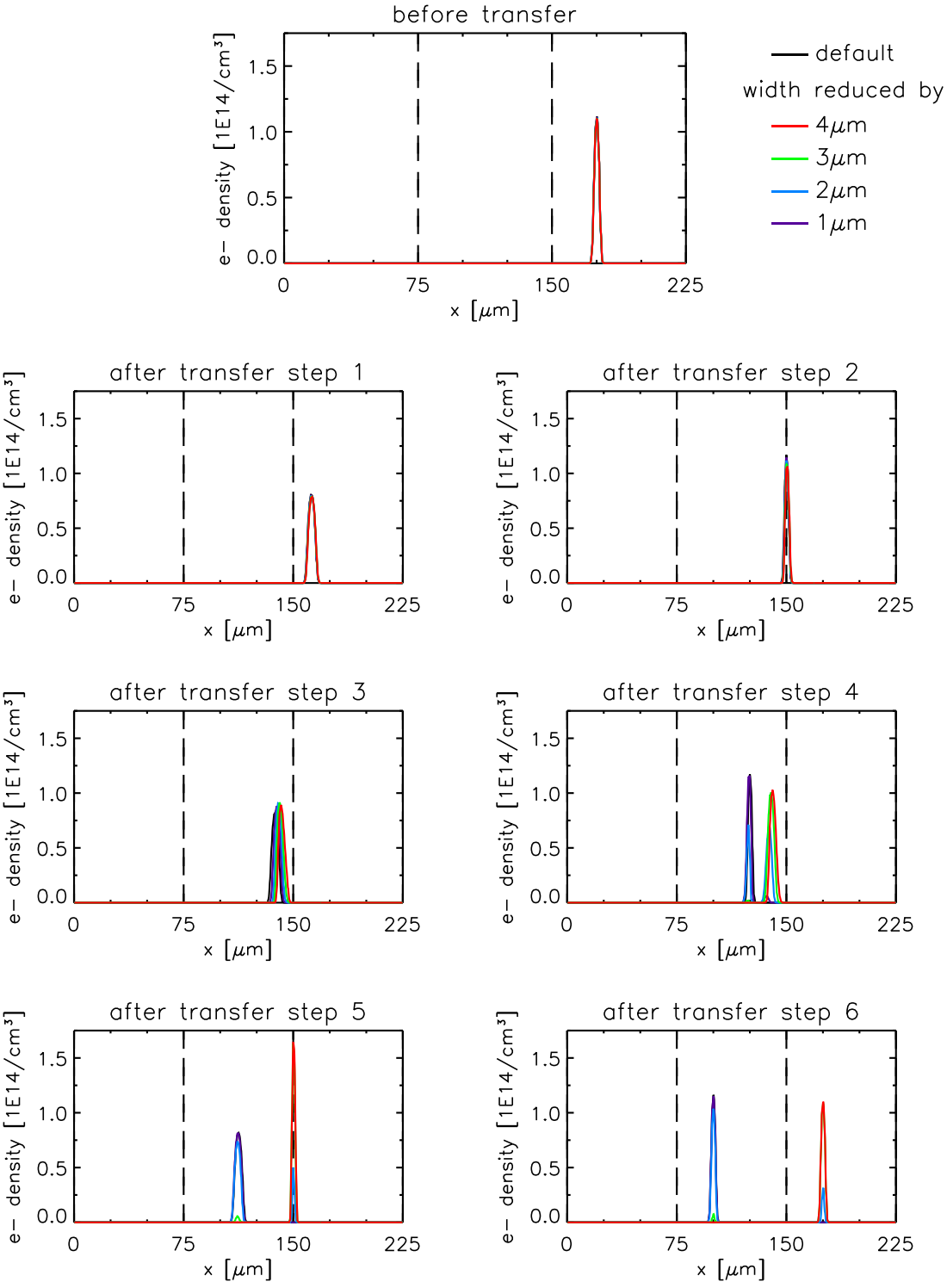

Figure 6.15: The electron density matching the potential shown in Fig. 6.14. Also all steps of a transfer are illustrated. The charge is splitted into two parts after transfer step 4 for a width reduced by 2 µm and 3 µm. For 1 µm the charge is transferred completely, whereas no charge at all is transferred for a width reduction of 4 µm.

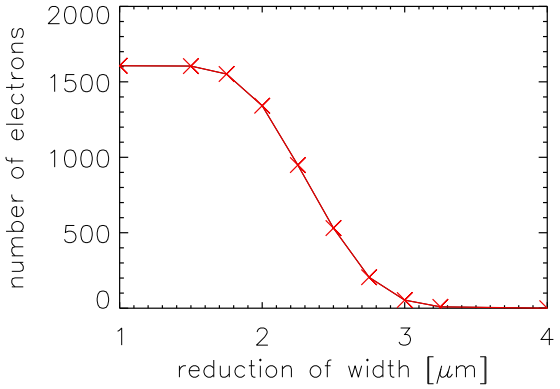

Figure 6.16: The number of electrons transferred to pixel B versus the reduction of the width of the channel notch. In the range between 1.5 µm and 3.25 µm the amount of charge transferred to pixel B slowly decreases until no charge is transferred anymore.

6.3.4 Doping Concentration of the Shift Register

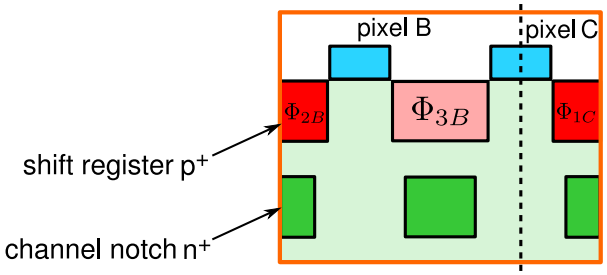

Figure 6.17: A detailed view of the simulated region showing the lower doping concentration of the shift register Φ_{3B}. The lower doping concentration is indicated by the paler colour of Φ_{3B} compared to Φ_{2B} or Φ_{1C}.

Besides the channel notch also the p^+ implant of the shift register plays an important role in the charge transfer. To investigate the influence of this implantation, at first the doping concentration of shift register Φ_{3B} (see Fig. 6.17) was scaled by a factor between 0.01 and 10. As an example, in Fig. 6.18 the potential in the simulated region for a scale factor of 0.01 is illustrated. Due to the lower doping concentration 99% of the negative space charge in the p^+ implant is missing and thus the potential barrier between pixel B and C is not as negative a intended.

This also can be seen in Fig. 6.19 showing the potential in the transfer channel before the charge transfer for the scaling factors of 10, 0.1 and 0.01 together with the

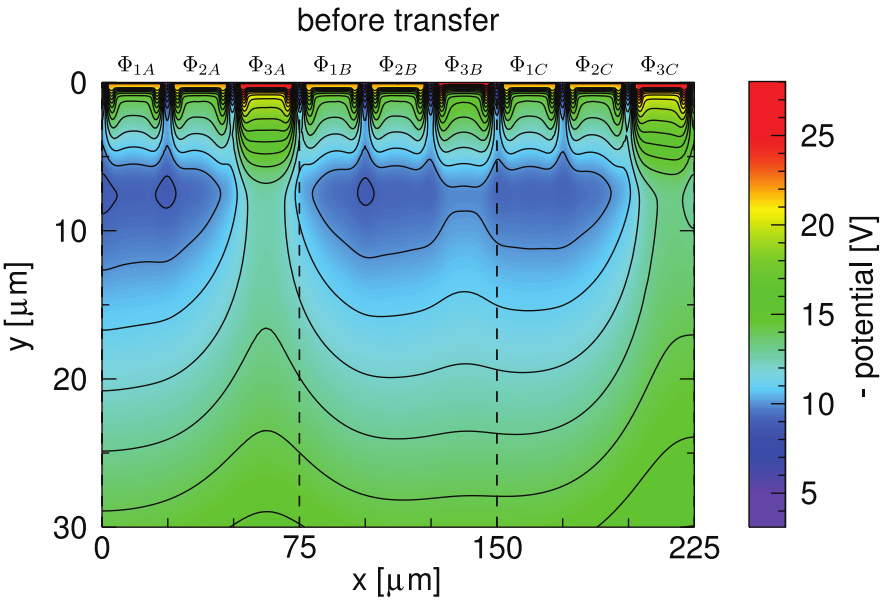

Figure 6.18: Potential in the simulated region with a changed doping concentration in the p^+ implant of the shift register Φ_{3B}. The default value of the doping concentration was scaled by a factor of 0.01. The potential barrier between pixel B and C is reduced as part of the negative space charge in the shift register implant is missing, leading to a more positive potential at the shift register and below it.

default situation. In contrast to the reduced doping concentration of the channel notch, the lower doping concentration at the shift register does not influence the transfer as much. Scaling factors in the range between 0.1 and 0.9 do not affect the charge transfer at all. Only with very low doping concentrations of 0.01 of the default, about 28 % of the total charge is left behind as shown in Fig. 6.20.

The higher doping concentrations up to a factor of ten higher than the default value do not hinder the charge transfer at all. The change of the potential is similar to a lower doping concentration of the channel notch. A factor of ten changes the potential in the transfer channel by about 1.8 V.

According to these results, it is very unlikely that a wrong doping concentration of the shift register causes the incomplete charge transfer as this implantation would have to differ largely from the default to see any influence in the charge transfer. Hence, this case is not considered any longer in the following analysis.

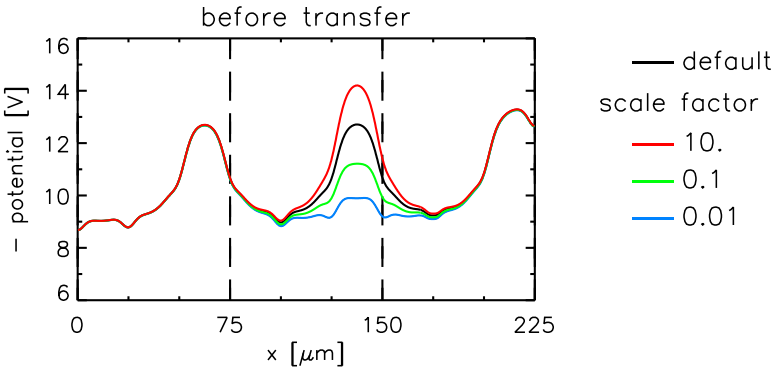

Figure 6.19: The potential in the transfer channel during the integration time. The original value (black curve) of the doping concentration of the shift register Φ_{3B} was scaled by the factor 10 (red), 0.1 (green) and 0.01 (blue).

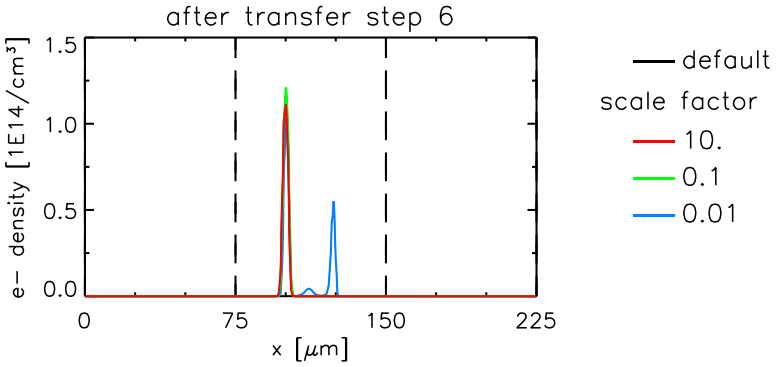

Figure 6.20: The electron density in a cut along the transfer channel after the transfer by one pixel. For the scale factors of 10 and 0.1 the charge is shifted without loss to pixel B, whereas for the scale factor 0.01 only about 72% of the charge generated by a Mn-K_α photon (which is about 1600 electrons) is transferred.

6.3.5 Width of the Shift Register

Not only the doping concentration but also the width of the p^+ implantation of the shift register could be changed during the chip production. In the simulations the width is reduced only from one side, namely the one close to Φ_{2B} (see Fig. 6.21). An example of the potential is illustrated in the 2D plot in Fig. 6.22. There the width is reduced by 3 µm.

In the simulations the width of the p^+ implantation was changed by 1 µm to 4 µm. The resulting potential along the transfer channel is shown in Fig. 6.23 and the corresponding charge density in Fig. 6.24.

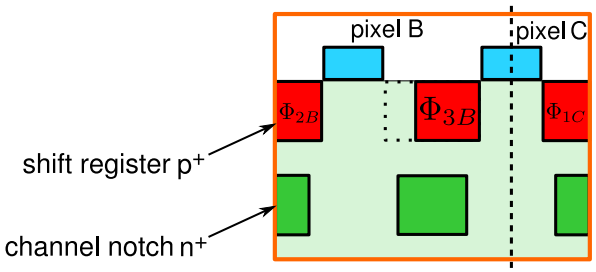

Figure 6.21: A sketch illustrating the reduction of the width of the shift register Φ_{3B}. The width is reduced from the side next to Φ_{2B}.

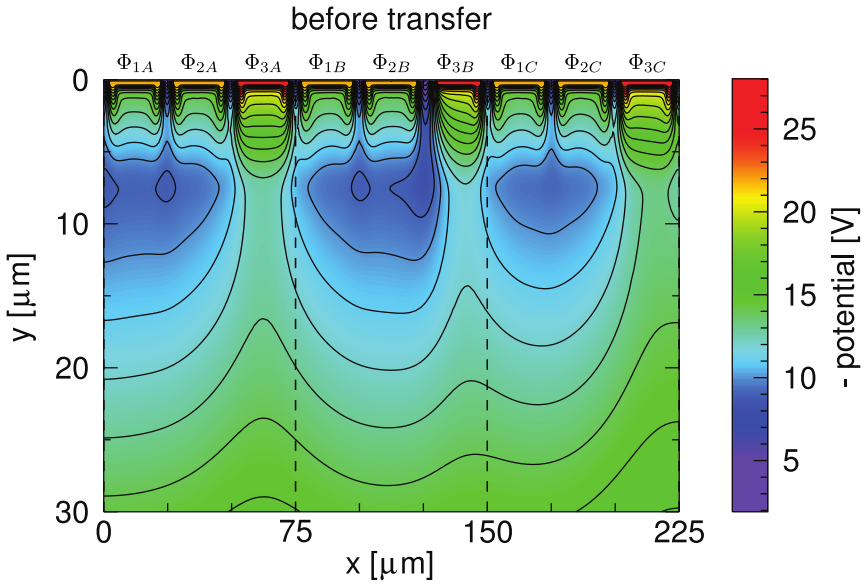

Figure 6.22: The potential in the simulated area with the shift register Φ_{3B} reduced in width by 3 µm. The potential barrier to the MOS gate between Φ_{2B} and Φ_{3B} exists no longer.

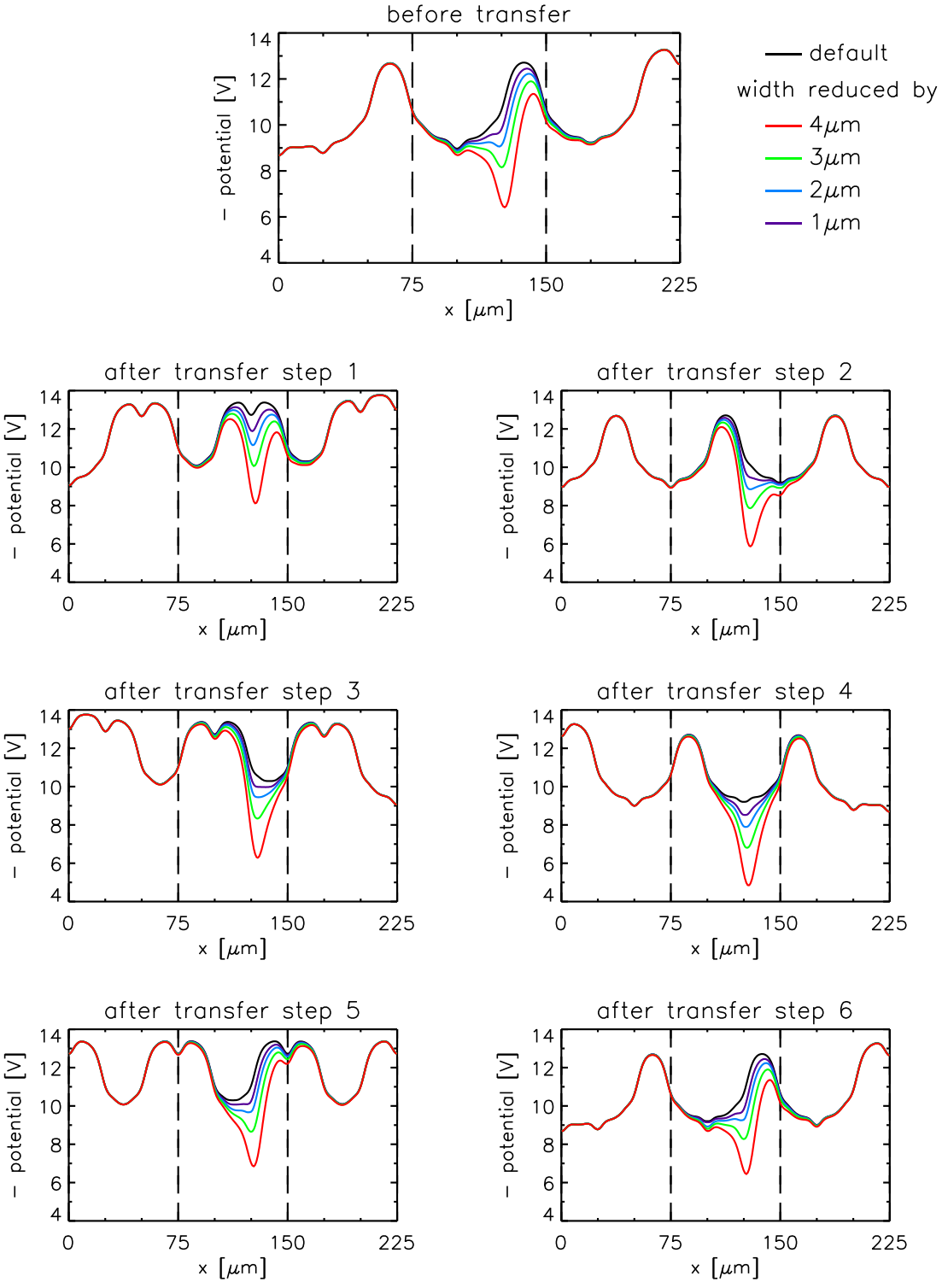

Figure 6.23: The potential in a cut along the transfer channel for all transfer steps. The width of the shift register was reduced by 1, 2, 3 or 4 µm as indicated in the legend. The dip in the potential curve at $x = 125$ µm gets deeper (i.e. the potential becomes more positive) for smaller widths of the shift register.

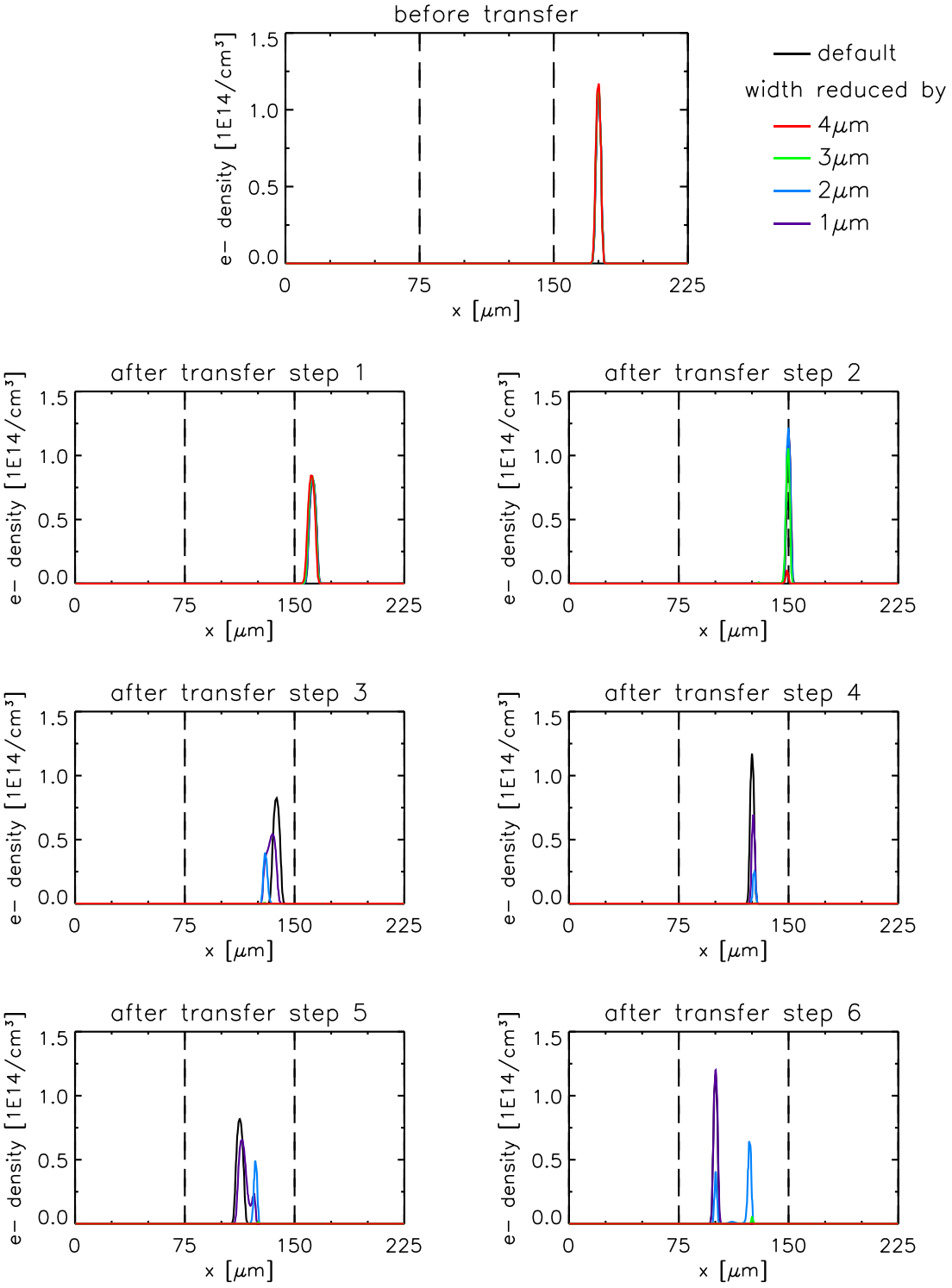

Figure 6.24: The electron density corresponding to the potential plots of Fig. 6.23 for all steps of a transfer. The charge is shifted completely as long as the width of Φ_{3B} is not reduced by more than 1 µm. With a reduction of 2 µm only part of the charge cloud is transferred to the next pixel. If the width is reduced by 3 µm or more the charge gets lost after step 3.

The smaller width of the shift register modifies the potential such that, depending on the strength of the effect, a correct charge transfer is not possible for different reasons. At first, if the shift register width is not reduced too much, the potential minimum below the MOS gate gets more positive, thus creating a permanent local potential minimum. Part of the charge cloud or the whole charge cloud can be trapped in there. This is clearly visible in Fig. 6.24 for the case of a reduction of 2 µm.

If the shift register width is reduced further, the potential barrier to the MOS gate becomes so small that part of the charge can flow to the electron layer accumulated underneath the MOS gate. Finally, for even smaller width of the p^+ implantation of the shift register, the potential barrier vanishes completely (and with it the local potential minimum). Then the whole charge cloud can flow to the electron layer accumulated underneath the MOS gate.

In Fig. 6.25 the potential structure below the MOS gate at $x \approx 127\mu$m is shown along a cut into the depth (perpendicular to the transfer direction). The simulation with a reduced shift register width of 3.25 µm (red curve) demonstrates the vanishing potential barrier to the MOS gate. For comparison, also the potential for the default structure (black curve) is plotted where the potential barrier to the MOS gate can be clearly recognised.

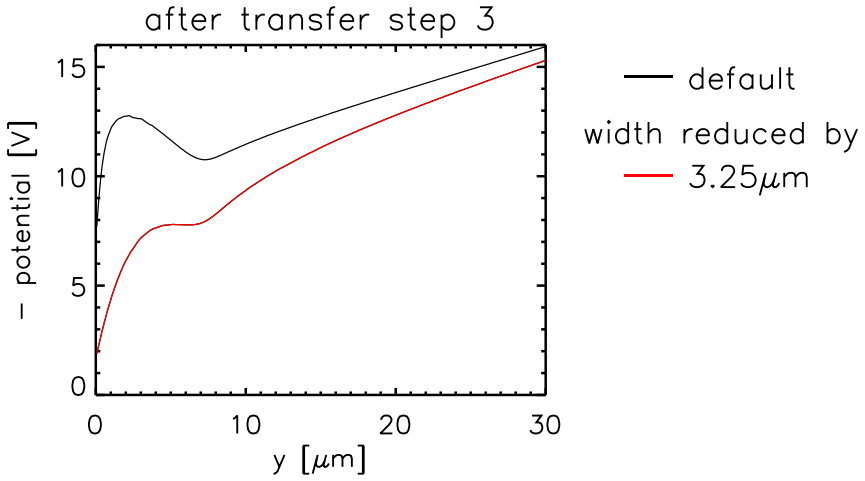

Figure 6.25: The potential structure along a cut in y-direction at $x \approx 127\mu$m. The black curve shows the default situation. The potential minimum of the transfer channel at $y = 7\mu$m is clearly visible. It prevents the charge from flowing to the electron layer underneath the MOS gate. In case the shift register width is reduced by 3.25 µm (red line), the potential minimum vanishes and the electrons can leave the transfer channel towards the MOS gate.

The amount of charge transferred to pixel B as a function of the reduction of the shift register width is illustrated in Fig. 6.26. Only for a reduction of 1 µm or less the charge transfer is not affected. In the range between 1 µm and 2.25 µm the amount of charge transferred correctly to the next pixel decreases rapidly, while the number of electrons trapped in the local potential minimum increases. If the width is reduced by 2.25 µm or more no charge is transferred correctly anymore. The number of electrons trapped does not change much in the range between 2.25 µm and 2.75 µm. For further reduction the amount of trapped charge decreases rapidly until for 3.25 µm or more the whole charge cloud flows to the electron layer underneath the MOS gate.

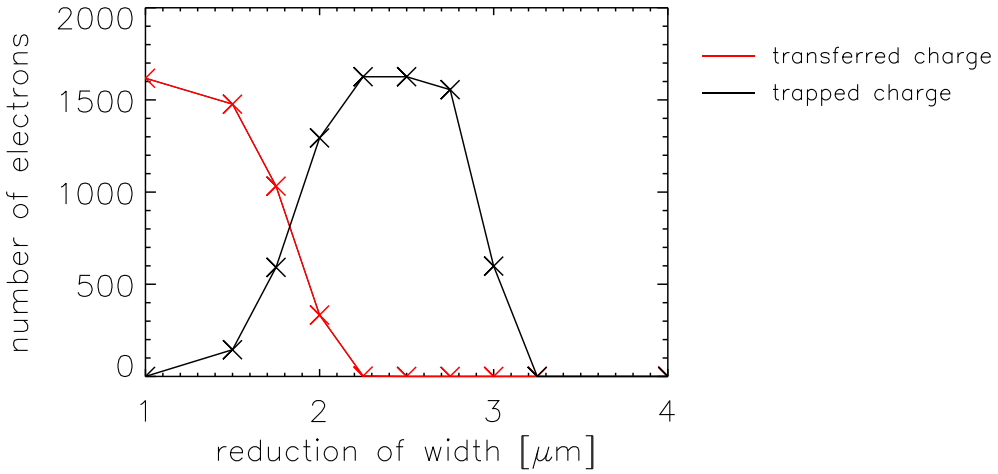

Figure 6.26: The number of electrons transferred to pixel B plotted versus the reduction of the width of the shift register Φ_{3B}. The red curve shows the charge which is correctly transferred to pixel B, whereas the black curve depicts the charge which is trapped in the local potential minimum.

6.4 Comparison with Measurement Results

6.4.1 Effect of the Shift Register Amplitude Voltage

As measurements have shown, in some cases of non-transferring pixels it is possible to correct the blocked transfer by applying a more negative shift register amplitude voltage[2]. In Fig. 6.27 an example of a PNCCD showing this behaviour is plotted. The curve depicts a badly transferring pixel of one CCD measured with four different shift register amplitude voltages, namely -6 V, -7 V, -8 V and -9 V.

[2] Of course, the possibel increase of the shift register amplitude voltage is limited in order not to damage the CCD.

At a shift register voltage of -6 V about 50% of the charge is transferred. The amount of transferred charge increases with the shift register amplitude voltage becoming more negative. Finally, for -9 V the charge is shifted completely.

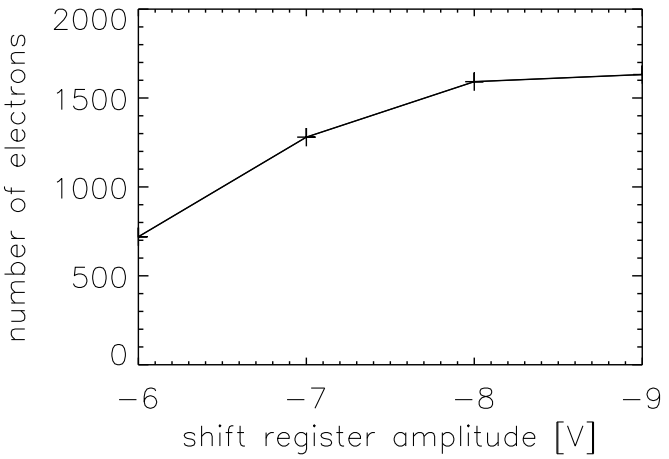

Figure 6.27: The number of electrons transferred by a badly transferring pixel was measured for four different shift register amplitude voltages. The result is shown in this plot. The more negative the shift register amplitude voltage, the more charge is transferred.

If the simulations are a correct model to describe non-transferring pixels, it should be possible - at least for some cases - to reproduce this behaviour in the simulations as well. To verify this, simulations were done with a shift register amplitude in the range from -6 V to -9 V. For each relevant defect investigated above, one example was selected where no charge transfer was possible, but where the responsible defect parameter is still close to the range with bad charge transfer. The examples were chosen as follows:

- doping concentration of the channel notch n^+ implantation by with a factor of 0.4
- width of the channel notch n^+ implantation reduced by 3.5 µm
- width of the shift register p^+ implantation reduced by 2.25 µm

The resulting number of electrons transferred from pixel C to B is illustrated in Fig. 6.28 for all three cases. If the doping concentration of the channel notch is only 40% of the default value (red curve), no charge is transferred at a shift register amplitude voltage of -6 V. At -7 V about 10% of the electrons generated by a Mn-K_α photon are transferred to the next pixel. Increasing the amplitude voltage further improves

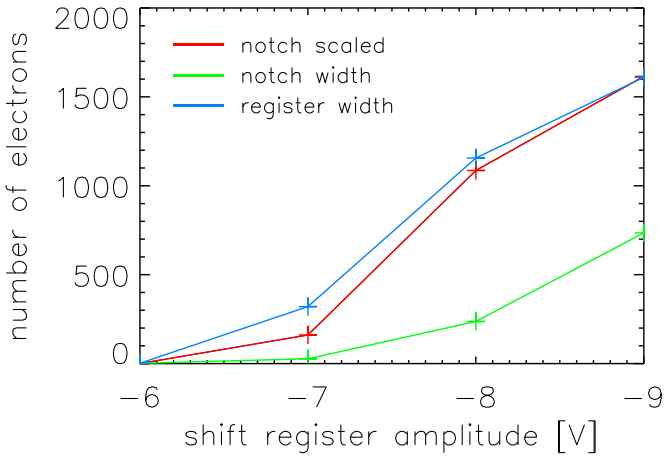

Figure 6.28: The number of shifted electrons as a function of the shift register amplitude voltage. Three different examples with no charge transfer at -6 V were simulated. The red curve shows the shifted charge if the channel notch n^+ implantation is scaled by a factor of 0.4. The green curve displays the number of electrons in pixel B if the width of the channel notch is reduced by 3.5 µm. The blue curve gives the number of shifted electrons for a shift register width reduced by 2.25 µm.

the charge transfer. Finally, with a shift register amplitude voltage of -9 V the whole charge cloud is shifted to pixel B.

A more negative amplitude voltage also improves the charge transfer if the width of the channel notch is reduced (green curve in Fig. 6.28). The channel notch was reduced by 3.5 µm where no charge is transferred at an amplitude voltage of -6 V. If the amplitude voltage at the shift register is increased to -7 V, a small number of electrons (less than 100) is shifted to the next pixel. This number increases with the shift register amplitude voltage getting more negative, but not as much as for the scaled doping concentration. At -9 V still less than half of the charge cloud is transferred.

The blue curve in Fig. 6.28 shows the case that the width of the shift register implantation is reduced by 2.25 µm. Again, with a more negative shift register amplitude voltage the charge transfer improves. Thereby the slope is similar to the example of the scaled channel notch. The whole number of electrons is shifted from pixel C to B for an amplitude voltage of -9 V.

These results prove that, in principle, the simulated cases can qualitatively describe the observed behaviour of non-transferring pixels. In the next step it shall be investigated if it is possible to distinguish between the different defects based on measurements of this behaviour. This should be possible as the influence on the charge transfer seems to be slightly different for the three kinds of defects.

For this purpose and for the measured example shown in Fig. 6.27 all three kinds

of defects were simulated again. The parameters for the simulations were chosen to match the measured amount of charge transferred at a shift register amplitude voltage of -6 V with a deviation of less than 10%:

- doping concentration of the channel notch n^+ implantation scaled by a factor of 0.54
- width of the channel notch n^+ implantation reduced by 2.4 µm
- width of the shift register p^+ implantation reduced by 1.83 µm

The voltage range covered by the simulations was again from -6 V to -9 V. The results of the simulations together with the ones of the measurements are shown in Fig. 6.29. As before, the amount of transferred charge increases faster for the scaled doping concentration (red curve) and for the reduced shift register width (blue curve) than for the reduced width of the channel notch (green plot). Only the latter behaviour matches the measurement results (black line) perfectly. This indicates that the non-transferring pixel in our example is caused by the width of the channel notch n^+ implantation being reduced by about 2.4 µm.

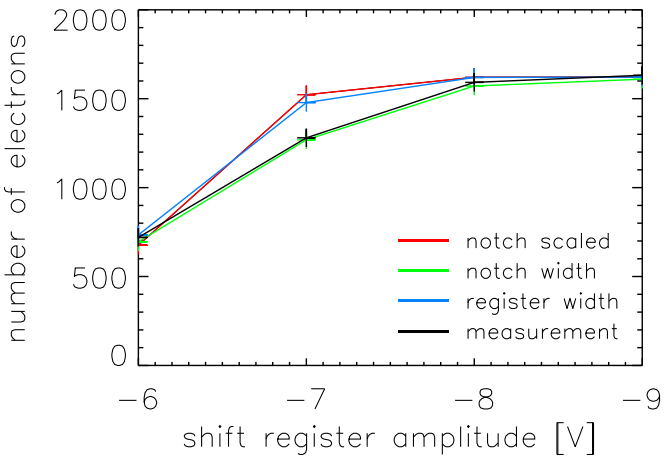

Figure 6.29: Number of transferred electrons vs. shift register amplitude voltage. The number of electrons transferred from pixel C to B is plotted in red for a channel notch doping concentration of 54% of the default value. The green line shows the situation if the channel notch width is reduced by 2.4 µm and matches the measurement data (black curve) already shown in Fig. 6.27. The blue line illustrates the simulation result with a shift register width reduced by 1.83 µm.

A second example illustrating this kind of study is given in Fig. 6.30. The figure shows measurement data of a different pixel, together with simulations as above. As

the number of transferred electrons at -6 V of this second pixel is close to the one of the first example, the same simulations can be used for the comparison (deviation of the amount of transferred electrons between measurement and simulation at -6 V is again less than 10%). This time the measurement data (black curve) is described best by the reduced shift register width (blue curve). Hence, the most likely fault causing this badly transferring pixel is that the shift register width of the p^+ implantation is reduced by about 1.83 µm (although the effect of a scaled doping of the channel notch would be very similar and would also be compatible with the measured data).

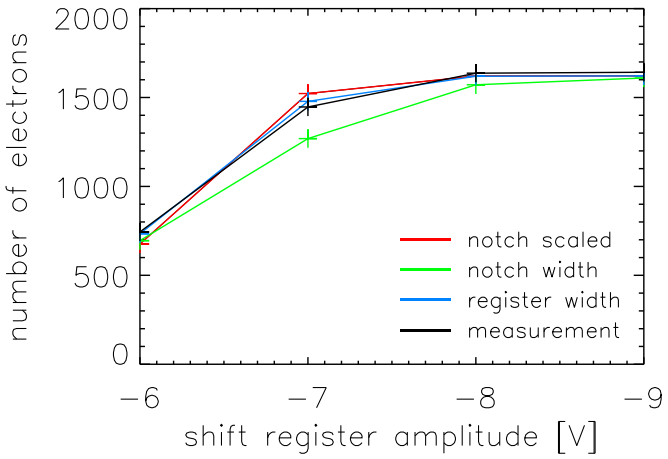

Figure 6.30: This plot shows a second example of a non-transferring pixel measured with different shift register amplitude voltages. Again the number of electrons transferred from pixel C to B is plotted vs. the shift register amplitude voltage. The red curve depicts the simulations result for a channel notch doping concentration of 54% of the default value. The green line shows the situation if the channel notch width is reduced by 2.4 µm. The blue line illustrates the simulation result with a shift register width reduced by 1.83 µm. This case matches the measurement data (black curve) best.

6.4.2 Dead Pixels

This section finally focuses in particular on dead pixels, i.e. non-transferring pixels with no charge transfer at all (see example in Fig. 6.2). During a measurement all electrons generated in the channel behind such a pixel must either be accumulated at the potential barrier where the transfer is halted or leave the pixel in some way. As described above, the latter case could be realised by a reduced shift register width, where the charge flows to the electron layer accumulated underneath the MOS gate. This could hence be one possible cause for a dead pixel. Nevertheless, the question

remains whether also the other kinds of defects (which would lead to an accumulation of large amounts of charge) could lead to dead pixels.

To clarify this aspect, the behaviour of the defects with a large number of electrons was simulated. The number of electrons generated in pixel C was increased by a factor of ten to about 16000. To start with, for both defects of the channel notch, an example parameter was chosen with no transfer but close to the range of bad charge transfer. After one transfer the following could be observed:

- **doping concentration of the n^+ implantation of the channel notch scaled by a factor of 0.4:**
  About 54% of the charge is transferred to pixel B leaving the rest behind.
- **width of the n^+ implantation of the channel notch reduced by 3.5 µm:**
  The fraction of charge transferred to pixel B is 64% whereas the rest is left behind in pixel C.

This result indicates that both cases would not lead to dead pixels since, as soon as enough charge has been accumulated, part of this charge is still transferred.

However, one could expect that this behaviour is changed if the defect parameter is deep in the non-transferring regime (instead of close to the bad-transferring case as above). This case was thus simulated as well. The parameters for the simulations and the obtained results are as follows:

- **doping concentration of the channel notch scaled by a factor of 0.1:**
  About 6% of the charge is shifted to pixel B.
- **width of the channel notch reduced by 5.5 µm:**
  Still 40% of the electrons are transferred to the next pixel.

To conclude one can say that of all studied cases the only one explaining dead pixels (i.e. where no charge - not even thermally generated electrons - reaches the anode) is a reduced shift register width. In the other cases, even strong defects still allow some charge to reach the anode when, after a while, enough charge has accumulated.

7 Summary and Conclusion

eROSITA will be the prime instrument on board the Russian-German satellite mission SRG, scheduled to be launched in 2014. The main aim of eROSITA is to perform an all-sky-survey in the X-ray energy range. For X-ray detection, PNCCDs are used, mainly because of their radiation hardness and their high quantum efficiency in the required energy range. However, since the final space qualified integration of a CCD chip on the detector module is time and cost consuming, it is desirable to investigate the performance of each individual CCD beforehand and only select the best ones for integration.

This need sets the frame for the current work. One of its aims was to characterise the eROSITA PNCCDs as conprehensively as possible on chip level in order to select the best ones for the satellite instrument. Therefor the CCDs were measured with a special measurement setup - the Cold Chuck Probe Station (CCPS). With this setup the CCDs could be operated solely through needle contact and all under the same measurement conditions. All eROSITA CCDs without a short circuit were measured at the CCPS. The results allow for a selection of the seven best ones for the satellite instrument, based on some of the main relevant performance parameters like energy resolution and pixel defects.

Measuring a total of 63 produced CCDs, a mean energy resolution of 160 eV with a spread from 135 eV to 195 eV was found. About one third of the measured PNCCDs could be classified as good or very good, based on reasonable criteria defined in this work (in this case they have an energy resolution of 160 eV or better and no or only a few defect pixels).

Apart from the global CCD parameters such as the energy resolution, also pixel defects could be identified. Generally, these pixel defects can be divided into two categories: the charge generating ones and the non-transferring ones. The second focus of this work was to get a better understanding of the underlying mechanisms for both kinds of defects through additional measurements and simulations.

On the one hand, the amount of charge generated by a defect as a function of the temperature was investigated. The result was compared to both, the expected behaviour according to the Shockley-Read-Hall Model and a simple exponential dependence. It

was found that the simple exponential fit agrees better with the measurement data, indicating that the considered defects are not formed by a single trap but a conglomeration of traps.

Secondly, the influence of the back contact voltage on the charge generating defects was studied. If such defects are close to the surface the amount of generated charge increases with the back contact voltage becoming more negative. This is evident as the electric field increases and thus the time during which the electrons and holes are still close enough to recombine decreases. In contrast, electron-hole pairs generated by bulk defects are separated always immediately due to the higher electric field.

Furthermore, for the non-transferring pixels several possible origins were studied by means of potential simulations. To this end, the simulated implantations building the potential structure of the pixel, i.e. the shift registers and the channel notch, were modified. The simulations were done with the software TeSCA and the following results were achieved:

- A modification in the channel notch implantation, either a lower doping concentration or a reduced width, can lead to a bad transfer or totally prevent the transfer. The charge is trapped in the pixel before by a barrier in the potential structure. In such a case, an increase of the shift register amplitude voltage could improve the charge transfer. Thus a badly or non-transferring pixel can possibly be changed to a transferring one.

- Changing the doping concentration by a scale factor in the range from 0.01 to 10 did not influence the charge transfer much or not at all. Only a very weak doping of 1% of the normal doping concentration led to a considerable effect with about 28% of the charge cloud being left behind.

- Instead, a reduction of the shift register width has a major effect on the charge transfer. It changes the potential such that the MOS gate is not shielded as good as before. Thus the charge is either trapped in a local potential minimum or flows to the electron layer underneath the more positive MOS gate if the potential barrier to the MOS gate is too low. In some cases of a reduced shift register width, the charge transfer can be improved by a more negative amplitude voltage.

The influence of the shift register amplitude voltage is slightly different for the investigated causes of non-transferring pixels. Thus it can be possible to determine the cause of a non-transferring pixel by studying the number of transferred electrons as a function of the shift register amplitude voltage.

Finally, possible defects leading to dead pixels were simulated. If the charge transfer is hampered by a fault of the channel notch (either a lower doping concentration or a reduced width), it was shown that part of the charge is still shifted to the next pixel when enough electrons have accumulated. In contrast, if the width of the shift register is reduced and part of the charge flows to the electron layer underneath the MOS gate, no charge is transferred to subsequent pixels. This is hence the only studied defect which can lead to truly dead pixels.

To conclude, this work reached two main aims. On the one hand, the performance of the eROSITA PNCCDs was succesfully determined and the best ones can now be selected for the satellite instrument. On the other hand, a deeper understanding of defect mechanisms in these devices could be obtained which can serve as a guidance for further improvements of the device quality.

Appendix A

Abbreviations

CAMEX	CMOS Analog Multiplexer
CCD	charge coupled device
CCPS	Cold Chuck Probe Station
CTE	charge transfer efficiency
CTI	charge transfer inefficiency
EPIC	European Photon Imaging Camera
eROSITA	extended Roentgen Survey with an Imaging Telescope Array
FF mode	full frame mode
FS area	frame store area
FS mode	frame store mode
IM area	image area
MPE	Max-Plack-Institute for Extraterrestrial Physics
MPI-HLL	Semiconductor Laboratory of the Max-Plack-Institute
OOT event	out of time event
PCB	printed circuit board
PNCCD	charge coupled device with pn structures
SRG	Spectrum-Roentgen-Gamma

TeSCA Two-Dimensional Semi-Conductor Analysis Package

XMM-Newton X-ray Multi-Mirror Mission - Newton

Appendix B

Voltages for PNCCD Operation

This appendix gives a short overview over all voltages needed for the operation of a PNCCD. Then the values used for these voltages at the CCPS measurements are summarized in Tab. B.1.

All contacts except for one are on the front side. Only one voltage is supplied on the back side - the back contact voltage (RK). It is one of the voltages needed to fully deplete the detector. On the front side there are six contacts to supply the pulses for the shift registers which are needed for the charge transfer and also for the depletion of the detector. The six shift register pulses are generated out of four voltages, two for each part of the CCD (IM and FS area): the offset and the amplitude of the shift registers. The shift register offset is the more positive potential. Below the shift register with the offset voltage the electrons are stored. The more negative potential separating the rows is the sum of offset and amplitude voltage.

Between the shift registers are the isolating MOS gates which also prevent electrons generated by surface defects from drifting into the potential minima of the pixels. All MOS gates except one have a common contact, the MOS contact. Only the one closest to the anode is contacted separately and called AMOS.

The active detector volume underneath the shift registers is separated from the border area by a guard ring - the outer guard ring OGR. Both parts of the bulk are contacted separately and named inner (IS) and outer substrate (OS), respectively. The IS contact is the bulk contact of the active detector volume underneath the pixel structure, while the OS contacts the bulk outside of the outer guard ring. Next to the outer guard ring there is another guard ring which separates the anode from the bulk. Its contact is called guard ring anode (GRA).

Finally, there are three contacts to supply the needed voltages for the on-chip electronics (see 2.2). These are the voltages for gate (RGAT) and drain (RSTA) of the Reset-FET and the drain voltage for the First-FET (FFDR) (see Fig. 2.9).

name	abbreviation	voltage [V]
back contact	RK	-200
offset of shift register in image area	PHI 123 Off	-21
amplitude of shift register in image area	PHI 123 Amp	-6
offset of shift register in frame store area	PHI 456 Off	-19
amplitude of shift register in frame store area	PHI 456 Amp	-6
outer guard ring	OGR	-22
guard ring anode	GRA	-22/-23
reset gate	RGAT	0/-3
reset anode	RSTA	0
inner substrate	IS	0
outer substrate	OS	0
MOS gate	MOS	0
MOS gate next to the anode	AMOS	0
First-FET drain	FFDR	4

Table B.1: Default voltages for the PNCCD operation at the CCPS. The second values of GRA and RGAT are used for the second charge of eROSITA PNCCDs.

List of Figures

List of Tables

Bibliography

[1] R. Giacconi *et al.*, "Evidence for X-rays from Sources Outside the Solar System", *Physical Review Letters* **9** no. 11, (1962) 439–443.

[2] W. Forman *et al.*, "The fourth Uhuru catalog of X-ray sources", *The Astrophysical Journal Supplement Series* **38** no. 4, (1978) 357–412.

[3] W. Voges *et al.*, "ROSAT All-Sky Survey Faint Source Catalogue", *International Astronomical Union Circular* **7432** (2000) 3.

[4] P. Charles and F. Seward, *Exploring the X-ray Universe*. Cambridge University Press, Cambridge, 1995.

[5] M. Santos-Lleo *et al.*, "The first decade of science with Chandra and XMM-Newton", *Nature* **462** no. 7276, (2009) 997–1004.

[6] F. Jansen *et al.*, "XMM-Newton observatory. I. The spacecraft and operations", *Astronomy and Astrophysics* **365** (2001) L1–L6.

[7] E. Pfeffermann *et al.*, "The focal plane instrumentation of the ROSAT telescope", *Proceedings of SPIE* **733** (1987) 519.

[8] L. Strüder *et al.*, "pnCCDs on XMM-Newton - 42 months in orbit", *Nuclear Instruments and Methods in Physics Research A* **512** (2003) 386–400.

[9] P. Predehl *et al.*, "eROSITA", *Proceedings of SPIE* **8145** (2011) 81450D.

[10] A. Zak, "The architecture of Spektr-RG orbital observatory as of 2010." http://www.russianspaceweb.com/spektr_rg.html, 2010. Online; accessed 25-Oct-2011.

[11] P. Predehl *et al.*, "eROSITA on SRG", *AIP Conference Proceedings* **1248** (2010) 543–548.

[12] A. G. Riess *et al.*, "Observational Evidence from Supernovae for an Accelerating Universe and a Cosmological Constant", *The Astronomical Journal* **116** no. 3, (1998) 1009.

[13] S. Perlmutter *et al.*, "Measurements of Ω and Λ from 42 High-Redshift Supernovae", *The Astrophysical Journal* **517** (1999) 565.

[14] J. Frieman, M. Turner, and D. Huterer, "Dark Energy and the Accelerating Universe", *Annual Review of Astronomy and Astrophysics* **46** (2008) 385–432.

[15] C. L. Sarazin, "X-ray emission from clusters of galaxies", *Reviews of Modern Physics* **58** (1986) 1–115.

[16] M. Mühlegger, *Simulated Observations of Galaxy Clusters for Current and Future X-ray Surveys*. PhD thesis, Technische Universität München, 2010.

[17] N. Cappelluti *et al.*, "eROSITA on SRG. A X-ray all-sky survey mission", *Memorie della Societa Astronomica Italiana Supplementi* **17** (2011) 159.

[18] A. Vikhlinin *et al.*, "Cosmological studies with a large-area X-ray telescope", *The Astronomy and Astrophysics Decadal Survey* **2010** (2009) 304.

[19] D. Eisenstein *et al.*, "Detection of the Baryon Acoustic Peak in the Large-Scale Correlation Function of SDSS Luminous Red Galaxies", *The Astrophysical Journal* **633** (2005) 560.

[20] M. White, "Baryon oscillations", *Astroparticle Physics* **24** no. 4, (2005) 334–344.

[21] P. Predehl *et al.*, "eROSITA", *Proceedings of SPIE* **6266** no. 1, (2006) 62660P.

[22] P. Predehl *et al.*, "eROSITA on SRG", *Proceedings of SPIE* **7732** no. 1, (2010) 77320U.

[23] R. Genzel *et al.*, *MPE Report 297*. Max-Planck-Institut für extraterrestrische Physik, Garching, 2010.

[24] P. Friedrich *et al.*, "Design and development of the eROSITA X-ray mirrors", *Proceedings of SPIE* **7011** no. 1, (2008) 70112T.

[25] N. Meidinger *et al.*, "Fast large-area spectroscopic and imaging CCD detectors for X-ray astronomy with eROSITA and for exploration of the nanocosmos", *Proceedings of SPIE* **6686** no. 1, (2007) 66860H.

[26] N. Meidinger *et al.*, "eROSITA camera design and first performance measurements with CCDs", *Proceedings of SPIE* **7011** no. 1, (2008) 70110J.

[27] M. Fürmetz *et al.*, "Operation of the X-ray telescope eROSITA", *Proceedings of SPIE* **7732** no. 1, (2010) 77323K.

[28] M. Pavlinsky *et al.*, "Spectrum-Roentgen-Gamma astrophysical mission", *Proceedings of SPIE* **7011** no. 1, (2008) 70110H.

[29] W. Boyle and G. Smith, "Charge Couple Semiconductor Devices", *Bell System Technical Journal* (1970) .

[30] L. Strüder *et al.*, "The MPI/AIT X-ray imager (MAXI) - High speed pn CCDs for X-ray detection", *Nuclear Instruments and Methods in Physics Research Section A* **288** no. 1, (1990) 227–235.

[31] L. Strüder *et al.*, "The European Photon Imaging Camera on XMM-Newton: The pn-CCD camera", *Astronomy and Astrophysics* **365** no. 1, (2001) L18–L26.

[32] E. Gatti and P. Rehak, "Semiconductor drift chamber - An application of a novel charge transport scheme", *Nuclear Instruments and Methods in Physics Research* **225** no. 3, (1984) 608–614.

[33] S. M. Sze and K. K. Ng, *Physics of Semiconductor Devices*. Wiley-Interscience, Hoboken, NJ, 3. ed., 2007.

[34] J. R. Janesick, *Scientific Charge-Coupled Devices*. SPIE Press, Bellingham, WA, 2001.

[35] G. Lutz, *Semiconductor Radiation Detectors*. Springer Verlag, Berlin, 2001.

[36] N. Kimmel, *Analysis of the charge collection process in solid state X-ray detectors*. PhD thesis, Universität Siegen, 2008.

[37] M. Popp, *Untersuchung und analytische Modellierung der Systemantwort von pn-CCD Detektoren*. PhD thesis, Ludwig-Maximilians-Universität München, 2000.

[38] N. Meidinger *et al.*, "CCD detectors for spectroscopy and imaging of X-rays with the eROSITA space telescope", *Proceedings of SPIE* **7435** no. 1, (2009) 743502.

[39] S. Ebermayer *et al.*, "Quantum efficiency measurements of eROSITA pnCCDs", *Proceedings of SPIE* **7742** no. 1, (2010) 77420U.

[40] N. Meidinger *et al.*, "Development of the focal plane PNCCD camera system for the X-ray space telescope eROSITA", *Nuclear Instruments and Methods in Physics Research Section A* **624** no. 2, (2010) 321 – 329.

[41] E. Pinotti *et al.*, "The pn-CCD on-chip electronics", *Nuclear Instruments and Methods in Physics Research A* **326** (1993) 85–91.

[42] C. Fiorini and P. Lechner, "Continuous charge restoration in semiconductor detectors by means of the gate-to-drain current of the integrated front-end JFET", *IEEE Transactions on Nuclear Science* **46** no. 3, (1999) 761–764.

[43] S. Herrmann *et al.*, "CAMEX readout ASICs for pnCCDs", *IEEE Nuclear Science Symposium Conference Record* (2008) 2952 –2957.

[44] M. Porro, S. Herrmann, and N. Hornel, "Multi correlated double sampling with exponential reset", *IEEE Nuclear Science Symposium Conference Record* **1** (2007) 291–298.

[45] S. Herrmann *et al.*, "Mixed signal pnCCD readout ASIC for the future X-Ray astronomy mission eROSITA", *IEEE Nuclear Science Symposium Conference Record* **3** (2007) 2398 –2403.

[46] J. Elbs *et al.*, "Electronic test system for the eROSITA X-ray PNCCDs", *Proceedings of SPIE* **7742** no. 1, (2010) 774211.

[47] H. Gorke *et al.*, "A compact setup of fast pnCCDs for exotic atom measurements", *AIP Conference Proceedings* **793** no. 1, (2005) 341–346.

[48] R. Hall, "Electron-hole recombination in germanium", *Physical Review* **87** no. 2, (1952) 387.

[49] W. Shockley and W. T. Read, "Statistics of the Recombinations of Holes and Electrons", *Physical Review* **87** no. 5, (1952) 835.

[50] H. Gajewski *et al.*, *WIAS-TeSCA Handbuch*. Weierstrass-Institut für Angewandte Analysis und Stochastik, Berlin, 1996.

[51] W. Van Roosbroeck, "Theory of the Flow of Electrons and Holes in Germanium and Other Semiconductors", *Bell System Technical Journal* **29** no. 4, (1950) 560–607.

Acknowledgments

Everybody writing a PhD thesis knows that this is impossible without the help of many people. So I want to use this opportunity to say thanks.

First of all I want to thank my PhD supervisor Prof. Günther Hasinger for giving me the opportunity to start this PhD in the first place and allowing me to finish the thesis despite him leaving the MPE.

I want to say thank you to Dr. Norbert Meidinger for supervising me during the last years, for his introduction to the world of PNCCDs, the support in the lab and the answers to many questions. Thanks also to Prof. Lothar Strüder for his efforts to make this work possible and the helpful discussions.

Furthermore I want to thank Dr. Robert Andritschke for his great help with the data analysis software and other computer problems and also the proofreading. Many thanks to Dr. Nils Kimmel for introducing me to TeSCA simulations. To Olaf Hälker and Sven Herrmann for supporting me with the electronic setup. I also want to say thank you to Dr. Johannes Elbs for his helping hand in the lab and the many helpful discussions. To Alois Bechteler for always measuring the CCDs as soon as possible. To Dr. Tanja Eraerds for proofreading my thesis.

Special thanks to all my office mates and fellow grad students during the years at the HLL for the nice atmosphere, the countless discussions about physics and other stuff and for the cheerful evenings playing Schafkopf. Finally, I want to thank all of the HLL staff not mentioned earlier for the pleasant working atmosphere.

Last but not least I want to say thank you to all my friends, my family and especially my husband for your patience and love. Without your moral support this thesis would never have been finished.